GEOLOGICA ULTRAIECTINA

Mededelingen van de
Faculteit Aardwetenschappen
Universiteit Utrecht

No. 157

Monte Carlo Waveform Inversion and Deep Continental Structure

Everhard J. Muijzert

GEOLOGICA ULTRAIECTINA

Mededelingen van de
Faculteit Aardwetenschappen
Universiteit Utrecht

No. 157

Monte Carlo Waveform Inversion and Deep Continental Structure

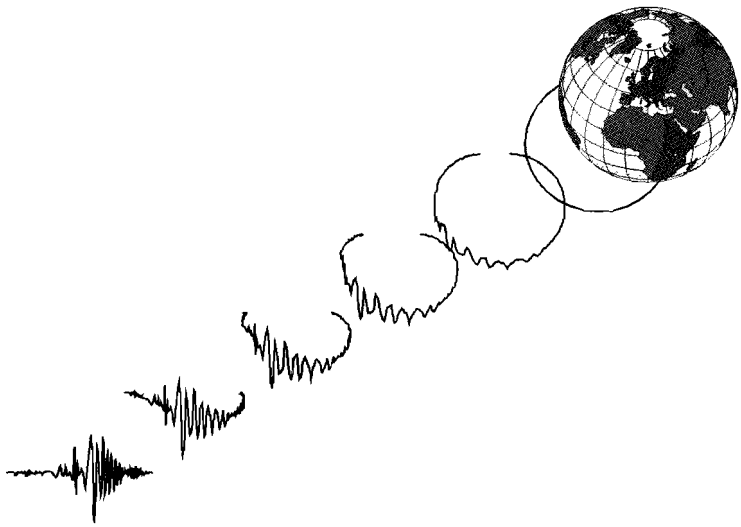

Everhard J. Muijzert

Promotor : Prof. Dr R.K. Snieder

Members of the dissertation committee :

Dr A.J.W. Duijndam	Faculty of Mining and Petroleum Engineering Delft University of Technology
Prof. Dr J.C. Mondt	Institute of Earth Sciences Utrecht University
Dr G. Roult	Institute the Physique du Globe Universite de Paris VII
Prof. Dr N.J. Vlaar	Institute of Earth Sciences Utrecht University
Prof. Dr T.B. Yanovskaya	Institute of Physics University of St. Petersburg

Monte Carlo Waveform Inversion and Deep Continental Structure

Monte Carlo golfvorm inversie en de diepe structuur van continenten

(met samenvatting in het Nederlands)

PROEFSCHRIFT

TER VERKRIJGING VAN DE GRAAD VAN DOCTOR AAN DE
UNIVERSITEIT UTRECHT, OP GEZAG VAN DE
RECTOR MAGNIFICUS, PROF. DR H.O. VOORMA,
INGEVOLGE HET BESLUIT VAN HET COLLEGE VAN DECANEN IN HET
OPENBAAR TE VERDEDIGEN OP
WOENSDAG 14 JANUARI 1998 DES NAMIDDAGS TE 2.30 UUR

DOOR

Everhard Johan Muijzert

Geboren op 20 augustus 1967, te Leiden

Promotor: Prof. Dr R.K. Snieder

The research described in this thesis was carried out at :

Department of Geophysics
Utrecht University
Budapestlaan 4
PO Box 80.021
3508 TA Utrecht
The Netherlands

The investigations were supported by the Netherlands Geosciences Foundation (GOA) with financial aid from the Netherlands Organization for Scientific Research (NWO) through project 750.600.01. The NARS-DEEP project has been supported by NWO "Samenwerkingsprogramma met Russische Federatie" project 047-003-035, INTAS project 93-1076 and INCO-Copernicus contract ERBIC15CT960207. This work was conducted under the programme of the Dutch national research school, the Vening Meinesz Research School of Geodynamics.

ISBN 90-5744-015-6

Contents

Chapter 1

Introduction

The study of the three dimensional structure of the earth is limited by the uneven distribution of earthquake sources and seismic stations. The distribution of the earthquakes is fixed as most earthquakes occur along the plate boundaries. The use of artificial sources can improve the distribution of seismic sources but such experiments are not popular as they require sources with the strength of a nuclear explosion in order to probe the mantle. The distribution of seismic stations is mainly concentrated in regions with a significant earthquake risk. In Europe the availability of seismic data has also been restricted by political borders. The politically changes in the 1980's and 1990's in Eastern Europe lead to increased scientific communication which has resulted in the NARS-DEEP (Network of Autonomously Recording Seismographs Deployed on the East European Platform) project. The NARS-DEEP project has been initiated to increase the data coverage in Eastern Europe and to investigate the geodynamic history of the region. Starting in the summer of 1995 eleven modern digital seismic stations have been installed in Russia, Belarus, Ukraine and Finland, see Figure 1.1. Other organizations such as IRIS and GEOFON also installed several seismic stations in the region. In this thesis the velocity structure of Eastern Europe is investigated using these newly available data.

In regions with poor data coverage surface waves are very useful for studying the lithosphere and upper mantle. Using the dispersion characteristics of the surface waves an image of the velocity variations with depth can already be made when few data are available. Lateral variations in the velocity structure can be studied by comparing phase velocity measurements from different source receiver combinations. In this thesis several new techniques have been developed in order to improve the methods for analysis of the surface wave data.

Modern surface wave analysis techniques such as single station dispersion measurements (Trampert and Woodhouse 1995) and waveform inversions (Woodhouse and Dziewonski 1984; Nolet 1990) depend on the accuracy of the source parameters necessary to compute the synthetic seismograms. In chapter 2 the influence

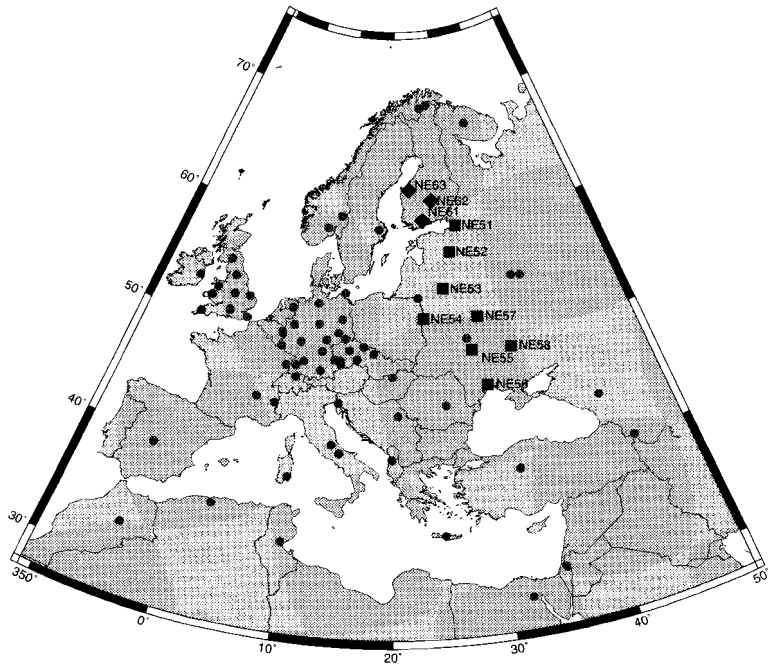

Figure 1.1: Digital broadband seismic stations in Europe. The NARS-DEEP and the NARS-TOR stations are indicated by the squares respectively diamonds.

of uncertainties in the source parameters on the modeling of surface waves is investigated. This study is the result of an analysis of a cluster of events recorded at the station KEV that showed that it was impossible to fit all data simultaneously. This was very clear for two events where one event had a phase delay while the other event had a phase advance. The only likely explanation is that these phase differences are due to errors in the source mechanism. The estimated uncertainties in the published source mechanisms are small. Updating these mechanisms using teleseismic data is only possible when a global coverage of data is available but most of such data has already been used for the construction of these source mechanisms as it is collected by IRIS. We therefore took an other approach. Using the published source mechanisms a method has been developed by which the frequency bands where the signal depends very strongly on the source characteristics can be identified. This method turned out to be very successful as it provides an objective criterium for rejecting frequency components in the data that are likely to be strongly influenced by errors in the source mechanism.

Chapter 3 deals with the influence of anisotropy on the propagation of surface waves. Anisotropy in the earth is already for a long time recognized as being important. The basic equations for the computation of rays and travel-times in a

general anisotropic spherical earth were derived by Vlaar (1968). In 1982 Anderson explained : "*We knew that our isotropic models were not very good but we had no other choice. It is simply that, so far, computers were not large enough to integrate the anisotropy parameter.*" (after A. Nicolas, Babuska and Cara 1991). It is also well known that the computation of the normal modes in the earth for other models than isotropic or transverse isotropic with vertical symmetry axis is not (yet) possible due to severe computational problems. Anisotropy does not only cause computational problems. The dispersion measurements of surface waves are inverted to medium parameters using the partial derivatives. In chapter 3 it is shown that the partial derivatives to the commonly used parameterset for the transverse isotropic medium (e.g. Takeuchi and Saito 1972) has intrinsic trade-offs. Because of these trade-offs it is not possible to resolve all parameters independently from surface wave data. In chapter 3 a new parameter set that does not have these intrinsic trade-offs is proposed and tested.

In chapter 4 a two-dimensional cross-section of the upper mantle from Egypt to Spitsbergen is presented. This study is obtained by the inversion of seismic waveforms using an approach similar to the method of partitioned waveform inversion as developed by Nolet (1990). For the first time this method has been applied to Love waves. The model shows the East European continent as a high velocity body extending down to 200 km depth. This is in contrast to previous studies such as Lerner-Lam and Jordan (1987) who proposed 400 km think continental roots. In the East European continent seismic velocities and thickness of the high velocity layer increase with tectonic age. In the Eastern Mediterranean 7% higher horizontally polarized shear velocity, β_H, than vertically polarized shear velocity, β_V, is observed which we interprete as anisotropy, This anisotropy can be explained by the presence oceanic lithosphere that is consistent with plate tectonic reconstructions of the region.

In chapters 5 and 6 a new higher mode waveform inversion technique with improved depth resolution is used. This method is a combination of two existing methods. The first method is the partitioned waveform inversion as developed by Nolet (1990). In this method waveforms from the fundamental mode up to the direct S-wave are inverted directly for path averaged velocity functions. The path averaged velocity functions are combined in a second inversion in order to obtain a tomographic image (see chapter 4). Each single seismogram is thus directly inverted for the depth structure without measuring the dispersion curves. As a single event does contain all the dispersion characteristics e.g. the seismogram of a shallow event contains only poorly excited higher modes, it is likely that some higher modes are not well constrained . The second method is the higher mode dispersion measurement technique of Stuzmann and Montagner (1993). They inverted waveforms of a cluster of events for the higher mode dispersion curves. As the selected events had different source depths the higher mode information is better retrieved. A disadvantage of the second method is that it is difficult to measure the individual dispersion curves at high frequencies as they tend to interfere with each other. Our methods combines the advantages of both methods

by a simultaneous inversion of waveforms from a cluster of events for the path averaged velocity structure.

Initially we inverted the data using an iterative gradient method. This was not a successful approach as the inversion got often stuck in local minima and the best fitting model turned out to be dependent on the starting model. The iterative gradient inversion together with necessary tests with different starting models and resolutions tests required a surprising large number of forward model evaluations, often more than 1000. This number is significantly more than for the inversion of a single seismogram. The problems with the gradient method can be avoided with global inversion methods. The drawback of a global method is of course an increased computational time but with the increasing computational speed and compilers that allow parallelisation these global methods have become feasible. The time the computer spent on these Monte Carlo runs was often less than the time I spent on the interpretation of results and also less than needed for gradient methods when all kinds of resolution tests and evaluation of secondary minima had to be performed. In this thesis two different global methods are applied to the waveform inversion problem.

In chapter 5 an extensive Monte Carlo search is carried out on waveform data sampling central Eurasia. The resolution of this Monte Carlo inversion is determined using the resolution analysis of Kennett and Nolet (1978). The Monte Carlo waveform inversion is applied on the cluster of events in the Hindu Kush region recorded in KEV (Finland) and the path averaged velocity structure is determined. The resolution analysis shows that the joint inversion of waveforms indeed improves the depth resolution of the waveform inversion. Both an isotropic and an anisotropic inversion is carried out where the parameterization for transverse isotropy derived in chapter 3 is used. The model shows that the Central Eurasian lithosphere has a S-velocity of 4.6 km/s and has 2% anisotropy. Below 200 km depth the velocities are very similar to the average earth model PREM. The anisotropy is smaller than found by other studies possibly due to better modelling of the crust.

In chapter 6 an adaptive Monte Carlo method is applied to the waveform inversion problem. Using this method we determine the marginal probability density functions which are in the Bayesian theory the solution of the inverse problem. Using this method we investigate another region, the East-Pacific Rise. Data is used from a cluster of Central American events recorded at Eastern Island. Unfortunately the data of the horizontal components was of poor quality due to a high noise level on this island site and could not be used. Only the Rayleigh waves recorded on the vertical component have been used. The velocity model shows that the waveforms can be explained by a significant low velocity zone down to approximately 180 km depth. Below this depth the velocity structure of this fast spreading Mid Ocean Ridge is well described by the average earth model PREM.

Chapter 2

The influence of errors in source parameters on phase velocity measurements of surface waves

2.1 Abstract

The phase of both Love and Rayleigh waves can be very sensitive to errors in the source parameters. This unstable behaviour of the phase depends on the source parameters and is frequency dependent. Fractional errors larger than 10° in the phase measurements can arise when realistic errors in the source parameters are considered. When these phase measurements are interpreted as phase velocity, uncertainties up to 3% can occur when errors in the source parameters are considered. The frequency bands where the unstable behavior occurs can be found by calculating the partial derivative of the initial phase with respect to the various source parameters. We have tested this method on a Rayleigh wave data set and find a good correlation between outliers in the data set and large partial derivatives of the source parameters.

2.2 Introduction

The phase of the fundamental mode surface wave is assumed to be a robust parameter in the seismogram and is widely used in upper mantle studies in both regional (e.g. Knopoff, 1972; Yanovskaya et al. 1988) and global studies (e.g. Nakanishi and Anderson, 1984; Zhang and Tanimoto, 1993). In such studies the phase shift of the surface wave due to the propagation through the earth has to be separated from the initial phase due to the excitation of the surface wave (i.e. the earthquake). Several methods have been developed to do this.

This chapter has been published as : Muyzert, E.J. and R.K. Snieder, 1996. The influence of errors in the source parameters on phase velocity measurements of surface waves, *Bull. Seis. Soc. Am.*, 86, 1863-1872.

Traditionally the propagation of the phase through the earth is measured with the two-station method. In this method one uses two stations on the same great circle as the event. The phase difference between the stations is due only to propagation because the stations are at the same azimuth of the source. In principle, the two-station method is very powerful but its limitation is that both the event and the stations have to lie on the same great circle which is seldom the case.

With the routine publication of accurate seismic moment tensors by research groups at both Harvard University (Dziewonski and Woodhouse, 1983) and the NEIC (Sipkin, 1986) another method for measuring phase velocities became popular which does not have the great circle limitation: the single station method. In the single station method the moment tensor solution is used for the calculation of a synthetic seismogram in a reference earth. The phase difference between the synthetic seismogram and the data is assumed to be only due to differences in propagation from the reference earth. A limitation of the single method is that it requires an accurate source model.

A waveform inversion uses both the amplitude difference and the phase difference between observed and synthetic seismograms. In most cases, however, the waveform inversion uses mainly the phase information so it becomes effectively equivalent to the phase-velocity measurement obtained by the single station method (e.g. Woodhouse and Dziewonski, 1984; Zielhuis and Nolet, 1994b).

As with all physical parameters, the source parameters of an earthquake have uncertainties. It is clear that using the single station method an error in one of the source parameters will lead to an error in the measured phase. For surface wave studies the relevant source parameters are: origin time, epicenter, rise time or half duration time, depth, fault-plane or moment tensor solution, seismic moment and structure near the source. Uncertainties in any of these parameters attribute to uncertainties in the phase measurement. The question is how large will the error in the phase measurement be due to a realistic error in our source model? Estimates on the uncertainty of the origin time, rise time and epicenter are given by Nakanishi and Anderson (1984). Uncertainties in the seismic moment are probably large but for phase-velocity measurement mostly the amplitude of the waveform is normalized and only the phase of the waveform is determined. In this study we look at the uncertainties in the phase velocity due to errors in the fault-plane parameters, depth and earth model near the source.

Our motivation for this study comes from a data set that gives inconsistent phase measurements for events on a single source-receiver path. This data set is presented in section 2.3. At periods $T \geq 100$ s phase differences larger as 10° are observed. An important conclusion is that the phase inconsistency is frequency dependent and that it must be due to errors in the source parameters. Phase errors of this size may give errors in phase velocity measurements up to 3%, depending on frequency and epicentral distance. In the rest of this paper we show that frequency dependent errors of this size in phase velocity measurements can be caused by errors in the following source parameters: depth, dip, rake and strike and earth model near the source. In section 2.4 we summarize the theory of the excitation of

surface waves due to a pure double couple source. In section 2.5 experiments with errors in the fault-plane parameters and depth of the source for Rayleigh waves are shown. In section 2.6 and 2.7 similar experiments with Love waves and higher mode data are shown. Finally in section 2.8 we show that the partial derivatives of the initial phase of the surface wave can be used as a diagnostic for determining parts of the frequency spectrum where small uncertainties in the source parameters lead to excessive phase changes of the surface wave.

2.3 Data with errors in the source parameters?

In figure 2.1 we show an example of Rayleigh wave data that give conflicting phase measurements when the single station method is used. The data consist of Rayleigh waves from earthquakes in the Hindu-Kush region with a magnitude $M_w \geq 5.5$ for the years $1990-1993$ recorded at station KEV in Finland ($27.0066°E, 69.7553°N$). In the Hindu-Kush region ($36° \pm 3°E, 72° \pm 3°N$) localized seismicity occurs down to a depth of about 250 km due to the collision between the Indian and Eurasian plate. The data has been checked for clipping of the instrument and signal-to-noise ratio within the relevant frequency band. The selected events are listed in Table 2.1. Since the epicentral distance is large compared to the distance of epicenters with each other, the waves have travelled effectively along the same path. The seismograms are bandpass filtered between $T = 70-100$ s within the group velocity window $4.3-3$ km/s to isolate the fundamental Rayleigh wave (Fig. 2.1b). We also show the traces bandpass filtered between $T = 150 - 200$ s in the group velocity window $6 - 2.5$ km/s (Fig. 2.1a). At this long period and epicentral distance the higher modes are not separated from the fundamental mode. The higher mode energy arrives before 1000 s (group velocity larger than 4.5 km/s).

year, date	longitude (°E)	latitude (°N)	depth (km)	dip (°)	rake (°)	strike (°)
1993.334	75.53	39.26	18	74	4	219
1993.261	71.59	36.42	113	48	144	233
1993.247	70.81	36.43	195	24	121	240
1993.204	70.42	36.44	272	48	-154	354
1992.141	71.32	33.38	16	5	79	237
1991.195	71.15	36.42	219	42	118	287
1991.031	70.45	35.99	140	17	68	247
1990.194	70.79	36.45	203	17	93	283
1990.135	70.44	36.03	117	36	48	216
1990.107	75.03	39.38	15	68	156	118

Table 2.1: List of events

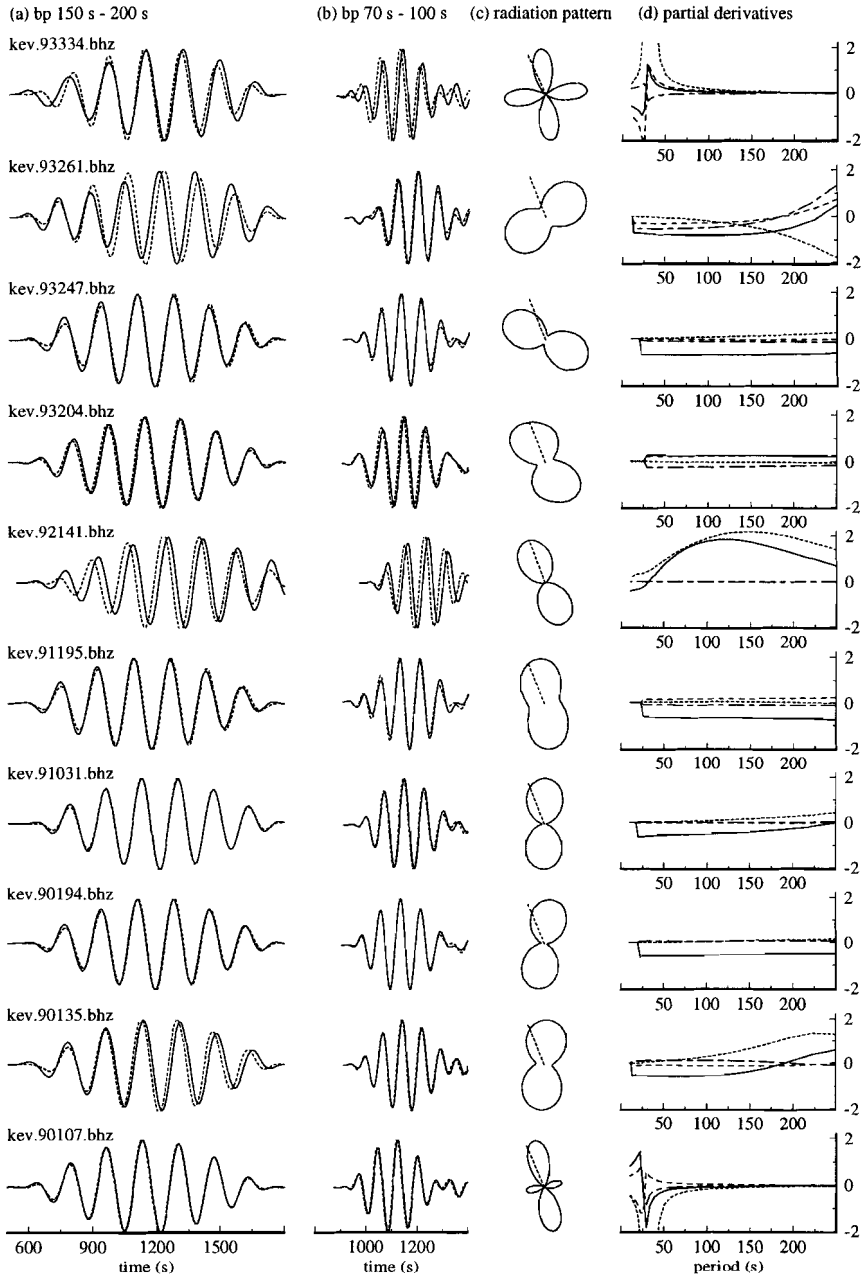
(a) bp 150 s - 200 s
(b) bp 70 s - 100 s
(c) radiation pattern
(d) partial derivatives
kev.93334.bhz
kev.93261.bhz
kev.93247.bhz
kev.93204.bhz
kev.92141.bhz
kev.91195.bhz
kev.91031.bhz
kev.90194.bhz
kev.90135.bhz
kev.90107.bhz
600 900 1200 1500
time (s)
1000 1200
time (s)
2
0
-2
50 100 150 200
period (s)

The events are shown together with synthetic data calculated using published source parameters (ISC epicenter and origin time, and Harvard moment tensor and half duration time). The synthetics are calculated for a continental velocity model with a Moho depth of 40 km. Between 40 km and 220 km depth the S-velocity is 4.7 km/s. Below 220 km the velocity is given by the PREM model (Dziewonski and Anderson ,1981). This velocity model seems to be a good representation of the average earth structure along the path from the Hindu-Kush towards KEVO since for most events the waveform fit is quite good.

For 4 events however, it is not possible to fit the long period data ($T = 150-200$ s) with a single velocity model (see Fig. 2.1a, events 90135, 92141, 93261,93334). Event 93261 shows a phase advance of $+45°$ of the data with the synthetics which indicates that a faster velocity model is required to fit this seismogram. Two other events 92141 and 90135 have a phase delays of $-45°$ and $-10°$ respectively so for these events a slower velocity model is needed to explain the data. Event 93334 also has a poor fit but it does not have a constant phase shift. The early part of this seismogram has a phase advance compared with the synthetics while the late part of the data has a phase delay. At shorter periods ($T = 70 - 100$ s) almost all the events have a very good fit (see Fig. 2.1b). Only events 92141 and 93334 have a phase delay. The observed phase differences for these four events are not due to an error in epicenter or origin time since this would have been reflected in an equal time shift in the two bandpass filtered traces. Such a constant time shift is only observed for event 93204. On the contrary, for events 93261 and 90135 a time shift is only observed for the frequency band $T = 150 - 200$ s. Finally, event 92141 has an unequal shift in the two frequency bands which can not be explained with an timing error. We have checked the arrival time of the direct P-wave for this event and found that it is not significantly delayed.

In figure 2.1c the amplitude radiation patterns of the events are shown. It is well-known that at azimuths near a node in the amplitude radiation pattern, phase uncertainties occur. From the four events that show phase differences, only event 93334 is near a node. Event 93261 is at the azimuth of minimum amplitude but it has still a significant magnitude. Furthermore, the other two events, 92141 and 90135, are not located near such a minimum, in fact the first is at the azimuth of maximum amplitude.

Figure 2.1: Previous page. Data (solid line) and synthetics (dashed line) for 10 earthquakes in Hindu-Kush region, listed in Table 2.1, recorded at station KEV. Column (a) bandpassed seismogram between $T = 150 - 200$ s. Column (b) bandpassed seismogram between $T = 70 - 100$ s. Column (c) Amplitude radiation pattern of fundamental mode Rayleigh wave at period $T = 100$ s. The dashed line indicates the azimuth of the station. Column (d) Partial derivatives of the initial phase of fundamental mode Rayleigh wave as function of period. Solid line represents the partial derivative to dip, the long dashed line to rake, the dash-dotted line to azimuth and the short dashed line to depth.

The observed phase differences have a large influence on phase velocity estimates. For the apparent phase-velocity C_a due to such a phase difference we can write

$$C_a = C_0 \left[1 - \frac{1}{1 + \frac{360r}{C_0 T d\theta}} \right] \tag{2.1}$$

with C_0 the true phase-velocity at period T, r the epicentral distance and $d\theta$ the phasediffence in degrees. As an example we compute the difference in phase-velocity for event 92141 which has a phase shift of $d\theta = 45°$ and a true phase-velocity $C_0 = 4.5$ km/s at a period $T = 175$ s. For an epicentral distance $r = 4000$km we infer a phase velocity of $c = 4.39$ km/s, which gives an error of 2.5% in the measured phase-velocity. From equation (2.1) we see that this kind of errors is particular important for surface wave analysis on a regional scale. On a global scale with distances which are one order of magnitude larger the error in the phase-velocity measurement due to such phaseshifts will be less. When we average phase-velocity measurements, including ones with large phaseshifts, we probably would get a value close to the true value but with a large spreading in the individual measurements. Identifying the events with large phaseshifts can therefore improve the average phase-velocity measurement for source-receiver paths with sparse data and reduces the large spreading the data.

As all the events in figure 2.1 have the same source-receiver path such a large spreading in measured phase cannot be caused by propagation effects. The phase differences are also not caused by errors in origin time and epicenter, or by the fact that we might be close to a node in the radiation pattern. Therefore we have to examine the possibility of uncertainties in the source.

2.4 The excitation of surface waves

Surface waves in a laterally homogeneous medium can be described by the sum of n propagating surface wave modes (Aki and Richards, 1980).

$$u(\mathbf{x}, \omega) = \sum_n A_n \exp\left[ik_n r\right] S_n \tag{2.2}$$

In equation (2.2) A_n describes the modal structure near the station and the geometrical spreading. The exponent describes the phase shift due to the propagation over a distance r. The excitation term S_n describes the initial phase and amplitude of the wave. Omitting the subscript n for clarity, the excitation term S^{Love} for Love waves is given by:

$$\begin{aligned} S^{Love} = ikl_1(h) \left[M_{xx} \sin\phi\cos\phi - M_{yx}\cos^2\phi + M_{xy}\sin^2\phi - M_{yy}\sin\phi\cos\phi \right] \\ - \frac{dl_1}{dz}|_h \left[M_{xz}\sin\phi - M_{yz}\cos\phi \right] \end{aligned} \tag{2.3}$$

For Rayleigh waves it is given by:

$$\begin{aligned} S^{Rayleigh} = & kr_1(h)\left[M_{xx}\cos^2\phi + (M_{xy}+M_{yx})\sin\phi\cos\phi + M_{yy}\sin^2\phi\right] \\ & + \frac{dr_2}{dz}|_h\, M_{zz} + i\frac{dr_1}{dz}|_h\left[M_{xz}\cos\phi + M_{yz}\sin\phi\right] \\ & -ikr_2(h)\left[M_{zx}\cos\phi + M_{zy}\sin\phi\right] \end{aligned} \tag{2.4}$$

with M_{ij} the moment tensor elements, ϕ the azimuth at the source, measured clockwise from North, k, the wavenumber, $l_1(h), r_1(h), r_2(h)$ the eigenfunctions for Love and Rayleigh waves at source depth h, period T and mode n. Note that both $S^{Love}$and $S^{Rayleigh}$are complex and have to be evaluated for each mode separately.

Expressions for the moment tensor due to a double couple source are given by Aki and Richards (1980). These expressions normally contain the strike of the fault ϕ_s, and the azimuth of the receiver at the source ϕ, both measured clockwise from North which are used to describe the relative azimuth $\phi_r = \phi - \phi_s$ between the strike and the azimuth of the receiver at the source. Here we use this relative azimuth $\phi_r = \phi - \phi_s$, which is in fact a rotation of the x-axis towards the strike direction, to obtain a simple expression for the moment tensor elements. In the new coordinate system with x' in the direction of the strike, y' perpendicular to it in the horizontal plane and z' pointing downwards, the moment tensor is given by :

$$\begin{aligned} M_{x'x'} &= 0 \\ M_{x'y'} &= M_{y'x'} = M_0 \sin\delta\cos\lambda \\ M_{x'z'} &= M_{z'x'} = -M_0\cos\delta\cos\lambda \\ M_{y'y'} &= -M_0\sin 2\delta\sin\lambda \\ M_{y'z'} &= M_{z'y'} = M_0\cos 2\delta\sin\lambda \\ M_{z'z'} &= M_0\sin 2\delta\sin\lambda \end{aligned} \tag{2.5}$$

where M_0 is the seismic moment, δ the dip of the fault-plane measured perpendicular to the strike direction and the vertical axis, and λ the rake measured in the fault plane as the angle between the strike and the displacement vector.

Each fault-plane moment tensor can be described as the sum of four moment tensors which are related to the four elementary fault planes: the horizontal fault, the strike-slip fault, the 45° fault and the dip-slip fault (Aki and Richards, 1980). Using this, we can write the excitation term for both Love waves (equation 2.3) and Rayleigh (equation 2.4) as the sum of four elementary excitation terms that give the excitation of the four elementary fault-plane solutions.

$$S = S^{strike-slip} + S^{hor.fault} + S^{45^\circ} + S^{dip-slip} \tag{2.6}$$

For Love waves the elementary excitation terms are given by:

$$S^{strike-slip} = iM_0 k l_1(h)\sin\delta\cos\lambda\left[\sin^2\phi_r - \cos^2\phi_r\right] \tag{2.7}$$

$$S^{hor.fault} = M_0\frac{\partial l_1}{\partial z}|_h\cos\delta\cos\lambda\sin\phi_r \tag{2.8}$$

$$S^{45^\circ} = iM_0 k l_1(h) \sin 2\delta \sin\lambda \sin\phi_r \cos\phi_r \tag{2.9}$$

$$S^{dip-slip} = M_0 \frac{\partial l_1}{\partial z}|_h \cos 2\delta \sin\lambda \cos\phi_r \tag{2.10}$$

For the Rayleigh waves they are give by:

$$S^{strike-slip} = 2M_0 k_n r_1(h) \sin\delta \cos\lambda \cos\phi_r \tag{2.11}$$

$$S^{hor.fault} = -iM_0 \left[\frac{\partial r_1}{\partial z}|_h - k_n r_2(h)\right] \cos\delta \cos\lambda \cos\phi_r \tag{2.12}$$

$$S^{45^\circ} = M_0 \left[\frac{\partial r_2}{\partial z}|_h - k_n r_1(h) \sin^2\phi_r\right] \sin 2\delta \sin\lambda \tag{2.13}$$

$$S^{dip-slip} = iM_0 \left[\frac{\partial r_1}{\partial z}|_h - k_n r_2(h)\right] \cos 2\delta \sin\lambda \sin\phi_r \tag{2.14}$$

The initial phase of a surface wave mode n is defined as:

$$\varphi_n = \arctan\left[\frac{imag(S_n)}{real(S_n)}\right] \tag{2.15}$$

The elementary excitation terms are either purely real or purely imaginary. Thus the corresponding initial phase is $0°, 90°, 180°$ or $270°$. An arbitrary moment tensor source is the sum of elementary fault-plane solutions. Its excitation term has a real and an imaginary and the initial phase can have every value between $0°$ and $360°$.

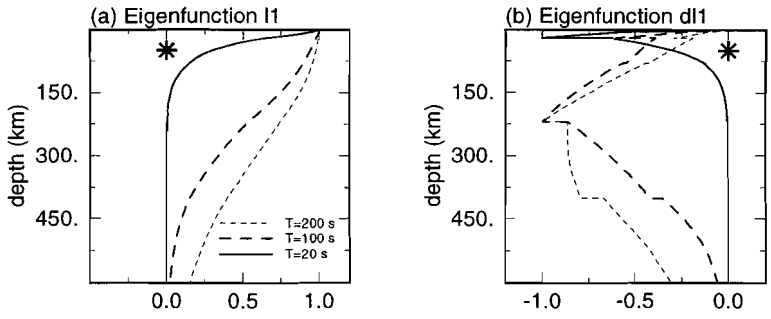

Figure 2.2: (a) Eigenfunctions in the elementary excitation terms $S^{strike-slip}$ and S^{45° for Love waves defined in equation 2.7-2.10 normalized to maximum value. The solid line represents the elementary excitation terms at a period $T = 20$ s, the thick dashed line at $T = 100$ s and the thin dash line at $T = 200$ s. (b) $S^{hor.fault}$ and $S^{dip-slip}$.

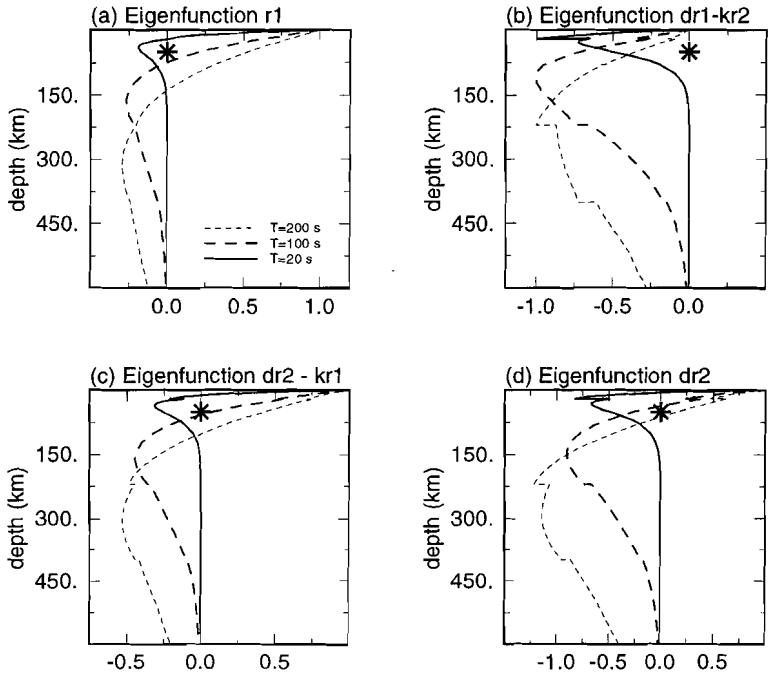

Figure 2.3: (a) Combinations of eigenfunctions in the elementary excitation terms $S^{strike-slip}$ for fundamental Rayleigh waves defined in equation 2.11 normalized to maximum value. Solid line $T = 20$ s. Thick dashed line $T = 100$ s. Thin dash line $T = 200$ s. (b) $S^{hor-fault}$ and $S^{dip-slip}$ at azimuth $\phi_r = 90°$. (c) $S^{45°}$. (d) As (c) but with azimuth $\phi_r = 0°$.

The elementary excitation terms for Love waves dependent on the eigenfunction l_1 or its derivative. For the fundamental Love wave, at the periods used in surface wave studies, l_1 is positive and its depth derivative is negative (Fig. 2.2).

The elementary excitation term of the strike-slip fault for Rayleigh waves depends on the eigenfunction r_1 (see equation 2.11). An important characteristic of r_1 is that it has a zero crossing at shallow depth. Around this zero crossing the eigenfunction obviously changes sign (see Fig. 2.3a). Near the surface r_1 is positive, in the deeper layers it is negative. The depth of the zero crossing increases with period. As a consequence, the excitation term of a strike-slip earthquake, which contains $r_1(h)$ (see equation 2.11), will be zero at this period and the initial phase will change 180°. The elementary excitation term and the initial phase of the strike-slip fault is now frequency dependent. The elementary excitation terms for the horizontal fault and the dip-slip fault of Rayleigh waves both depend on the same combination of eigenfunctions (see equations 2.12 and 2.14). This combination is negative for all frequencies (Fig. 2.3b). The combination of eigenfunctions

for the 45° fault is dependent on azimuth which can be seen from equation (2.13). We show two azimuths ($\phi_r = 0°, \phi_r = 90°$) where maximum and minimum values occur (Fig. 2.3c-d). They both have a zerocrossing which implies that Rayleigh waves excited by this type of fault have also a frequency dependent initial phase.

2.5 Fundamental mode Rayleigh wave

Error estimations of the source parameters are difficult to obtain since there is a trade-off between the source parameters and the three dimensional structure of the earth. The depth uncertainty of the Harvard CMT solution is estimated to be 10 km by Ekstrom (1987). For an error estimation in the source parameters we compared the preferred double-couple solutions by the Harvard group and the NEIC as published in the ISC bulletins. These solutions are obtained using different data and different methods. The differences are in the order of 10° for dip, rake and strike. In the following we therefore use errors of 10° for the fault-plane parameters and 10 km for the depth.

In Figure 2.4 (thick solid line) we show the initial phase and amplitude and a bandpass-filtered fundamental Rayleigh wave from a shallow earthquake ($h = 20$ km) with a fault plane dipping at an angle of 45°, an azimuth $\phi_r = 90°$ and distance $r = 10°$. The seismic wave is excited and propagated through the PREM model. The excitation of this source is describe by the elementary excitation term $S^{45°}$ given by equation (2.13). At period $T = 25$ s the initial phase changes from 180° to 0° and the initial amplitude drops more then 2 order of magnitude (see Figures 2.4a-b). At the source depth ($h = 20$ km) the eigenfunction present in $S^{45°}$ has a zero crossing at a period of 25 s, therefore the initial amplitude will be zero (see Fig. 2.3c, equation 2.13).

Also shown in Figure 2.4 (thick dashed line) is the same event but now with an error of +10 km in the source depth. The amplitude drop and phase reversal occur now at a larger period, $T = 40$ s. Between $T = 25$ s and $T = 40$ s a change in the source depth from 20 km to 30 km gives a difference in the initial phase of 180°. At other periods there is no phase distortion. The seismogram bandpass filtered between 20 s and 100 s is significantly different in both phase and amplitude when the source depth is perturbed (Fig. 2.4c). However, at larger periods only amplitude differences are observed (Fig. 2.4d). The sensitivity of the initial phase, amplitude and waveform to a small perturbation in the source depth is caused by the fact that at larger source depths the zero crossing of the combination of eigenfunctions present in $S^{45°}$ is shifted towards longer periods. Note that in the seismogram for $T \geq 100$ s no phase differences, only amplitude variations appear. If the traces were normalized no difference would be observed. At shorter periods ($T \leq 100$ s) the waveforms differ significantly and phase measurements would be influenced by the error in the source depth.

Another possible source of error is the modal structure near the source. Zielhuis and Nolet (1994) showed that changing the earth model in the excitation

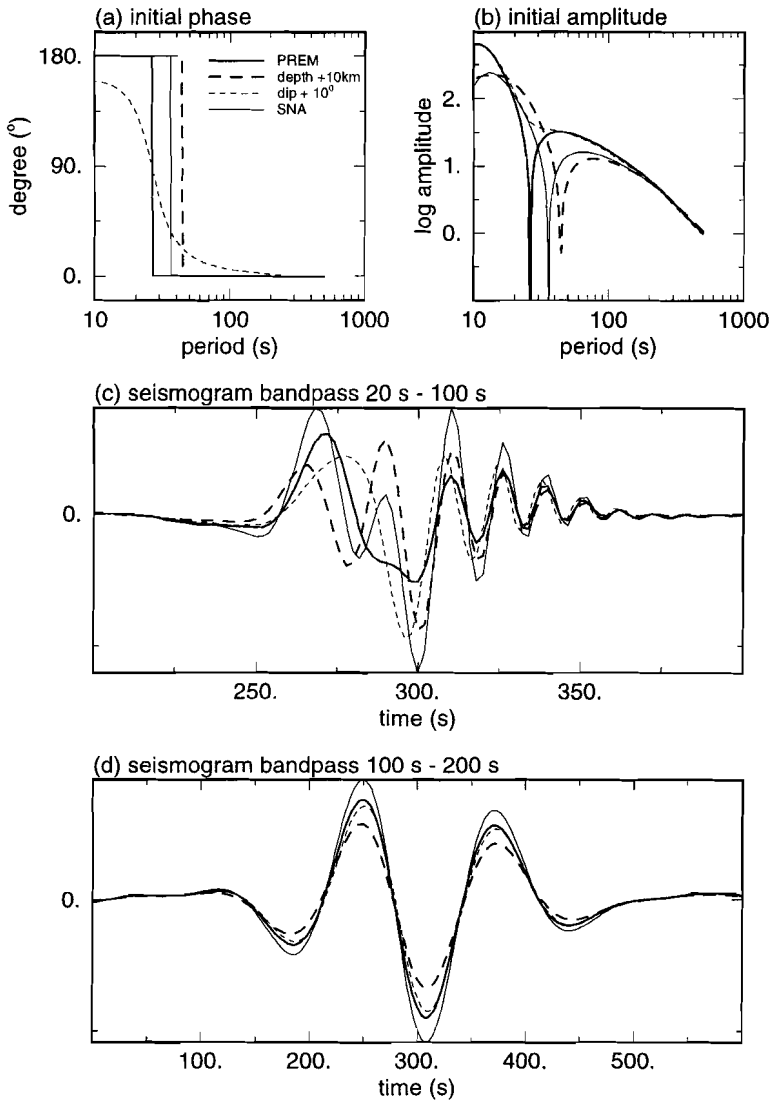

Figure 2.4: (a) The initial phase of a fundamental mode Rayleigh wave for a fault dipping 45° ($h = 20$ km, $\delta = 45°$, $\lambda = 90°$, $\phi_r = 90°$). The thick solid line represents the unperturbed case, the thick dashed line a source at $h = 30$ km, the thin dashed line a dip $\delta = 55°$ and the thin solid line the SNA model at source. (b) The initial amplitude for same sources as in the (a). (c) Seismograms for the source in (a), bandpassed between $T = 20 - 100$ s. (d) As (c) but now bandpassed between $T = 100 - 200$ s.

term (equation 2.3 and 2.4) has a significant influence on the surface waveform. McLaughin et al. (1992) have modeled inhomogeneous structure, a subducting slab, near the source and found that it has a large influence on both the phase and the amplitude of surface waves. These phase and amplitude distortions are frequency dependent since they depend on the characteristic wavelength of the inhomogeneous structure. We do not take this effect into account since this phenomenon can not be modelled with the far field approximation of the wave field give by equation (2.2) but requires the calculation of the full wave field near the source. We investigate the difference between surface waves excited in PREM with surface waves excited in the SNA model of Grand and Helmberger (1984). The SNA model is a model for the S-velocity in the Canadian shield and is characterized by a deeper Moho (38 km for SNA compared to 24.4 km for PREM) and by a higher velocity in the upper 200 km of the earth compared to PREM.

Using the eigenfunction of SNA instead of PREM in the excitation term gives a phase difference of 180° in the initial phase between $T = 25$ s and $T = 35$ s (Fig. 2.4, thin solid line). Like the source depth perturbation at other periods the phase of the wave is not perturbed. The filtered seismogram for $20 < T < 100$ s is significant different from the seismogram calculated using PREM in the excitation term.

The source we use in this example has a excitation term which consists only of an S^{45° term and it is real. Errors in the depth and earth model have only influence this term. With a change of the dip of the fault plane, a $S^{dip-slip}$ term enters in the excitation term (see equation 2.14). This is an imaginary term hence the excitation term becomes complex and gives an initial phase shift. This phase shift is clearly visible when we perturb the dip with $-10°$ (Fig. 2.4, thin dashed line). For all periods shorter $T < 100$ s the initial phase and amplitude are changed. The change in the initial phase at $T = 25$ s is now continuous instead of the jump for the 45° dip fault and there is no significant drop in amplitude of the initial phase. For periods $T > 100$ s the amplitude of $S^{dip-slip}$ is much smaller than that of S^{45° term which explains the unperturbed phase at these periods. In the waveforms the effect of the perturbed initial phase is clearly visible. At short periods the perturbed and unperturbed waveform are very different (Fig. 2.4c), while at larger periods they are almost identical (Fig. 2.4).

Perturbing the rake for this fault-plane solution does not effect the initial phase and amplitude, which can be seen from equation (2.13).

In the next example, shown in figure 2.5, we have used the same source but now located at a depth of 100 km. Again the initial phase is very sensitive for perturbations in the source parameters at the frequency where the combination of eigenfunctions is zero. This occurs now at a longer period since the earthquake depth h is larger (Fig. 2.3d). The effect of the perturbed dip is visible over the whole period range while perturbing the source depth only influences the longer periods. Changing the earth model from PREM to SNA has a dramatic effect on the longer periods. This is caused by the fact that the zerocrossing of the eigenfunctions of these models appear at different depths.

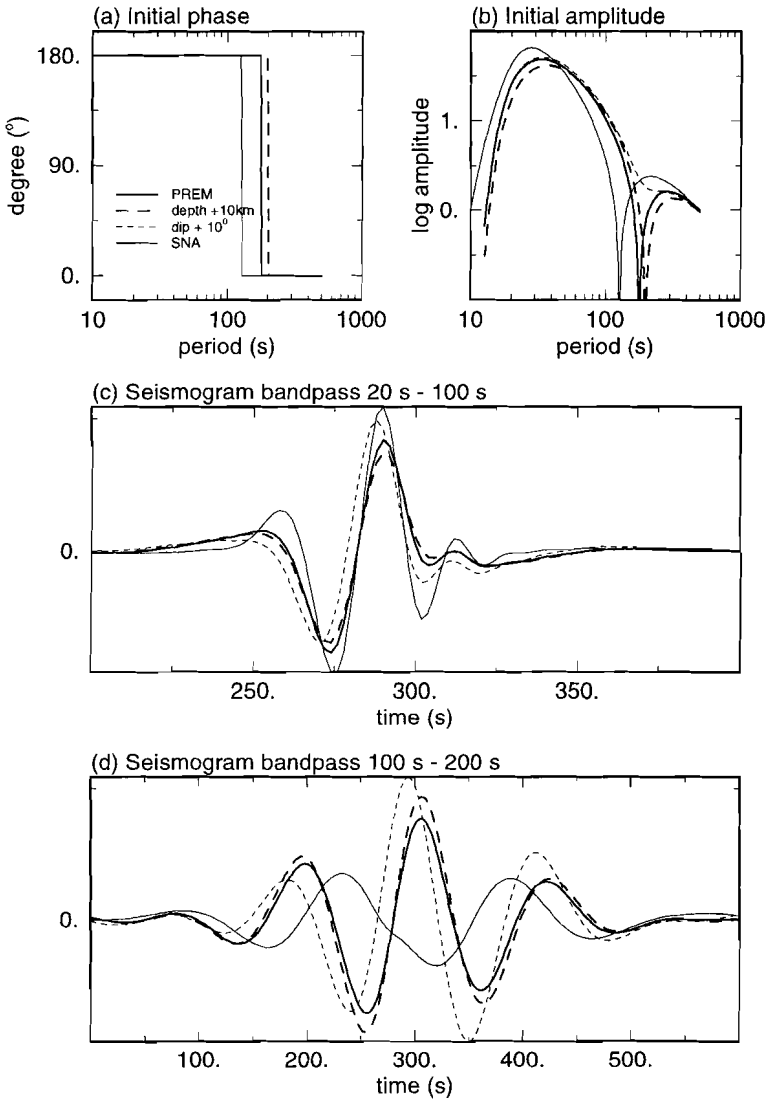

Figure 2.5: Same as Figure 2.4 but now with source at $h = 100$ km, the thick dashed line represents a source at depth $h = 110$ km.

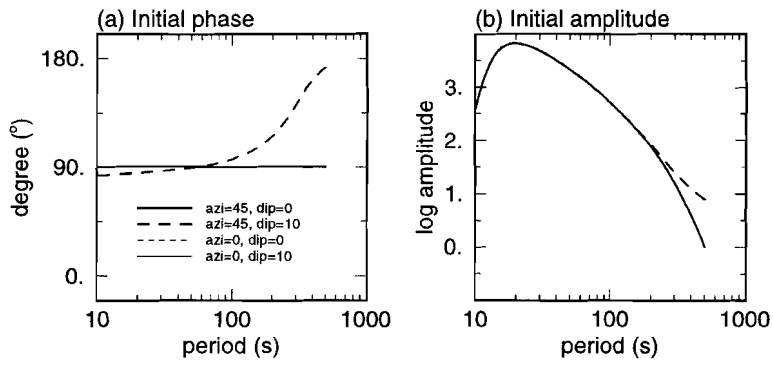

Figure 2.6: (a) The initial phase for a fundamental mode Rayleigh wave for a horizontal fault plane ($h = 50km$, $\delta = 0°$, $\lambda = 0°$). The thick solid line represents the unperturbed case ($\delta = 0°$, $\phi_r = 0°$), thick dashed line a perturbed dip ($\delta = 10°$, $\phi_r = 0°$), thin dashed line for station at different azimuth ($\delta = 0°$, $\phi_r = 45°$) and thin solid line for different azimuth and perturbed dip ($\delta = 10°$, $\phi_r = 45°$). (b) The initial amplitude for the same sources as in (a).

In Figure 2.6 the initial phase and amplitude of a horizontal fault plane at a depth of 50 km is shown. As we can expect from the shape of the combination of eigenfunctions for this source, see Figure 2.3b and equation (2.12), no drop in amplitude or phase reversal is observed. Changing the dip to $+10^0$, an azimuth dependent $S^{45°}$ term enters the excitation term. At azimuth $\phi_r = 0$ this term is zero. At $\phi_r = 45°$ it is not zero and for long periods the initial phase is significantly perturbed because the combination of eigenfunctions for the horizontal fault decreases faster with period than the strike-slip and dip-slip case.

From these examples we see that large uncertainties in the initial phase of the Rayleigh wave due to errors in the fault-plane solution have two causes. First, when the combination of eigenfunctions present in an elementary excitation term at a certain frequency has a zero crossing we can expect large errors in the initial phase in its neighborhood. This follows from the examples with the perturbed depth and azimuth and where different eigenfunctions are used near the source. Second, when a fault-plane solution is close to an elementary fault plane, the excitation terms related to other elementary excitation terms are nearly zero. These terms can grow rapidly when small perturbations in the source parameters dip, rake and strike are considered. This is illustrated by the example with the horizontal fault as shown in Figure 2.6 and the examples with the perturbed dip.

2.6 Fundamental Love wave

The excitation of Love waves is different from Rayleigh waves. First, the azimuthal dependency of the radiation pattern differs from the Rayleigh waves (see equations 2.3 and 2.4). Second, the eigenfunction of the fundamental Love wave does not have a zerocrossing, hence this source of error does not exist. However, the initial phase of Love waves can have large uncertainties when the fault-plane is near an elementary fault-plane. In Figure 2.7 (thick solid line) the initial phase and amplitude for a horizontal fault plane is shown. A small increase of the dip introduces an S^{45° term that causes a large amplitude increase and phase change (Fig. 2.7, thin dashed line). Due to the fact that the eigenfunction for Love waves does not have a zerocrossing, perturbing the depth or the earth model has no influence on the initial phase (Fig. 2.7, thick dashed line and thin solid line).

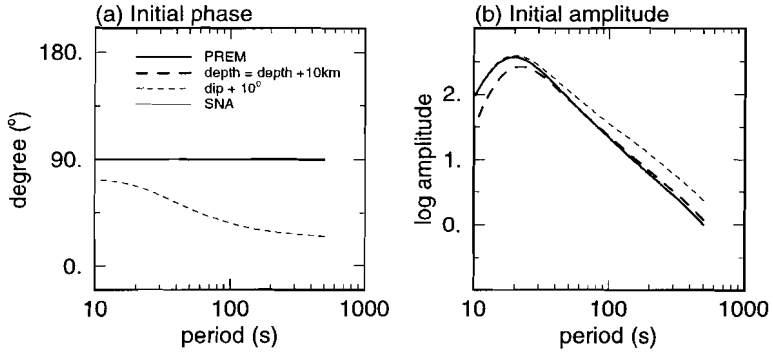

Figure 2.7: (a) Initial phase for fundamental mode Love wave for a horizontal fault plane ($h = 50$ km, $\delta = 0^\circ$, $\lambda = 0^\circ$, $\phi_r = 90^\circ$). The thick solid line represents the unperturbed case, the thick dashed line a source at $h = 40$ km, the thin dashed line a dip $\delta = 55^\circ$ and the thin solid line the SNA model at the source. (b) Initial amplitude for the same sources as (a).

2.7 Higher modes

All eigenfunctions for both Love and Rayleigh higher modes have zerocrossings. The number of zerocrossings in an eigenfunction increases with the mode number n. As a consequence, the elementary excitation terms for individual higher mode Love and Rayleigh waves are sensitive to errors near all their zerocrossings. Because of this, the initial phase of a single higher mode is as sensitive for variations in source parameters as the fundamental Rayleigh wave. However, the waveform resulting of a sum of higher modes is often not strongly effected by such a zerocrossing because the amplitude of the other higher modes is in general not affected. It is therefore more useful to look at the phase difference between the perturbed

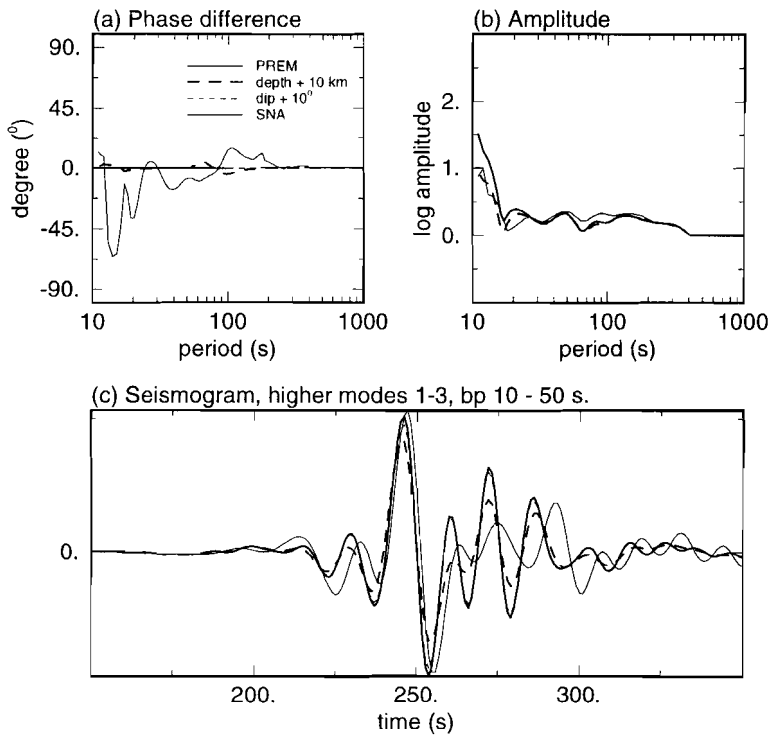

Figure 2.8: (a) Phase difference between the seismograms of the perturbed and unperturbed source for the sum of the first, second and third overtone Rayleigh wave for a fault dipping $\delta = 45°$. (b) The amplitude spectrum. (c) Seismograms bandpassed between $10 < T < 50$ s.

and unperturbed waveform at the station then to look at the initial phase for each mode. In Figure 2.8, this phase and amplitude difference and the waveform for the sum of the first, second and third Rayleigh higher modes are shown, for the same source as in Figure 2.4 (a 45° dipping source at a depth of 20 km). We see that the main characteristics of the phase and amplitude, and the waveform are not sensitive to perturbations in the dip, depth, and earth model near the source.

The second source of errors in the excitation term, which occurs when small changes in the fault plane causes large variations in elementary excitation terms, is not negligible for the higher modes. This can be seen in Figure 2.9 (thick solid line) where we show the case of a horizontal fault plane as in Figure 2.6. Changing the dip with 10° introduces an S^{45° term in the excitation term for all the higher modes and results in large phase shifts in the measured wave (Fig. 2.9, thin dashed line). Large changes in the initial phase also occur when a wrong earth model is used in the excitation term (Fig. 2.9 thin solid line). Since this seismogram is very sensitive for errors in the dip and source model it can not be used for phase measurements or waveform fitting.

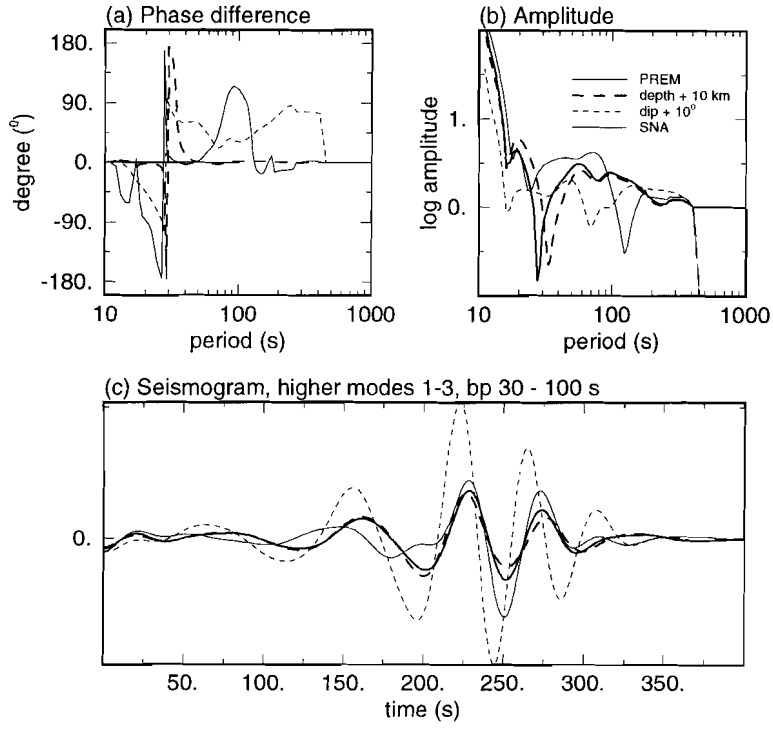

Figure 2.9: (a) Phase difference between the seismograms of the perturbed and unperturbed source for the sum of the first, second and third overtone Rayleigh wave for a horizontal fault as in Figure 2.6. (b) The amplitude spectrum is shown. (c) The seismograms bandpassed between $30 < T < 100$ s are shown.

2.8 Partial derivative of the initial phase

In this section we propose a method by which one can detect frequency bands in the seismogram that are sensitive to source errors. When we know these frequency bands, we can remove these frequency components from the data to avoid errors in the measurement of the phase velocity due to errors in the source parameters.

In the previous sections we have found these frequency bands by calculating seismograms for small perturbations in the source parameters. Instead of calculating many seismograms for all possible uncertainties in the source parameters one can compute the partial derivatives of the initial phase with respect to the source parameters. The partial derivatives of the initial phase can be obtained from equation (2.15) in combination with equation (2.3) or (2.4). The value of the partial derivatives can be used to estimate the error in the phase-velocity measurement due to uncertainties in the source parameters. If it exceeds a certain value it is likely that the phase velocity measurements are contaminated with errors in the

source parameters.

For the events shown in Figure 2.1 we have calculated the partial derivatives of the initial phase φ with respect to the source parameters p_i (dip, rake, azimuth and depth). These partial derivatives are shown in Figure 2.1 column d. The partial derivatives for dip, rake and strike are dimensionless. So for $\partial\varphi / \partial p_i = 1$ a change in one of the source parameters dip, rake or strike of 1° changes the initial phase 1°. The partial derivative $\partial\varphi / \partial p_i$ for depth has the unit 1° so here a change in the depth of 1 km gives rise to a changes in the initial phase of 1°. For the events with a good fit of the data with the synthetics, namely 90107, 90194, 91031, 91195, 93247, all the partial derivatives have $\partial\varphi / \partial p_i < 1$, see Figure 2.1d. These events have a stable initial phase. Events 90135 and 93261 have a poor fit at $150 < T < 200$ s but have a good fit for $70 < T < 100$ s. This observation coincides very well with the behavior of the partial derivatives as function of frequency since $\partial\varphi / \partial p_i \geq 1$ occurs is only at long periods. Both events have a fault plane with $\delta \simeq 45°$ for which a frequency dependent error in the initial phase of the fundamental mode can be expected. However the higher modes for this kind of fault plane are not sensitive to errors in the source parameters as we showed before. For the events 90135 and 93261 this can seen in the data in Figure 2.1a. At $150 < T < 200$ s the higher modes arrive before 1000 s and fit very well, the fundamental mode energy arrives after 1000 s and shows a phase shift, probably due to a high sensitivity to the source parameters. Event 92141 is poorly fit at both $150 < T < 200$ s and $70 < T < 100$ s. This event has a nearly horizontal fault plane which according to our results a large sensitivity of the initial phase to the dip of the fault plane. We see that $\partial\varphi / \partial\delta \geq 1$ for periods between $50s$ and 300 s. The higher modes for this event are also sensitive to errors which explains the poor fit of the first part of the long period signal. Event 93204 is only slightly sensitive to errors in the initial phase. The worse fit here can be caused by a location or time error. Finally, the fit of event 93334 at $70 < T < 100$ s can be explained by the instabilities in the spectrum of the partial derivatives at $T = 40$ s but at $150 < T < 200$ s the fit is also not good. This event is probably too close to a node in the radiation pattern. From this data example we conclude that the partial derivative of the initial phase can be used to define period ranges of stable and unstable measurement.

2.9 Conclusions

The surface wave data set presented in this paper indicates that errors in the source parameters can lead to significant changes in the phase velocities inferred from this data set. These changes are not caused by unmodeled 1D structure or due to the fact that we might be close to a node in the radiation pattern, or by errors in the origin time and epicenter.

Synthetic experiments show that small uncertainties in the fault plane parameters, dip, rake, strike and depth can cause large frequency dependent errors in the phase of fundamental mode Rayleigh waves. Also for the fundamental Love wave and higher modes these errors are not negligible. The unstable behavior of the initial phase occurs (1) when the combination of eigenfunctions present in the excitation term has a zerocrossing at the depth of the source at a certain period we get instabilities near this near period, (2) when the fault-plane is close a an elementary fault-plane.

The partial derivatives of the initial phase can be used to identify the periods of high uncertainty without looking at the data. These periods should be removed from the phase measurements or should be given a high uncertainty. In the dataset shown in this paper a good agreement is observed between outliers in the data and large partial derivatives of the source parameters.

Chapter 3

An alternative parameterization for surface waves in a transverse isotropic medium

3.1 Abstract

The elastic properties of the earth can only be retrieved by seismic waves when assumptions about the seismic anisotropy are made. One such an assumption is to assume that the earth is transverse isotropic. In a transverse isotropic earth Love waves are sensitive to 2 independent elastic parameters and Rayleigh waves to 4 parameters. In addition these waves are sensitive to density. However, resolving 4 elastic parameters together with density as function of depth from Rayleigh waves phase velocity curves is difficult as the large number of parameters can make the inverse problem easily under-determined. We show that the partial derivatives of fundamental and higher mode Rayleigh wave phase velocities with respect to the parameters of transverse isotropy for periods $20 < T < 200$ s are very similar to each other. This means that the inversion of Rayleigh phase velocity data has intrinsic trade-offs. We show that Rayleigh wave data can only resolve 3 combinations of parameters of the transverse isotropic medium : the S-velocity β_V, the sum of the horizontal and vertical P-velocity $\alpha_+ = \frac{1}{2}[\alpha_H + \alpha_V]$ and their difference $\alpha_- = \frac{1}{2}[\alpha_H - \alpha_V]$. The influence of α_- is limited to only the upper 100km earth. For this parameter-set the influence of the density is small and we think it cannot be resolved when realistic variations in all parameters are considered. For Love waves the only relevant parameter is β_H as β_V and ρ can not be resolved. We support our conclusions by a synthetic experiment where the bias in the inversion of Rayleigh wave phase velocity is investigated when the data is inverted for the reduced alternative parameter-set.

This chapter has been submitted for publication.

3.2 Introduction

Seismic wave propagation in the earth is determined by the elastic properties and density of the earth. Most seismological studies only consider variations in the isotropic P-and S-velocities. However, since Hess (1964) provided evidence for anisotropy in the oceanic lithosphere, seismologists have determined the anisotropic properties of the earth, an overview of such studies is given by Babuska and Cara (1991). Surface waves are a primary tool for the investigation of the earths anisotropic properties. Transverse isotropy was, for example, required to explain the Love-Rayleigh discrepancy present in the surface wave data used for the PREM model (Dziewonski and Anderson, 1981). Transverse isotropy is a simple type of anisotropy which has only one symmetry axis in either the vertical or horizontal direction. Transverse isotropy has also been observed in the oceanic lithosphere (Cara and Leveque 1987, 1988; Nishimura and Forsyth (1989). Surface waves have also been used to map the large scale variations in the azimuthal properties of the earth (Tanimoto and Anderson 1985; Montagner and Tanimoto, 1991). Inversions of surface wave data for the density structure have been carried out by Nolet (1977); Cara et al. (1984) and Tanimoto (1991).

Determination of the full elasticity tensor c_{ijkl} with its 21 independent parameters in the earth is beyond the resolving power of the seismic data. Analysis of the partial derivatives of surface waves has shown that there are only 13 combinations of elastic parameters that can be resolved (see Smith and Dahlen 1973, Crampin, 1984, Montagner and Nataf, 1986). However, between these 13 combinations of elastic parameters strong correlations do exist between the parameters as has been shown for realistic petrological models of the upper mantle (Montagner and Anderson, 1989). For data along a given source-receiver path the number of independent parameters is even smaller (Maupin, 1985). In that case the partial derivatives for the general anisotropic medium can be written as a linear combination of those for the transverse isotropic medium with vertical symmetry axis. This means that for a given source-receiver path, Rayleigh waves are sensitive to only 4 combinations of elastic parameters and density while Love waves sample only 2 independent combinations of elastic parameters and density.

In this paper we show that for a well-posed inversion of fundamental and higher mode Love and Rayleigh phase velocity data with periods between $20s < T < 200$ s a further reduction of the number of independent parameters is required. For fundamental mode data this observation is not surprising as typically 10-15 measurements are available for inverting 4 elastic parameters and density as a function of depth. The parameters in such an inversion can be better constrained when higher modes are added to the data set. However, we show that the parameters for transverse isotropy have inherent trade-offs. We propose an alternative parameter-set that does not have these trade-offs. This alternative parameter-set is built from linear combinations of the elastic parameters in such a way that it has a minimum of trade-offs. We investigate the relative importance of these parameters in combination with density and show that we can resolve only 3 com-

binations of parameters instead of $4+1$ parameters. We illustrate this statement with an experiment in which we invert phase velocity data, computed for the full parameter-set, for the reduced alternative parameter-set.

3.3 Transverse isotropy

Wave propagation in transverse isotropy is sensitive to 5 independent elastic parameters (A,C,L,N,F) and density (see Love, 1927). In Table 3.1 the definition of this so called Love parameter-set is given in terms of seismic velocities, the fourth order elasticity tensor c_{ijkl} and its shorthand notation C_{ij}. The interpretation of the elastic parameters A, C, L, N is straightforward, that of F is more complicated. By definition, $F = c_{3311} = c_{3322}$ which indicates that F is related to the velocity of a wave propagating in the vertical plane between source and receiver. Throughout this paper we denote this velocity by γ. Anderson (1961) has given an expression for F as function of a wave at 45° incidence of the vertical axis and introduced the parameter $\eta \equiv \frac{F}{A-2L}$ (here η is given in the notation of Takeuchi and Saito (1972) which is the inverse of Anderson's definition). In isotropy $F = A - 2L$ and $\gamma^2 = \alpha^2 - 2\beta^2$.

Linearized inversion of surface wave dispersion measurements can be carried out using the partial derivatives of the phase velocity with respect to the model parameters. For Love waves such an inversion is based on equation 3.1 which relates the relative variation in phase velocity $\delta c/c$ to integrals of the variations in the medium with depth.

$$\left(\frac{\delta c}{c}\right) = \int_{z=0}^{R} \frac{L}{c}\left[\frac{\partial c}{\partial L}\right]\frac{\delta L}{L}dz + \int_{z=0}^{R} \frac{N}{c}\left[\frac{\partial c}{\partial N}\right]\frac{\delta N}{N}dz + \int_{z=0}^{R} \frac{\rho}{c}\left[\frac{\partial c}{\partial \rho}\right]\frac{\delta \rho}{\rho}dz \quad (3.1)$$

In equation 3.1 the terms between brackets, $\left[\frac{\partial c}{\delta}\right]$, are the partial derivatives to the model parameters. The unit of the the terms like $\frac{L}{c}\left[\frac{\partial c}{\partial L}\right]$ are reciprocal length. Details about the computation of the partial derivatives can be found in Takeuchi and Saito (1972). For Rayleigh waves a relation similar to equation 3.1 but with terms for (A, C, L, F, ρ) is commonly used.

Love (1927) Parameters	Velocity	Elasticity tensor	Matrix notation
A	$\rho\alpha_H^2$	c_{1111}	C_{11}
C	$\rho\alpha_V^2$	c_{3333}	C_{33}
L	$\rho\beta_V^2$	$c_{2323} = c_{1313}$	$C_{44} = C_{55}$
N	$\rho\beta_H^2$	c_{1212}	C_{66}
F	$\rho\gamma^2$	$c_{3311} = c_{3322}$	$C_{31} = C_{32}$

Table 3.1: Definition of the Love parameters

The partial derivatives of the Rayleigh waves for the Love parameter-set at 6 frequencies and modes are shown in the left panels of Figure 3.1. These partial derivatives have been computed for the equivalent isotropic PREM model (Dziewonski and Anderson 1981). An important observation made from Figure 3.1 is that the higher mode partial derivatives for $\frac{\partial c}{\partial A}$, $\frac{\partial c}{\partial C}$ and $\frac{\partial c}{\partial F}$ all have an almost identical shape but different amplitude. Because of this similar shape it is not possible to resolve the parameters A, C, and F independently using higher mode Rayleigh wave data alone. This is in contrast to the fundamental mode partial derivatives for A, C, and F that have significant differences in the upper 100 km. An other interesting observation is that for higher modes, $\frac{\partial c}{\partial A}$, $\frac{\partial c}{\partial C}$, $\frac{\partial c}{\partial F}$ are more sensitive to structure at shallower depths than $\frac{\partial c}{\partial L}$. This is due to the fact that the partial derivative for L is determined by S-motion while those for A, C and F are determined by P-motion. The partial derivative for the density is a mixture of the P-and S-motion and has a negative sign.

An other parameter-set for transverse isotropy has been proposed by Anderson (1961). He introduced the parameter η for transverse isotropy and used velocities instead of elastic parameters. The Anderson parameter-set (α_H, α_V, β_H, β_V, η) is derived from the Love parameter-set by differentiation. This parameter-set has been used for the construction of the PREM model (Dziewonski and Anderson, 1981). In the middle panels of Figure 3.1 we show the partial derivatives for the Anderson parameter-set. The definition $F \equiv \eta(A - 2L)$ introduces additional partial derivatives for β_V and α_H which change the shape of the partial derivatives for these parameters significantly (see Figure 3.1). The partial derivative $\frac{\partial c}{\partial \eta}$ has the same shape as $\frac{\partial c}{\partial F}$. For the fundamental mode $\frac{\partial c}{\partial \alpha_H}$ has a zero crossing while for the higher modes it becomes negative and $\frac{\partial c}{\partial \alpha_H} \approx -\frac{\partial c}{\partial \alpha_V}$. Thus for the higher modes an increase in horizontal P-velocity results in a decrease in phase velocity which is entirely caused by the additional partial derivative $\frac{\partial c}{\partial F}\frac{\partial F}{\partial \alpha_H}$. The additional term $\frac{\partial c}{\partial \beta_V}$ introduced by Anderson's definition of F causes an inherent trade-off between $\frac{\partial c}{\partial \beta_V}$ and the P-partial derivatives $\frac{\partial c}{\partial \alpha_V}$, $\frac{\partial c}{\partial \alpha_H}$, $\frac{\partial c}{\partial \eta}$. As all Love parameters are dependent to density, Anderson's $\frac{\partial c}{\partial \rho}$ has a different shape and is oscillating around zero.

For Love waves in a transverse isotropic medium only the partial derivatives to the elastic parameters, L and N and density are nonzero. In the left panel of Figure 3.2 we show the partial derivatives for these parameters at the same frequencies and modes as the Rayleigh partial derivatives displayed in Figure 3.1. The partial derivative for the density has a similar shape and amplitude but opposite sign as $\frac{\partial c}{\partial N}$. These partial derivatives have a much larger amplitude than $\frac{\partial c}{\partial L}$ of which the influence on the Love wave phase velocity is very small. In Anderson's parameter-set the density partial derivative is negligible for the fundamental mode and only small for the longer periods higher modes (e.g. the fifth higher mode at 50 s), see right hand panel of Figure 3.2.

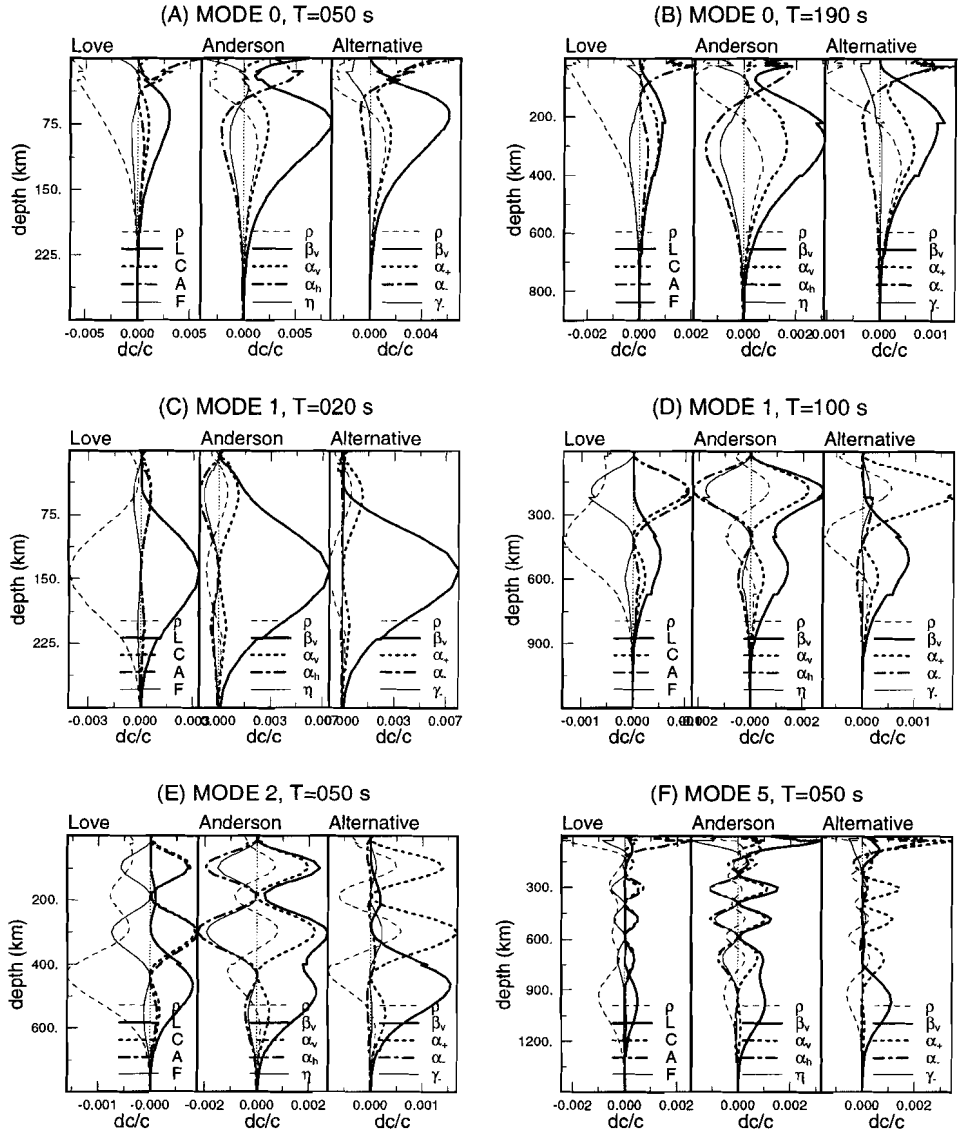

Figure 3.1: Partial derivatives of the Rayleigh wave phase velocity for three parameter sets. The left panels show those for the Love parameter set, the middle panel shows those for the Anderson parameter set and alternative parameter set is shown in the right panel. Ilestyles for the partial derivatives with respect to the various parameters are indicated in the figure. (a) Fundamental mode at $T = 50$ s. (b) Fundamental mode at $T = 190$ s. (d) First higher mode at $T = 20$ s. (d) First higher mode at $T = 100$ s. (e) Second higher mode at $T = 50$ s. (f) Fifth higher mode at $T = 50$ s.

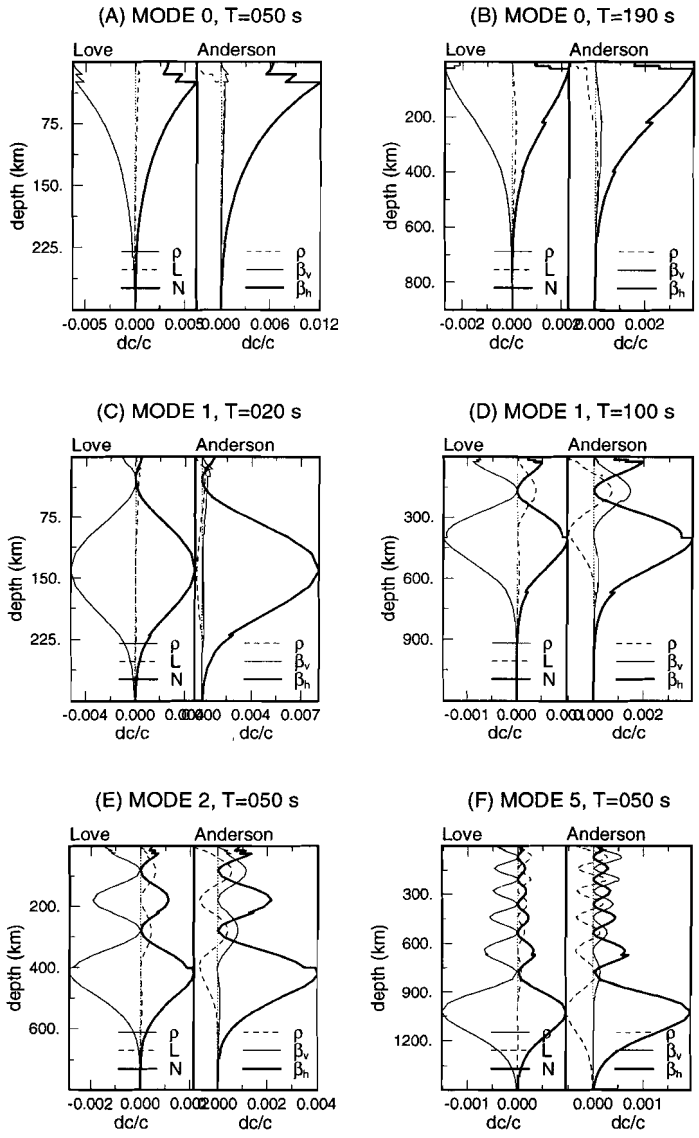

Figure 3.2: Partial derivatives of the Love wave phase velocity for the Love parameter set (left panel) and the Anderson parameters (right panel).

3.4 Alternative parameterization

The analysis of the partial derivatives for the transverse isotropic medium has shown that it is unlikely that all parameters can be resolved from phase velocity data. This is due to some inherent trade-offs present in the parameters A, C, and F. The Anderson parameter-set has even more trade-offs due to the definition of $F = \eta(A - 2L)$. On the other hand, for this parameter-set the influence of the density is much smaller. We therefore propose an alternative parameter-set which is more suitable for the inversion of surface wave data. We use the alternative definition of $F \equiv \rho\gamma^2$ by which no additional partial derivatives for α_H and β_V exist that causes undesirable trade-offs. Using this definition the partial derivatives for α_H, α_V, β_H, β_V and γ have a similar shape for the Love parameters A, C, L, N but the partial derivative for density has the same shape as Anderson's density partial derivative. As $\frac{\partial c}{\partial \alpha_H}$, $\frac{\partial c}{\partial \alpha_V}$ and $\frac{\partial c}{\partial \gamma}$ have a similar shape we define three new parameters : the average of the horizontal and vertical P-velocity $\alpha_+ = \frac{1}{2}[\alpha_H + \alpha_V]$, the difference between the P-velocities $\alpha_- = \frac{1}{2}[\alpha_H - \alpha_V]$ and the difference $\gamma_- = [\gamma - 0.7\alpha_+]$. The factor 0.7 in the definition of γ_- accounts for amplitude differences between $\frac{\partial c}{\partial \gamma}$ and $\frac{\partial c}{\partial \alpha_+}$ and is empirically determined as no analytical relation could be derived.

The partial derivatives for the alternative parameter-set (β_V, α_+, α_-,γ_-,ρ) are shown in the right panels of Figure 3.1. Those of the parameters β_V, α_+, ρ have the largest amplitudes and have very different shapes. We expect therefore that it is possible to resolve these parameters independently. Note that the partial derivative for ρ is identical to Anderson's. The higher modes partial derivatives for α_- and γ_- have a small magnitude and it is therefore unlikely that they can be resolved. For the fundamental mode the partial derivative for γ_- has a larger amplitude but still it is small and is likely to have a trade-off with α_- which depth penetration is also limited to the upper 200 km.

We illustrate the importance of the elastic parameters on the phase velocity by the following example. We perturb the parameters (β_V, α_+, α_-,γ_-,ρ) in the upper 220 km by 1%, below this depth the model is not perturbed. The corresponding phase velocity perturbations with respect to the PREM model have computed using equation 3.1. For the Rayleigh waves the results are shown in Figure 3.3. The influence of β_V on the phase velocity is large as a 1% increase can give a 0.8% change in $\left(\frac{dc}{c}\right)_{\beta_V}$. As the modes penetrate deeper in the earth with increasing period and mode, the effect of a 220 km thick perturbed β_V layer on the fifth overtone is only observable at periods smaller than 20 s. The partial derivative for α_+ penetrate less deep than β_V at the same period thus the variations in $\left(\frac{dc}{c}\right)_{\alpha_+}$ occur at larger periods than for β_V. The influence of a 1% perturbation in α_- and γ_- on the phase velocity is small. We think that it is impossible to retrieve the α_- and γ_- independently because they are both predominantly sensitive to the crust and lithosphere. The sensitivity of γ_- is less then of α_- and therefore we propose to neglect this parameter in the inversion. We cannot also neglect α_-

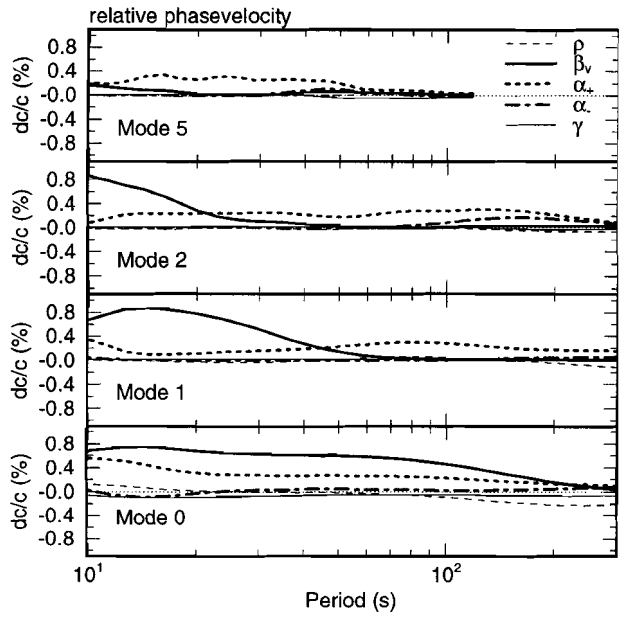

Figure 3.3: Relative Rayleigh wave phase velocity perturbations $\frac{dc}{c}$ as function of period for increase in each model parameter of 1% in the upper 220 km.

as in the crust and lithosphere large variations ($< 10\%$) in the elastic properties occur.

The influence of the density perturbation on the phase velocity is very small, see Figure 3.3. This does not contradict with Tanimoto (1991) who showed that it is possible to retrieve density information from surface waves. Tanimoto used long period data with $T > 100$ s and inverted the data-set only for S-velocity and density. Tanimoto found global density variations in mantle of about 0.5% while β_v varied 7%. Figure 3.3 shows that at these long periods the perturbed S-velocity and density give a similar phase velocity perturbation. There are two reasons why the density can be neglected in the inversion of phase velocity data for periods between $20 < T < 200$ s. First, the oscillatory nature of $\left[\frac{\partial c}{\partial \rho}\right]$ makes it very difficult to resolve the smooth structure of the density profile. In addition, seismologists normally put smoothness constraints on the inversion of phase velocity data that make it impossible to find rough density profiles. Second, the changes in the density of the earth are likely to be smaller than the variations in the elastic parameters. In the continental lithosphere the density can vary up to 3% due to variations in mantle temperature (Vlaar, Van Keken and Van den Berg, 1994). The corresponding variation in phasevelocity is much less than the observed variations in the phase-velocity in the lithosphere. In the sub-lithospheric mantle the density variations are likely to be smaller. Subducting slabs are probabibly the most

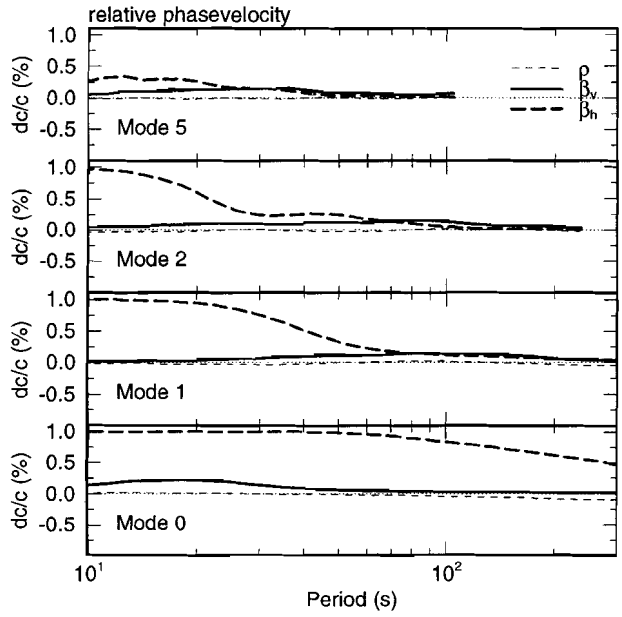

Figure 3.4: Relative Love wave phase velocity perturbations $\frac{dc}{c}$ as function of period for a 1% increase in each model parameter in the upper 220 km.

important source for density variations in the mantle. We estimate the maximum density contrast in a slab in the following way. The center of a slab at 400 km depth has a temperature contrast of 800° with the surrounding mantle (Helffrich, Stein and Wood, 1989; De Jonge, 1995). Given a thermal expansion coefficient for the mantle of $\alpha = 3.510^{-5}K^{-}1$ a maximum density contrast of 3% can be expected. This means that the expected density contrasts in the earth are smaller than the variation in the elastic parameters. A constant density variation of 3% gives a 0.75% variation in the phase velocity, see Figure 3.3. As phase velocity measurement errors are of the order of 1% this is still within the uncertainties, (Nakanishi and Anderson, 1984, Van Heijst et al., 1994). In conclusion we think that it is unlikely that one can resolve the density given its lack of sensitivity to smooth profiles, measurement errors and variations in other parameters.

For the sake of completeness we show in Figure 3.4 the sensitivity of the Love wave phase velocity. The sensitivity of the Love waves to perturbations in β_H is large, a 1% perturbation in β_H results in a $\left(\frac{dc}{c}\right)_{\beta_H}$ of 1%. The sensitivity to density and β_V perturbations is much smaller, by which we do think it is difficult to resolve these parameters from Love wave data.

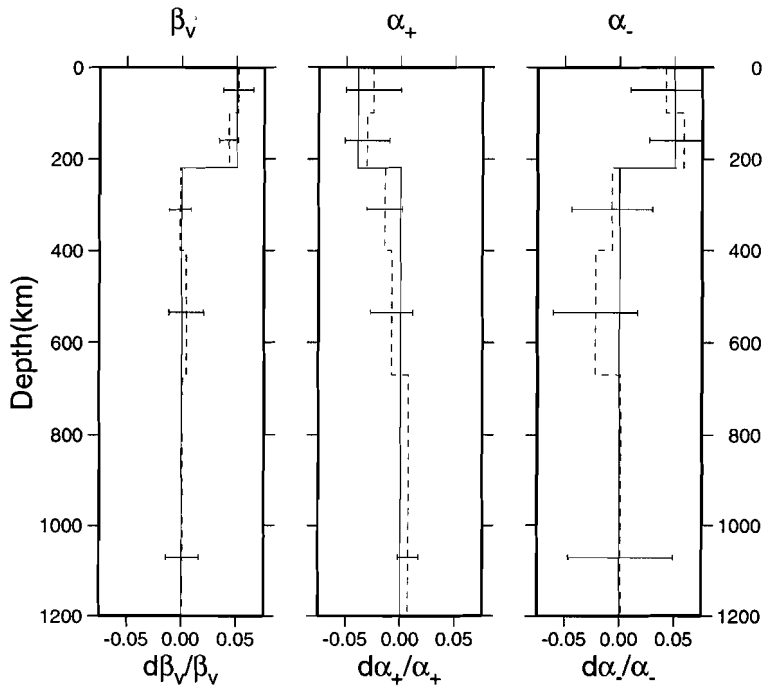

Figure 3.5: Synthetic test of the inversion of phase velocity data. Solid line indicates the input model. The dashed line represents the model obtained by inversion. (a) Inversion results for $\left(\frac{\partial\beta_V}{\beta_V}\right)$. (b) shows the inversion results for $\left(\frac{\partial\alpha_+}{\alpha_+}\right)$. (c) shows the results for $\left(\frac{d\alpha_-}{\alpha_-}\right)$.

3.5 Experiment

In this experiment we investigate the bias in the inversion of Rayleigh phase velocities using the alternative parameterset. Phase velocity perturbations have been computed for an input model that has the following variations in the medium parameters with respect to PREM : $\frac{\delta\beta_V}{\beta_V} = 5\%$, $\frac{\delta\alpha_V}{\alpha_V} = 2.5\%$, $\frac{\delta\alpha_H}{\alpha_H} = 2.5\%$, $\frac{\delta\gamma}{\gamma} = 5\%$, $\frac{\delta\rho}{\rho} = 5\%$. These model parameters are only perturbed in the upper 220 km. Phase velocity perturbations have been computed at 10 frequencies between the periods of 20s to 200s for the fundamental mode up to the fifth higher mode. The dataset is inverted for the reduced parameters (β_V, α_+, α_-). The input model is projected on this parameters using the relations $\alpha_+ = \frac{1}{2}(\alpha_H+\alpha_V)-\gamma$ and $\alpha_- = \frac{1}{2}(\alpha_H-\alpha_V)$. Each parameter is defined over 5 layers.

The inversion is carried out using the algorithm of Tarantola and Valette (1982). The data is assumed to be uncorrelated and thus the covariance matrix

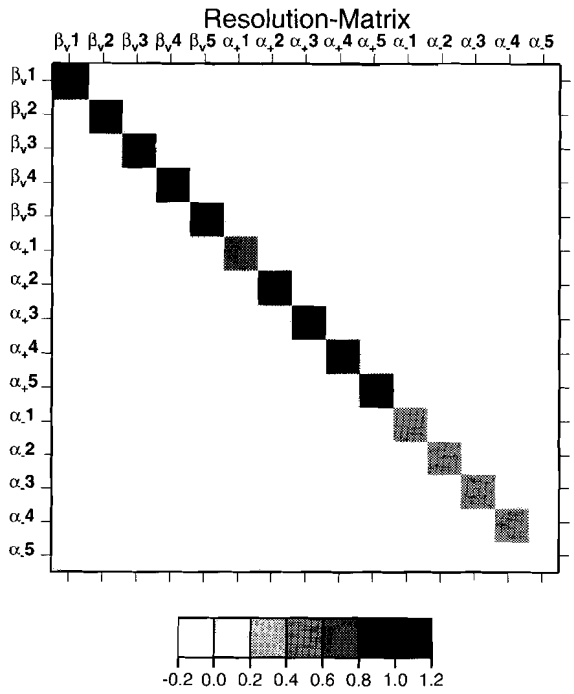

Figure 3.6: Resolution matrix for inversion shown in figure 3.5. The parameters increase for $\beta_V 1$ which corresponds to the top layer of β_V to $\alpha_- 5$ the deepest layer of α_-. Note that the zero contour separates the white region from the light-gray region.

for the data C_D has only diagonal terms which represent the variance. A realistic standard error of 40 m/s has been assigned to the phase velocity data (Nakanishi and Anderson, 1984, Van Heijst et al., 1994). For the a-priori covariance matrix of the model parameters C_m we only take the diagonal elements as nonzero by which C_m acts as norm damping on the inversion. Using a trade-off curve between data misfit and model we have determined an optimum solution which is displayed in Figure 3.5. We see that the inversion reveals the parameters up to a high degree and well within the uncertainties. The best determined parameter, which has the smallest variances is β_V followed by α_+. The poorest determined parameter is α_- and the increase of variance with depth for the parameter reflects the poor depth sensitivity to this parameter. The resolution matrix shows that β_V and α_+ are well resolved, see Figure 3.6. α_- is much poorer resolved, which can be expected from the little depth penetration. The resolution matrix also shows that are little trade-offs between the parameters.

3.6 Discussion

We have shown that for periods $20s < T < 200s$ the inversion of Rayleigh waves in a transverse isotropic medium has some inherit trade-offs. By introducing a new parameter-set we have shown that one can only resolve 3 parameters (β_V, α_+, α_-). For Love waves the modeling results show that only β_H can be resolved. However this parameter-set should be used with some caution. First, we have shown that the density and γ_- are difficult to resolve but this does not mean that they are completely negligible. When additional information about these parameters is available this should be included in the inversion. Second, Love wave data alone can not resolve β_V but this does not mean it's influence is negligable. When a joint inversion of both Love and Rayleigh waves is carried out the shift in the Love phase velocity due to β_V can be taken into account as it is constrained by the Rayleigh wave. Finally, the partial derivative for β_V should not be used for an isotropic inversion of Rayleigh wave data. In that case an additional term for $\left[\frac{\partial F}{\partial \beta_V}\right]$ should be included leading to Anderson's partial derivative for β_V.

The proposed parameterization is particular useful when the earth is modeled by transverse isotropy such as in regional studies of phase velocity data (e.g. Nishimura and Forsyth, 1989) or waveform inversion (see Nolet, 1990). It is interesting to note that in the proposed parameterization, the Rayleigh wave partial derivative for $\left[\frac{\partial c}{\partial \beta_V}\right]$ has a shape very similar as the Love wave partial derivative for $\left[\frac{\partial c}{\partial \beta_H}\right]$.

This parameterization can also be used for a more general anisotropic medium. Maupin (1985) has shown that for a given source-receiver path, the partial derivatives of the general anisotropic medium can be written as linear combination of those for the transverse isotropic medium. Instead of using the partial derivatives for the Anderson parameter-set one can use our proposed parameter-set which has less trade-offs.

Chapter 4

A seismic cross section through the East European continent

4.1 Abstract

A two-dimensional profile for the shear wave velocity and anisotropy between Egypt and Spitsbergen is presented. The profile is constructed using fundamental and higher mode Love and Rayleigh waves recorded by stations of the NARS-DEEP, IRIS and GEOFON networks. The surface wave data has been inverted for shear velocity and anisotropy using a waveform inversion. In the Eastern Mediterranean lithosphere we observe a large difference (7%) between SH and SV velocities. We interprete this anomaly as anisotropic oceanic lithosphere beneath the Eastern Mediterranean, an interpretation which is consistent with tectonic reconstructions of the region. The East European continent is imaged as a high velocity body of which thickness increases with lithospheric age. The continental root of the Ukrainian and Baltic shields and East European Platform extends to a depth of 200 km. This in contrast with the surrounding younger continental regions which appear to be less than 100 km. We further have studied the structure of the continental lithosphere by investigating a possible relation between seismic velocities and tectonic age. Both a logarithmic and a square root relationship have been fitted to the average seismic velocities in each tectonic region. The data slightly favors a logarithmic relation but a square root relation can not be excluded.

4.2 Introduction

The East European continent consist of a variety of tectonic units ranging from possible oceanic plates (Eastern Mediterranean) to the archean Ukrainian and Baltic Shields. The crustal structure of region is well studied, e.g. Pavlenkova

This chapter has been submitted for publication

(1996), but the structure of the lithosphere is poorly known. Considerable heterogeneities in the East European lithosphere have been observed down to a depth of 300 km using P-wave travel-time data (e.g. Husebye and Hovland 1982; Grad, Kryzanowska and Pirhonen 1995). Recent higher mode surface wave studies have mapped the transition from phanerozoic Western European toward precambrian East European Platform along the Tornquist-Teisseyre zone and revealed a difference in seismic velocities down to 300 km depth (Zielhuis and Nolet, 1994ab; Marquering and Snieder, 1996). However, high resolution tomographic studies of the East European Platform have not yet been performed due to the lack of digital broadband seismic stations.

Seismological data put important constraints on models of the evolution of the continental lithosphere (Jordan, 1981; Durrheim and Mooney, 1994). The basic idea in such theories is that chemical content and the thickness of the continents varies with lithospheric age due to the increased mantle temperature in the Archean. One such observation is the increase of crustal thickness with lithospheric age (Meissner, 1986; Durrheim and Mooney, 1994). Other important seismological observables are the thickness of the continental lithosphere and changes in velocities due to temperature and chemical variations in the continental lithosphere. The poor knowledge of the continental lithosphere is in contrast to the knowledge of the oceanic lithosphere (Sclater, Jaupert and Galson 1980). Heat flow and bathymetry in oceanic lithosphere older than 80 Ma follows a logarithmic relation instead of a square root relation. Such a logarithmic relation is predicted by a cooling model of a 125 km thick lithospheric plate.

In this study we present a two-dimensional model for shear velocity and anisotropy from Egypt to Spitsbergen. This profile connects three earthquakes in the Eastern Mediterrean and Spitsbergen with 7 stations in the region. The locations of these stations allow us to determine the seismic velocities of several tectonic units such as the Eastern Mediterranean Sea, the East European Platform and the Baltic Shield, see Figure 4.1a. The main data source are four stations of the NARS-DEEP network that has been installed along a line from Odessa to St. Petersburg, thus covering the East European Platform, see Snieder and Paulssen (1993). In addition we use data from several recently installed IRIS and GEOFON stations in the region.

The data-set, which consists of fundamental and higher mode Love and Rayleigh waves, is inverted using a partitioned waveform inversion analogous to Nolet (1990). Such a waveform inversion has the advantage over dispersion measurements that it is not necessary to identify the modes in the seismogram. Interference of higher modes with each other and of higher modes with the fundamental mode is implicitly taken into account and does not bias the inversion. We illustrate the lateral and depth resolution of the waveform inversion by a synthetic test. It is well known that the inversion of Love and Rayleigh waves can lead to different SH and SV models, e.g. Babuska and Cara (1991). As such a Love-Rayleigh discrepancy is also present in our data set we include anisotropy in the inversion.

We discuss the lateral variation and the depth extend of the anomalies in the

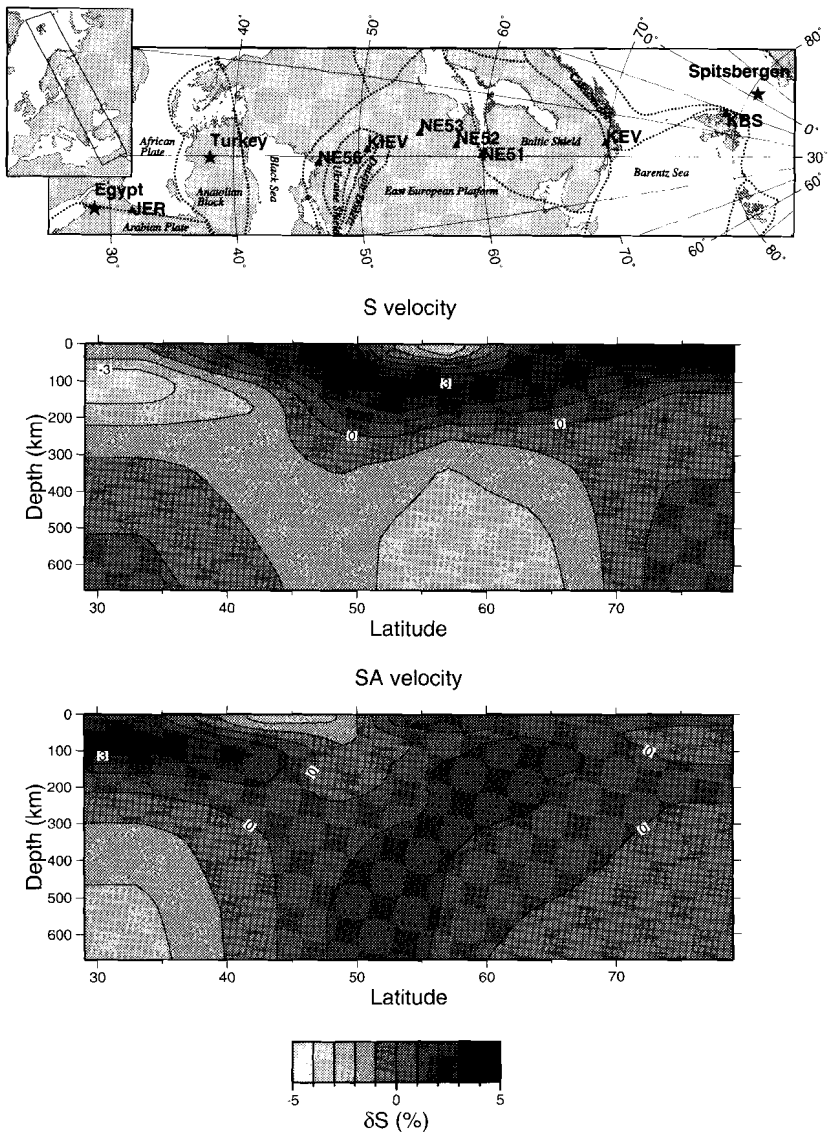

Figure 4.1: (a) Map along the profile Egypt-Spitsbergen along the 30°E meridian showing stations (triangles), event locations (stars) and the tectonic regions after Zonenshain et al. (1990). (b) S-velocity model of the lithosphere and mantle between Egypt and Spitsbergen. (c) Apparent anisotropy SA model for the same region.

model and relate these to the tectonic history of the regions. The seismic velocities and anisotropy of the Eastern Mediterranean lithosphere are strikingly different than in the continent and therefore we discuss this region in a separate section. In the last section we investigate a possible relation between seismic velocities in the continental lithosphere and tectonic age.

4.3 Data

We have collected data from three strong earthquakes. Two events took place in the Eastern Mediterranean: Turkey, October, 1, 1995, $M_w = 6.0$ and Egypt, November 22, 1995, $M_w = 7.2$. The third event is located in the Northern Atlantic Ocean (Spitsbergen, May, 14, 1996, $M_w = 5.7$). The epicenters of these earthquakes are located on a great-circle connecting 8 seismic stations in Eastern Europe and the Eastern Mediterranean for which data were available, see figure 4.1A, Table 4.1. Along them are the NARS-DEEP stations NE51 (St. Petersburg, Russia), NE52 (Pskov, Russia), NE53 (Naroch, Belarus) and NE56 (Odessa, Ukraine). Together with the NARS-DEEP data we use registrations from the IRIS stations KEV (Kevo, Finland), KBS (Kingsbay, Spitsbergen) and KIEV (Kiev, Ukraine). In addition we include recordings of the Spitsbergen event by the GEOFON station JER (Jericho, Israel). Data from other stations and events in the region were either of poor quality or not available.

The seismograms have been corrected for instrumental response and after visual inspection for noise, 14 transverse component seismograms and 16 vertical components seismograms were available for surface wave analysis. The vertical component seismograms show strong fundamental and higher mode Rayleigh waves

Station	**latitude** ($^\circ N$)	**Longitude** ($^\circ E$)
JER	31.72	35.18
NE51	59.88	34.82
NE52	57.82	28.39
NE53	54.90	26.79
NE56	46.78	30.88
KEV	69.75	27.00
KBS	78.92	11.92
KIEV	50.69	29.21
Egypt event	28.81	34.86
Turkey event	38.10	30.18
Spitsbergen event	80.78	-2.27

Table 4.1: Station locations and epicenters of earthquakes

together with S and SS phases. Due to the shallow source depth of the events, the transverse component seismograms contain mainly strong fundamental mode Love waves and poorly developed higher modes and body wave phases. All waveforms have been checked for sensitivity to uncertainties in the source parameters, see Muyzert and Snieder (1996).

4.4 Waveform inversion

The seismic velocities between the stations and earthquake locations have been determined by a partitioned waveform inversion similar to the method developed by Nolet (1990). This is a two step method. First, each seismogram is inverted for the path-averaged shear velocity structure. Both Love and Rayleigh, fundamental and higher modes have been inverted from the direct S wave up to the fundamental mode arrival. In the second step all path-averaged velocity functions are combined and inverted for the lateral velocity variations between the stations. In this step anisotropy has been introduced in the model as no satisfactory data fit were found for isotropic models.

In the first step of the inversion procedure the seismograms are filtered both in time and frequency in order to separate phases. The fundamental mode is filtered into two different windows with frequencies between 0.01 - 0.03 Hz and 0.005 - 0.01 Hz. In addition two higher mode windows have been defined, one around the S, the other around the SS phases, both at frequencies between 0.016 - 0.05 Hz. At the shorter distances the S and SS phases could not be separated and a window containing both phases has been used. For Love waves at shorter distances a window is chosen which contains the SS phase and the fundamental mode.

The seismograms are inverted using the objective function defined by :

$$F(\mathbf{m}) = \int [D(t) - S(t, \mathbf{m})]^2 dt + \gamma_{\mathbf{m}} \tag{4.1}$$

(see Nolet, 1990). In equation (4.1), $D(t)$ and $S(t, \mathbf{m})$ are the filtered data and synthetic seismogram computed for the path averaged velocity model $\mathbf{m}$. The term $\gamma_{\mathbf{m}}$ denotes a regularization term which is a two-point smoothing operator that penalizes vertical gradient of the model. Equation (4.1) is minimized using the conjugated gradient method. To prevent the inversion from being trapped in local minima, first long-period fundamental modes are inverted. In further iterations the depth resolution is increased by adding the higher modes windows and higher frequencies to the objective function.

The model parameters of the waveform inversion are the relative perturbation in the horizontal and the vertical shear velocity, $SH(z)$ and $SV(z)$. The shear velocity model is parameterized in 9 layers with increasing thickness. The top layer is the crustal layer with a thickness of 40 km. The bottom layer is defined from 670 km depth to the core mantle boundary. The starting model for the inversion has a Moho depth of 40 km and between 40 km and 220 km a constant

shear velocity of 4.5 km/s. Below 220 km depth the PREM model (Dziewonski and Anderson, 1981) is used. For the waveform modeling ISC locations and Harvard source mechanisms have been used. A crustal correction has been applied on each seismogram using the CRUST5.1 model (Mooney, Laske and Masters, 1996). The crustal correction is the sum of the local phase velocities in each cell of the $5° \times 5°$ crustal model along the source receiver path. Thus the seismograms include the effect of the variation in crustal structure, Moho depth and water layer. The application of the crustal correction has resulted in a smaller difference between SH and SV velocities in the layer directly below the Moho in the final model.

In the second step of the inversion the path-averaged velocity perturbations are inverted for the inter-station velocities. In this inversion the cell boundaries have been defined by the latitudes of the earthquakes and stations. The only exception is on the East European Platform where a cell ranging from NE53-NE51 has been defined as tests indicated that the cell NE52-NE51 could not be resolved due to its small horizontal length.

As we will show later, a Love-Rayleigh discrepancy is present in our data-set. We therefore include anisotropy in the inversion. A commonly used parameter-set for the inversion of surface waves is SV and $\xi = (SH/SV)^2$. This parameter-set is useful for the inversion of phase velocities but not but for the path-averaged velocity functions as it results in a non-linear inversion for $SH(z)$. Instead we define the average shear velocity $S = (SH + SV)/2$ and the apparent shear wave anisotropy $SA = (SH - SV)/2$. The relation between the path-averaged velocity functions and S and SA is linear. Another advantage of this parameter-set is that the S velocity has only little dependence on SA while the estimate for SV has an implicit tradeoff with ξ. Furtheron in this paper the symbols S and SA refer to the relative variations in these parameters.

The inversion of the path-averaged velocity function for S and SA is a linear inversion and is regularized by both smoothing and norm damping of the model. This results in the following set of linear equations that is solved in the least-squares sense (see Paige and Saunders, 1982) :

$$\begin{bmatrix} \mathbf{A_1} & 0 \\ \eta\mathbf{G} & 0 \\ 0 & \mathbf{A_2} \\ 0 & \eta\mathbf{G} \\ 0 & \mu\mathbf{I} \end{bmatrix} \begin{bmatrix} S \\ SA \end{bmatrix} = \begin{bmatrix} SH + SV \\ 0 \\ SH - SV \\ 0 \\ 0 \end{bmatrix} \tag{4.2}$$

In equation 4.2 the elements of the matrices $\mathbf{A_1}$ and $\mathbf{A_2}$ are the relative distances each seismic wave has traveled through each cell. $\mathbf{G}$ is the operator which smooths the horizontal and vertical gradient of the relative perturbation in S and SA and whose importance can be varied by adjusting the parameter η. The amount of apparent anisotropy SA can be minimized by adjusting the damping parameter μ which is multiplied by the identity matrix $\mathbf{I}$.

We illustrate the resolution of the inversion by a checkerboard synthetic test. The input model for the checkerboard test is an alternating pattern with 10%

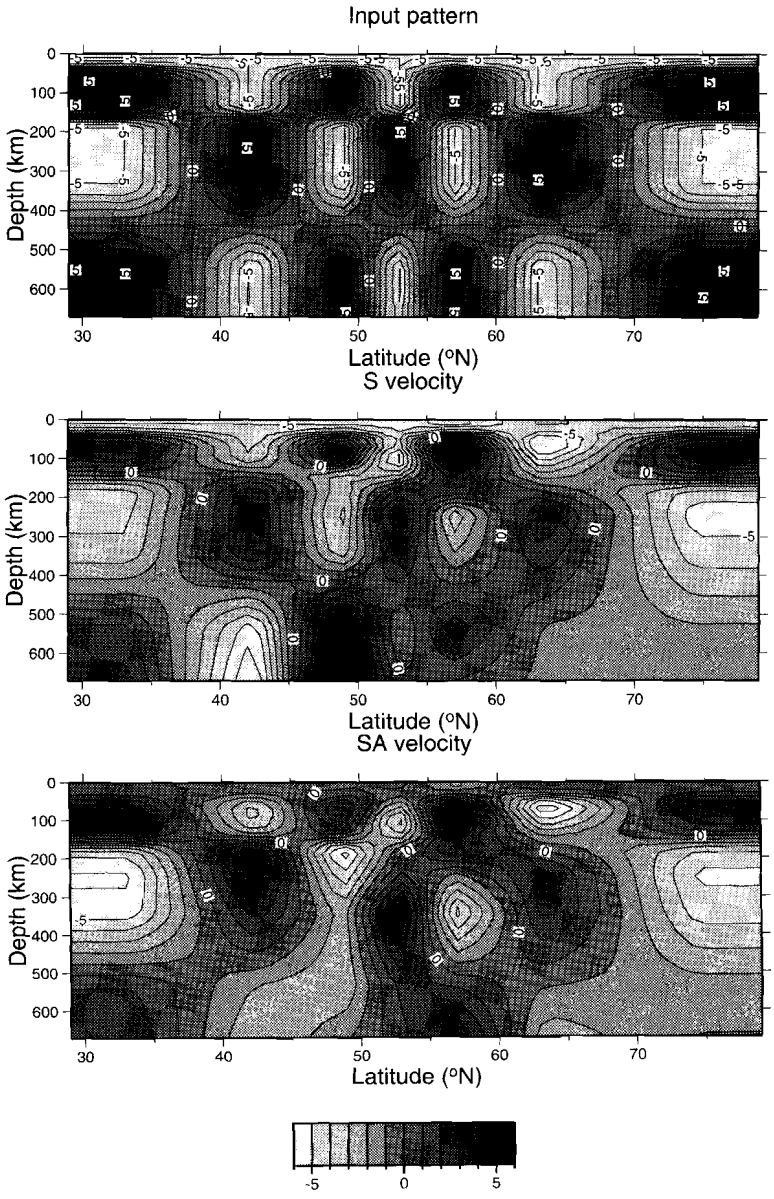

Figure 4.2: (a) Pattern of checkerboard synthetic test for the model presented in Figure 4.1. (b) Recovered S velocity model. Input model has perturbations of (0% – 10%) from which 5% has been subtracted for visual display. (c) Recovered SA velocity model. Input pattern has perturbation of $(-5\%, 5\%)$.

variation in S and SA, see Figure 4.2a. In Figure 4.2a the true amplitude of each cell has been plotted in the midpoint of each cell. Between the cell midpoints linear interpolation has been applied in order to obtain a smooth image. The perturbations in the SA model are -5% and 5%. The choice of the S perturbation is important as we compute the synthetic seismograms for the corresponding SH and SV models. When we define S similar to SA the perturbation in SV is zero throughout the model and the inversion of the Rayleigh waves becomes trivial. We have therefore shifted the pattern of the S perturbations to 0% and 10% which leads to a constant SV perturbation of 5%.

The synthetic seismograms computed for this input model have been inverted using the same inversion procedure as applied to the real data. The retrieved S and SA models are shown in Figure 4.2b-c where a constant value of 5% is subtracted from the S velocity for visual display. These Figures show that the S and SA velocities are equally well resolved. The resolution is good in the top and the center of the model. At depths larger than 400 km in the southern and the northern part the amplitude of S and SA is poorly recovered.

4.5 The Model

A prefered model has been selected on the basis of a trade-off analysis between model roughness and data-misfit, see Figure 4.3. We have tested a large number of combinations of the regularization parameters η and μ in the range 10-2000. The model roughness is defined as the sum of the gradient smoothing and the anisotropy damping. The data-misfit is the sum of the misfit between data and synthetics waveforms computed for the corresponding velocity model and is given by the first term on the right hand side in equation 4.1. The minimum norm model which is the point closest to the origin on the trade-off curve, is a logical but subjective choice which depends on the scaling of the axis, the relative importance of the smoothness of the model and the amount of anisotropy. After visual checks of the waveforms computed for the range of tested models we have selected a slightly rougher model which has stronger gradients in the variation of S but less apparent anisotropy SA than the minimum norm model. The prefered model is computed for $\eta = 250$ and $\mu = 500$ and is indicated by the star in Figure 4.3.

The prefered model for the S velocity and the apparent anisotropy SA is shown in Figure 4.1b-c. The S velocity model shows a clear signature of the European continent with 7% lateral variations in the lithosphere. At the southern boundary of the model, under the Eastern Mediterranean, we find low S velocities in the lithosphere. The mantle in this region is poorly resolved. Velocities increase under Turkey. The average velocity under Turkey and the Black Sea is described by a high velocity zone overlaying the asthenosphere which has a 5% lower S velocity. Velocities increases even further under the East European Platform, Ukrainian and Baltic shield where the thickness of the high velocity layer increases to a depth of 200 km. Under the East European Platform at a depth larger than 300 km low

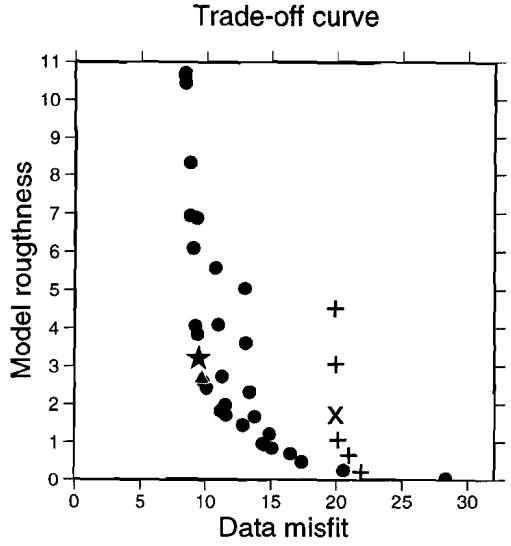

Figure 4.3: Trade-off curve for model roughness versus data misfit. Circles represent tested anisotropic models. The triangle indicates the minimum norm model. The preferred model is indicated by the star. Pluses indicate the isotropic models of which the preferred model is marked by the cross.

velocities are observed. In the Barentz sea region the thickness of the continent is approximately 100 km. The pattern of the apparent anisotropy SA is rather different. Under the Eastern Mediterranean high SA values (3.5%) are found in a well defined region at 100 km depth. Under the continent a broad region with increased SA values ($SA < 1.5\%$) can be identified. The shape of this structure does not correlate with the variations in the S model.

The waveform fits for the model are good. Figure 4.4a shows the waveform fits for the Rayleigh waves of the Egypt event. Both the fundamental modes and the S and SS phases have a good fits. Only the relative amplitude of these phases show a poorer fit. This is probably caused by ignoring variations in attenuation. A typical fit to the Love wave data is shown in Figure 4.4b where the Love wave of the Spitsbergen event are shown.

It is important to investigate whether apparent anisotropy SA is required in the model. We have therefore inverted the dataset only for S velocity and performed a trade-off analysis of which the results are indicated by the plus symbols (+) in Figure 4.3. The model roughness is in general smaller than for the anisotropic inversion because now the model roughness of SA is not included. The data-misfit of even the best fitting isotropic model is significantly worse than for the models with apparent anisotropy. The prefered isotropic S model is shown in Figure 4.5 and is remarkable similar to the model with SA included. This means that there is little trade-off between the S and SA velocity (compare Figures 4.1b and 4.5).

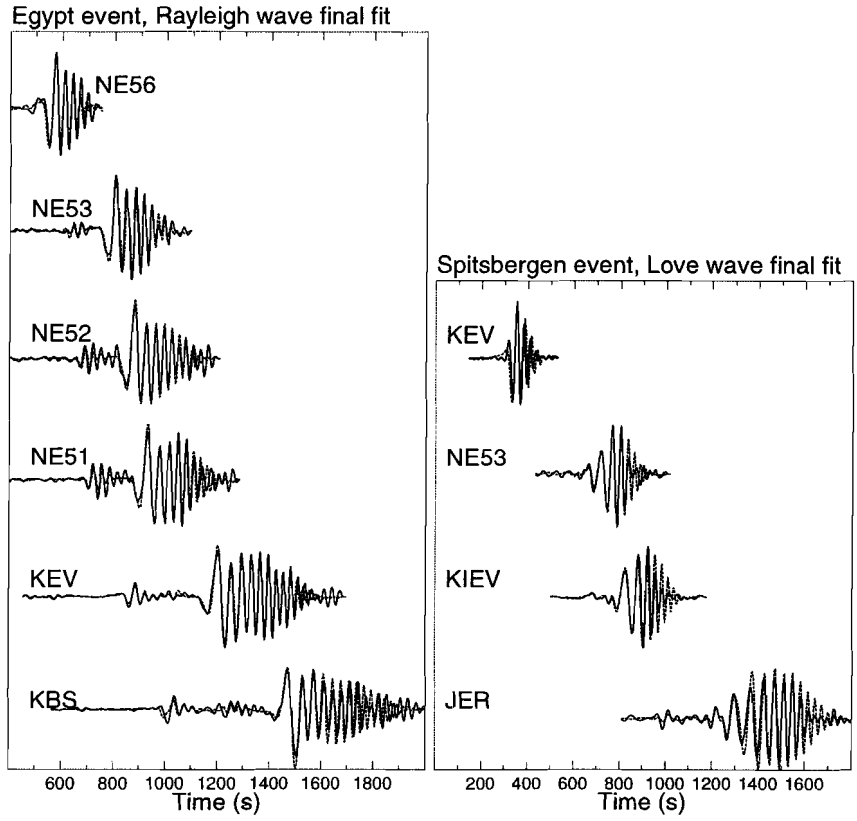

Figure 4.4: (a) Waveform fit of the Rayleigh waves from the Egypt event, filtered between periods $25s < T < 100s$. Solid line represents the data, the dashed line correspond to the synthetic seismograms. (b) Waveform fit for Love waves of the Spitsbergen event.

The presence of apparent anisotropy is clearly visible in the data. In Figure 4.6 we show data for the Spitsbergen event together with synthetics for the S velocity of the isotropic model displayed in Figure 4.5. Fundamental mode Love and Rayleigh waves recorded at station KIEV fit the data well which means that there is only little SA in the lithosphere between Spitsbergen and KIEV. Seismograms recorded 20° further south in JER however show a poor fit to the synthetics for the isotropic S model. Larger SH velocities and smaller SV velocities resulting in significant apparent anisotropy SA are required to explain the data. We have also observed this phenomena for seismograms of the Egypt and Turkey event. Thus we have a stable observation of apparent anisotropy SA.

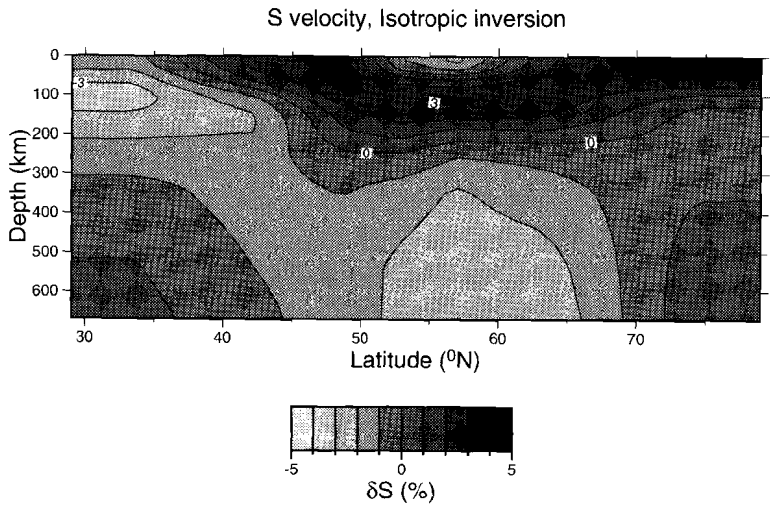

Figure 4.5: S velocity model obtained by the isotropic inversion.

4.6 The Eastern Mediterranean

The observed apparent anisotropy SA in the Eastern Mediterranean could be due to inexact modeling of the crustal structure. Levsin and Ratinkova (1984) have explained the 2% difference in SV and SH velocities between 20 – 220 km depth in the PREM model by lateral variations in Moho depth. For our model we have computed a crustal correction using the 5° × 5° crustal model CRUST5.1 (Mooney et al., 1996). This model shows that the crustal structure in the Eastern Mediterranean is very different from the continent with different Moho depth (26 km versus 40 km), thickness of the sedimentary layers and the presence of a water layer. The crustal correction in the Eastern Mediterranean for the short period fundamental Rayleigh wave ($T < 20$ s) is larger than 10% but at these periods it only samples the crust. The size of the crustal correction quickly decreases for increasing period as the surface wave penetrates deeper in the mantle. At a period of 40 s the crustal correction is only 2% and is not sufficient to explain the observed Love-Rayleigh discrepancy. Because of the magnitude of the Love-Rayleigh discrepancy (7%) our preferred interpretation of this anomaly is the presence of anisotropy in the lithosphere.

The interpretation of anisotropy in the Eastern Mediterranean is supported by tectonic reconstructions. Dercourt at al. (1986) propose the presence of an oceanic plate in the Eastern Mediterranean that has been subducted under Eurasia during the closure of the Tethys ocean. This hypothesis of oceanic lithosphere is based on tectonic reconstructions and the only direct evidence for it comes from seismic studies. On seismic profiles shot in the Ionian sea (20°E) oceanic crust has been identified (De Voogd et al., 1992). Along our profile at 30°E, however, both surface

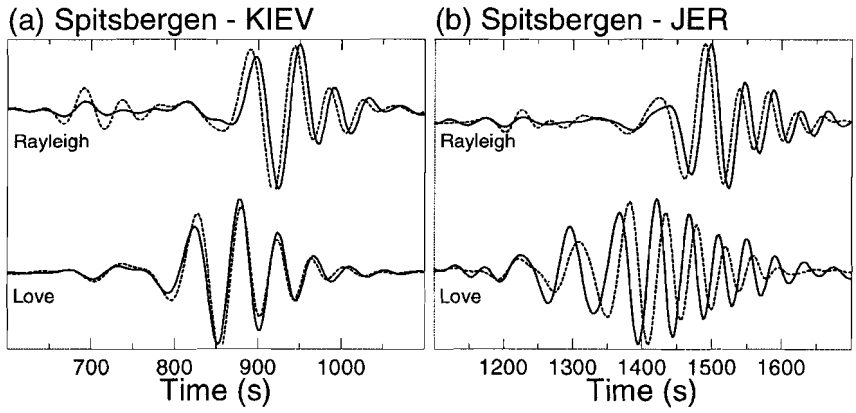

Figure 4.6: Waveform fit to the isotropic model for Love and Rayleigh waves for the Spitsbergen event recorded in KIEV. Synthetics (dashed line) have been computed for the isotropic S model shown in Figure 4.5. Seismograms are low pass filtered at $T = 50$ s. (b) Waveform fit for station JER.

wave and seismic reflection studies can not discriminate between oceanic crust and thinned continental crust, (Cloetingh, Nolet and Wortel, 1980; De Voogd et al., 1992). Our model for the lithosphere under Eastern Mediterranean is very similar to oceanic lithosphere which has 6% anisotropy down to 160 km and SV velocities between 120 km and 200 km of 4.3 km/s, see Nishimura and Forsyth (1989). As the high velocity lid remains shallow (depth $<$ 100 km) it indicates that the Eastern Mediterranean has an oceanic lithosphere likely to be younger than 100 Ma, which is in agreement with the reconstructions of Dercourt et al. (1986)

4.7 East European Continent

The geologic history of the East European Continent is very different from the Eastern Mediterranean. The southern part of the Eurasian continent consists of different tectonics blocks, such as the Anatolian block and the Black Sea region which were pressed onto the East European Platform (EEP) and Ukrainian Shield in the late Cretaceous (Dercourt et al., 1986). In our model, this recent tectonic activity is reflected in the velocity structure by a thin high velocity lid and little apparant anisotropy. A similar velocity structure is observed under the Barentz Sea microplate which collided 600 Ma ago with Baltic Shield and the Caledonides. The high velocity anomaly associated with the continent also extends to a depth of 100 km.

The East European Platform between stations NE53 and NE51 is of Proterozoic age. Between KIEV and NE53 it is overprinted by the Rhiphean aulacogen (1300 Ma) and the Dnieper-Donetz depression (340 Ma), see Zonenshain, Kuzmin

and Natapov (1990). Below the East European Platform we find a continuous high S velocity anomaly that extends down to a depth of 200 km. The seismic velocities under the Archean Baltic Shield (NE51-KEV) are slightly smaller than for the younger East European Platform but the anomaly extends to the same depth of 200km. At depths larger than 300 km, the EEP shows low S velocities. Similar low velocities have also been observed more westwards under the EEP by Nolet and Zielhuis (1994) who relate these to the injection of water by ancient subduction along the Tornquist-Teisseyre zone. We conclude that the geological boundary between the Proterozoic and Archean terrains and the surrounding tectonicly younger regions extends at least down to 200 km depth.

The crustal velocities correlate well with the image of the continent. They are not strongly affected by smoothing which can been seen by the low crustal velocity under the East European Platform. This anomaly can be interpreted as an image of the sedimentary layers which are present on the EEP but absent on the Baltic shield. There interpretation is however not correct as we have already corrected our data for such a crustal structure. We should therefore observe only very small velocity perturbations in the crust. When we omit the crustal correction we get poorer waveform fits and larger SA anomalies in the lithosphere. Therfore the most likely explanation for the crustal anomalies is that either the applied crustal model (CRUST5.1), or the computation of the crustal correction by summing the local phase velocities in each $5° \times 5°$ cell is not adequate.

There is no clear pattern in the apparent anisotropy SA under the continent. On average $SA < 1.5\%$ and in the Barentz Sea region SA is almost zero. As we already noted SA is affected by the crustal model and we expect that further improvement of the crustal model could reduce SA. On the other hand, other types of anisotropy are often observed under continents. For instance azimuthal dependence of phase velocities is observed under Central Europe studies by Yanovskaya et al. (1990). An other indication for continental anisotropy is SKS splitting which has been observed under several stations in the region (e.g ANTO in Turkey and OBN in Russia), see Silver (1996). It is interesting to note that one of the few seismic stations in the world where no splitting has been observed is KEV (Silver, 1996). This station is situated in our model on boundary of the cell that has the lowest SA value.

4.8 Seismic velocities and tectonic age

For oceanic plates several square-root of age and logarithmic relations between geophysical observables and the age of the ocean floor have been observed (Sclater et al. 1980). The square-root relation has been explained by a thermal model of a cooling half space and is valid for oceanic lithosphere younger than 80 Ma. In older oceanic lithosphere logarithmic relations have been observed, which were explained by a model of a cooling plate laying on a halfspace, see Sclater et al. (1980). Simular relations have been proposed for continental regions. Meissner

(1986) described an empirical logarithmic relation between the crustal thickness and the lithospheric age. For the Eurasian continent, Pavlenkova (1996) has shown that heat flow and P_n velocities decrease with lithospheric age. Because of the geodynamical implication of these relations we have investigated if such a relation exists in the lithosphere of continental regions.

The thickness of the continental lithosphere would be useful parameter for such an investigation. In our S velocity model it correlates well with the regional tectonics. Young lithosphere such as present in the Eastern Mediterranean is characterized by a very thin high velocity lid. The thickness of this lid increases to 100 km in continental regions such as the Black sea and Barentz sea. The high velocity layer has a thickness of 200 km under the East European Platform and Baltic. This high velocity layer reaches its largest depth extend under the Ukrainian shield and the southern part of the EEP. The definition of the base of the lithosphere however is somehow arbitrary as it depends on which contour level in the seismic model has been chosen.

We think that the average velocity of the lithosphere in our model is better resolved than the base of the lithosphere. We have computed the average S velocity perturbation between the Moho and 200 km depth. The crust is not included as already a crustal correction has been applied. The maximum depth of the integration is set to 200 km which seems to be the base of the lithosphere in our model. An uncertainty of 0.5% in the average velocity has been given to each value representing the uncertainty in the model and the integration depth. The tectonic age of each has been computed using ages given by Zonenshain et al., 1990. For several cells this has resulted in a significant uncertainty in the age as tectonic blocks with different ages are sampled (e.g. KIEV-NE53). As the data does not follow a linear trend, we have plotted the data on a logarithmic scale following the trend in the data, see Figure 4.7.

A least-squares fit to the data is computed for both a logarithmic and a square-root relation between seismic velocity and age. The quality of the fit is measured by χ^2 and should be around 1 for a good fit. The measurement for the Eastern Mediterranean, indicated by the triangle in Figure 4.7, has been excluded in the fit because we have concluded that this is not a continental region. The solid line in Figure 4.7 represents the fit for a logarithmic relation with $\chi^2 = 0.9$. The dashed, curved line in Figure 4.7 is the fit for a square-root of age relation of the seismic velocities and age. The fit with the data is slightly worse with $\chi^2 = 1.2$. When the measurement for the Eastern Mediterranean is included in the fitting procedure we get $\chi^2 = 0.9$ for the logarithmic relation and $\chi^2 = 2.2$ for the square-root relation. These numbers support the logarithmic relation between seismic velocities and lithospheric age. However because of the uncertainties in the Eastern Mediterranean and the small differences in χ^2 when this region is excluded we conclude that our model has a small favor for a logarithmic relation of seismic velocity and tectonic age.

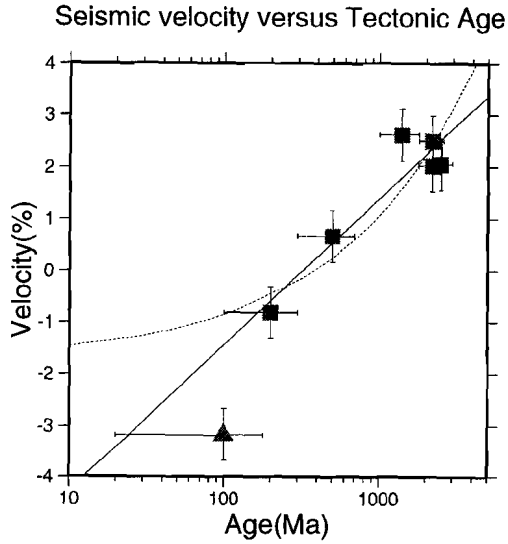

Figure 4.7: Seismic velocities versus tectonic age. The solid line represents a fit to the points indicated by the squares assuming a logarithmic relation. The dashed lines is computed for a square-root relation. The measurement for the Eastern Mediterranean indicated by the triangle has been excluded in the calculation.

4.9 Conclusion

Low shear velocities and strong apparent anisotropy are observed in the Eastern Mediterranean. The large difference of 7% in SH and SV velocities is interpreted as anisotropy. This interpretation is consistent with tectonic reconstructions of the region that predict the presence of oceanic lithosphere. The constructed model shows the European continent as a pronounced high velocity body extending down to 200 km depth under the proterozoic East European Platform and the archean Ukrainian and Baltic shields. In younger continental regions, such as the Black Sea and Barentz Sea the high velocity lid is thinner and extends only to a depth of 100 km. The seismic velocities in the continental lithosphere increase with tectonic age and slightly favor a logarithmic relation. However a possible square-root of age relation can not yet be excluded. In the continent only little the apparent seismic anisotropy is observed.

Chapter 5

Velocity and anisotropy of the Central Eurasian mantle

5.1 Abstract

The lithosphere and mantle structure along a source-receiver path under Central Eurasia is investigated by means of a Monte Carlo waveform inversion method. Fundamental and higher modes from a cluster of events with different source depth are jointly inverted for the path averaged velocity and anisotropy structure. Inversions for both the isotropic and transverse isotropic velocity structure have been carried out. The models show that the continental lithosphere beneath Eurasia has a constant S-velocity of $\beta = 4.6$ km/s and 2% S-wave anisotropy is observed. The mantle below 200 km depth is isotropic and not different from the PREM model. A resolution analysis shows that the model is well resolved down to 1000 km depth. In an inversion for anisotropy a 2% anomaly in the average of the horizontal and vertical P-velocities is observed in the lithosphere but we can not prove that this anomaly is statistically significant due to a limited resolution for this parameter and the small size of the anomaly.

5.2 Introduction

Seismic studies reveal the continental lithosphere as an anisotropic high velocity body overlying an isotropic mantle. In a recent study of the Australian continent Gaherty and Jordan (1995) observed $3.3 \pm 0.5\%$ shear-wave anisotropy. In other continents similar values have been observed. Regionalized surface wave data from Southern Germany can be explained by 4% shear wave anisotropy between 70 and 200 km depth (Friederich and Huang, 1996). The EU2 model of Gee and Jordan (1988) for the Eurasian lithosphere has 4% shear wave anisotropy down to 220 km and between 200 km and 400 km $1 - 2\%$ anisotropy is present. The amount

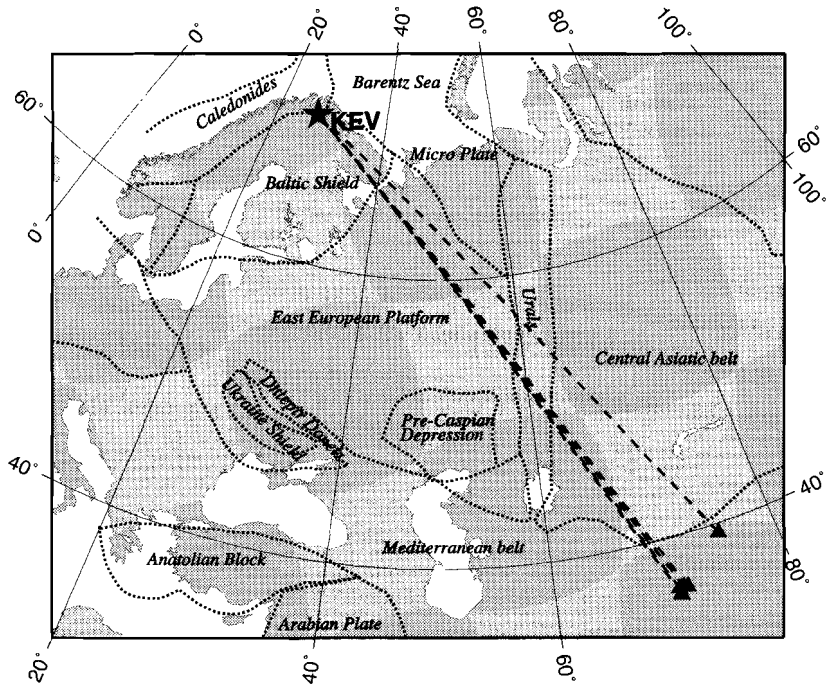

Figure 5.1: Map of Central Eurasia showing the location of the sources (triangles) and station (star). The tectonic regions are drawn after Zonenshain et al. (1990).

of anisotropy observed in the continental lithosphere is comparable to that in the global PREM model which has $2-4\%$ shear wave anisotropy in the lithosphere between 24.4 km and 220 km depth (Dziewonski and Anderson, 1981)

The change from an anisotropic lithosphere to an isotropic mantle has been explained in several ways. Originally it has been proposed that the Lehmann discontinuity marks the base of a zone of partial melt. Karato (1992) proposed that the Lehmann discontinuity results from a change in preferred orientation of olivine due to a change in deformation mechanism. Gaherty and Jordan (1995) interpreted the anisotropy in the lithosphere as a result of small scale heterogeneity and proposed that the Lehmann discontinuity represents a localized transition from an anisotropic boundary layer to an isotropic mantle. In all these studies anisotropy in the lithosphere has been introduced in order to explain the observed Love-Rayleigh discrepancy in the data. Another explanation for the observed Love-Rayleigh discrepancy is given by Levsin and Ratnikova (1984). They showed that lateral variations in the crustal structure can lead to a Love-Rayleigh discrepancy such as observed in the PREM model.

In this paper we investigate the one-dimensional shear velocity and anisotropy structure along a corridor from Afghanistan to the seismic station KEV (Fin-

Year, julian day	Component	Longitude (°)	Latitude (°)	depth (km)
1990.107	TZ	75.03	39.38	15
1991.031	TZ	70.45	35.99	140
1990.194	TZ	70.79	36.45	203
1990.135	Z	70.44	36.03	216
1991.195	TZ	71.11	36.42	219
1993.204	T	70.41	36.44	272

Table 5.1: Events used in this study

land), see Figure 5.1. The seismic waves travel entirely through continental lithosphere and sample the Proterozoic East European Platform and the Archean Baltic Shield, the Urals and the Central Asiatic Belt. We invert fundamental and higher mode Love and Rayleigh waves for isotropy and anisotropy. For the anisotropic inversion we use the parameterization for transverse isotropy described in chapter 3 and invert the Love waves for β_H and the Rayleigh waves for β_V, the average of horizontal and vertical P-velocity α_+, and the difference in the horizontal and vertical P-velocity α_-. We explicitly correct for the crustal structure with the CRUST5.1 model (Mooney, Laske and Masters, 1996) in order to reduce a possible Love-Rayleigh discrepancy.

The seismograms are inverted from the fundamental mode up to the direct S-wave, including the higher modes. Due to interference of the higher modes it is difficult to identify the individual dispersion curves. Stutzmann and Montagner (1993) therefore determined the higher mode dispersion curves from data of a cluster of events located close to each other and recorded by a single station. They improved the depth resolution by selecting events with different source depths as the excitation of the higher modes is depth dependent. We follow a similar approach as we will jointly invert seismograms from the same source region but with different source depths. However we do not determine the dispersion curves but invert the waveform directly for the path averaged velocity structure similar to method of partitioned waveform inversion of Nolet (1990).

A Monte Carlo waveform inversion is carried out which allows us to explore the model space and estimate the resolution. Randomly chosen models are tested against the data and a set of models that successfully fit the data is obtained. On this ensemble of models a resolution analysis is carried out (Kennett and Nolet, 1978; Douma, Lomax and Snieder, 1996). This resolution analysis has similarities to the Backus-Gilbert approach for linear systems and allows us to investigatewhich features can be resolved in the inversion. We show that the model is well-resolved down to 1000 km depth. We also show that the joint inversion of higher modes has a better resolution than the inversion of each event separately. Finally we investigate possible trade-offs between the parameters when anisotropy is included in the inversion.

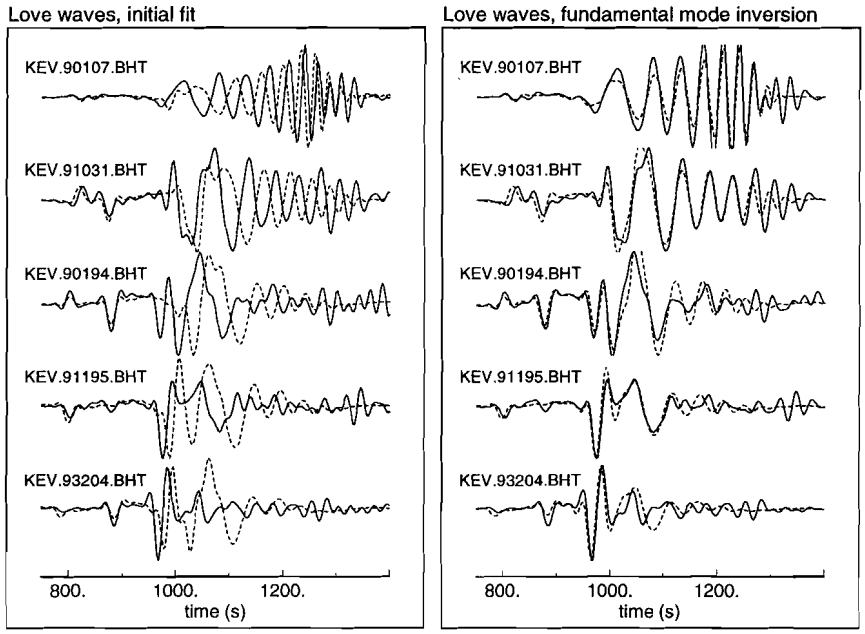

Figure 5.2: (a) Initial waveform fit for Love wave data. The seismograms are sorted with increasing source depth. Solid line represents the data bandpass filtered between $20 < T < 200s$, the dashed line the synthetic seismogram computed for the starting model. (b) Waveform fit to fundamental mode model displayed in Figure 5.3a.

5.3 Data

The events are selected from a small region in the Hindu Kush region where both shallow and deep seismicity occurs due to the collision of the Indian plate with Eurasia. The seismic waves recorded in KEV travel through the Central Asiatic Belt, the Urals, the East European Platform and the Baltic Shield, see Figure 5.1. All selected events have a magnitude $M_w > 5.5$ and have a good signal to noise ratio in the frequency band ($20 < T < 200s$) used in this study. The seismograms have been checked on sensitivity of the initial phase of the wave to small variations in the source parameters (Muyzert and Snieder, 1996). In total five transverse and five vertical component seismograms have been used, see Table 5.1.

The starting model for the inversion has a constant S-velocity of 4.5 km/s in the lithosphere and a moho depth of 50 km. On each seismogram a crustal correction has been applied for the CRUST5.1 model (Mooney, Laske and Master, 1996). Below 220 km the starting model is identical to PREM (Dziewonksi and Anderson, 1981). Figure 5.2a shows the Love wave data set together with synthetic seismograms computed for the starting model of the inversion. The waveform fits for the fundamental mode in particular are rather poor and indicate a faster

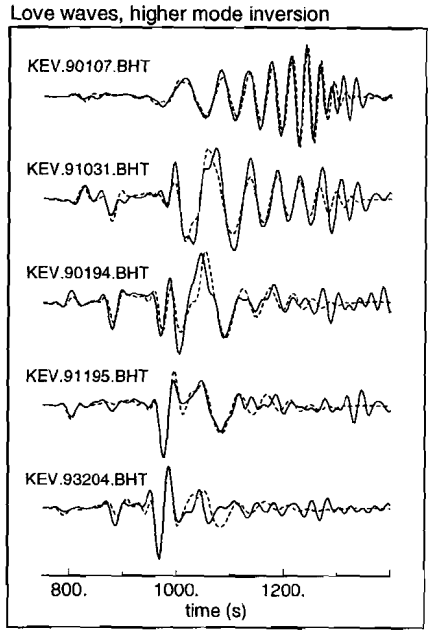

Figure 5.2 continued (c)Waveform fit to the higher mode model displayed in Figure 5.3b

lithosphere. The fits for the S-wave are much better but also indicate that the starting model is to slow.

5.4 Waveforms and anisotropy

The seismograms are computed by the summation of surface wave modes (Aki and Richards, 1980) :

$$u(\omega, \mathbf{m}) = \sum_{n=1}^{N} A_n(\omega) \exp\left[i\Delta\left(k_n^0 + \delta k_n(\omega, \mathbf{m})\right)\right] \tag{5.1}$$

This equation describes the spectrum of the wave field $u(\omega, \mathbf{m})$ recorded at epicentral distance Δ for a given model $\mathbf{m}$ at frequency ω. $A_n(\omega)$ is an amplitude term including attenuation and the initial phase and amplitude of the source. Heterogeneity is taken into account by the averaged horizontal wavenumber $\delta k_n(\omega)$. The wavenumber k is related to the phase velocity c by :

$$\delta k/k = -\delta c/c \tag{5.2}$$

Perturbations in the model can now be computed using the partial derivatives of the phase velocity.

In chapter 3 we have shown by the analysis of the partial derivatives that Love waves in a transverse isotropic medium are sensitive to β_H velocity and the Rayleigh waves to three parameters, β_V, $\alpha_+ = \frac{1}{2}(\alpha_H + \alpha_V)$ and $\alpha_- = \frac{1}{2}(\alpha_H - \alpha_V)$. These conclusions are valid in the period range $20s < T < 200s$. This parameterization will be used in the inversion. For Love waves the perturbation in the phase velocity due to variations in β_H is given by :

$$\left(\frac{\delta c}{c}\right) = \int_{z=0}^{R} \frac{\beta_H}{c}\left[\frac{\partial c}{\partial \beta_H}\right]\frac{\delta \beta_H}{\beta_H} dz \tag{5.3}$$

For the isotropic inversion of Rayleigh waves a similar expression for β_V is used. For transverse isotropic inversion of Rayleigh waves the following expression is used that relates the perturbations in the phase velocity due to variations in the β_V, α_+ and α_-

$$\left(\frac{\delta c}{c}\right) = \int_{z=0}^{R} \frac{\beta_V}{c}\left[\frac{\partial c}{\partial \beta_V}\right]\frac{\delta \beta_V}{\beta_V} dz + \int_{z=0}^{R} \frac{\alpha_+}{c}\left[\frac{\partial c}{\partial \alpha_+}\right]\frac{\delta \alpha_+}{\alpha_+} dz + \int_{z=0}^{R} \frac{\alpha_-}{c}\left[\frac{\partial c}{\partial \alpha_-}\right]\frac{\delta \alpha_-}{\alpha_-} dz \tag{5.4}$$

Different partial derivative for $\left[\frac{\partial c}{\partial \beta_V}\right]$ are used in the isotropic and transverse isotropic inversions, see chapter 3.

The seismograms are filtered in frequency and phase velocity windows. By this procedure parts of the seismogram are isolated and can be given different weight in the inversion. This is a similar aproach as used in the partitioned waveform inversion of Nolet 1990. We have defined 4 windows; around the S-phase, the SS-phase and two fundamental mode windows, see Table 5.2. Each data window $D(t)$ contains the filtered seismogram and is normalized using the L^2 norm :

$$\tilde{D}(t) = \frac{D(t)}{\sqrt{\int_{t=T_1}^{T_2} D^2(t) dt}} \tag{5.5}$$

The total misfit is defined as the sum over the misfits of all I data windows of J events :

$$\xi^2 = \sum_{i=1}^{I}\sum_{j=1}^{J} A_{ij} \int_{t=T_1}^{T_2} \left[\tilde{D}_{ij}(t) - \tilde{S}_{ij}(t, \mathbf{m})\right]^2 dt \tag{5.6}$$

with A_{ij} are the weights of the diferent events and data windows.

	Love wave		Rayleigh wave	
Data type	Period (s)	V_g (km/s)	Period (s)	V_g (km/s)
Short Period Fund. mode	30 - 75	3.1 - 4.2	30 - 75	3.4 - 4.1
Long Period Fund. mode	75 - 200	3.5 - 5.9	75 - 200	3.0 - 5.5
Higher modes and SS-phase	20 - 70	4.2 - 5.0	20 - 70	4.1 - 4.8
Higher modes and S-phase	20 - 70	5.0 - 6.0	20 - 70	4.8 - 6.0

Table 5.2: Definition of data windows for Love and Rayleigh waves

5.5 Resolution analysis

Using the Monte Carlo method we generate a set of models and compute the misfit with the data. A model is a vector $\mathbf{m}$ with length N, $\mathbf{m} = (m_1, m_2 \cdot \cdot, m_N)$. The resolution analysis is carried out on the set of models that successfully fit the data. We define a successful model as a model with a misfit less than ϵ different from the smallest misfit ξ^2_{min} found in the Monte Carlo search.

$$\frac{\xi^2}{W} < \frac{\xi^2_{min}}{W} + \epsilon \tag{5.7}$$

In this criterion we average the misfit over the number of data windows $W = I \cdot J$. The maximum allowed difference of a successful misfit with respect to the minimum misfit is ϵ. In the next section we describe the inversion of the higher mode Love wave data set. For that particular inversion we have tested 300.000 Monte Carlo models and found a minimum misfit of $\xi^2_{min}/W = 0.66$, a maximum misfit of $\xi^2_{max}/W = 3.15$ and an average misfit for all tested models of $\bar{\xi}^2/W = 2.03$. As a model with an average misfit gives a poor fit to the data ϵ must be much smaller than $\bar{\xi}^2/W - \xi^2_{min}/W = 1.37$. Based on visual comparisons of the waveforms we found that models with $\epsilon = 0.2$ gave waveform fits are comparable to the minimum misfit model. The value for $\epsilon = 0.2$ is not too small as an increase to $\epsilon = 0.4$ did not give significantly different results for the resolution analysis. The set of successful models depends also on the weight of the data windows. Throughout this study we have use equal weights of the data windows, see equation 5.6. We have also experimented with different weights for the each data windows. This leads to significant different results only when the weights are very different from each other (e.g. the weights for the higher mode windows are zero). We have tested Monte Carlo models until we found approximately $10 \times N$ (with N the number of parameters) successful models.

We apply on the set of successful models the resolution analysis of Kennett and Nolet (1978). A similar approach has been described by Douma et al. (1996). The resolution analysis requires that the model space is over-parameterized in such a way that the successful models expose a "raggedness". First we find the average model $\bar{\mathbf{m}}$:

$$\bar{\mathbf{m}} = \frac{1}{L} \sum_{l=1}^{L} \mathbf{m}_l \tag{5.8}$$

where L is the number of successful models. The average is subtracted from all successful models, giving the deviations $\mathbf{p}_l$:

$$\mathbf{p}_l = \mathbf{m}_l - \bar{\mathbf{m}} \tag{5.9}$$

We can project $\mathbf{p}_l$ on N orthonormal base vectors $\mathbf{v}_n$:

$$\mathbf{p}_l = \sum_{n=1}^{N} \alpha_{nl} \mathbf{v}_n \tag{5.10}$$

The vectors $\mathbf{v}_n$ are chosen such that they independently constrain the data. Then $\mathbf{v}_n$ are the eigenvectors of the covariance matrix $\hat{\mathbf{P}}$.

$$\hat{\mathbf{P}} = \frac{1}{L}\sum_{l=1}^{L} \mathbf{p}_l \mathbf{p}_l^T \tag{5.11}$$

The eigenvalues λ_n are the variances for the eigenvectors $\mathbf{v}_n$. Thus the eigenvector with the smallest eigenvalue is the best determined part of the model space. We therefore sort the eigenvectors $\mathbf{v}_n$ with increasing eigenvalues λ_n.

The resolution matrix $\hat{\mathbf{R}}$ is defined as :

$$\hat{\mathbf{R}} = \sum_{n=1}^{Q} \mathbf{v}_n \mathbf{v}_n^T \tag{5.12}$$

where Q is the maximum number of eigenvectors used. Several definitions for this truncation level have been used. Douma et al. (1996) determine Q from the eigenvalue spectrum and take only the eigenvalues before the largest jump in the eigenvalue spectrum. This truncated expansion in eigenvectors, equation 5.12 contains the robust information about the solution. It is however difficult to determine the largest jump in the eigenvalue spectrum as often the eigenvector spectrum changes smoothly. Another criterion for the eigenvalue truncation is given by Kennett and Nolet (1978). They relate the truncation level to the maximum allowed variance M_i in the parameter p_i.

$$var(p_i) = \sum_{n=1}^{Q} v_{in} v_{in} \lambda_n < M_i \tag{5.13}$$

Note that in their paper $var(\alpha_i)$ is written instead of $var(p_i)$. According to Kennett and Nolet (1978) "*This truncation thus arises from the constraints imposed during the model generation*". The problem with this criterion is that for an over-parameterized model space the variance in each parameter is similar to the variance imposed during the model generation. This means that all eigenvectors are taken into account to estimate the resolution.

We interpret equation 5.13 in a slightly different way. Similar to the Backus-Gilbert approach for linear inversion we define a preferred variance for each parameter which is used as the maximum allowed variance M_i (Backus and Gilbert, 1968). With equation 5.13 we can compute the truncation level Q_i for which the error in the model parameter is less than the prescribed uncertainty M_i. For this truncation level we then determine the resolution for each parameter. As the best determined eigenvectors are typically only sensitive to a limited part of the model space the number of eigenvectors used to estimate the truncation level varies from parameter to parameter. Therefore the truncation level Q_i is parameter dependent. When a small uncertainty is required only a few eigenvectors will be taken into account resulting in a poor resolution. The resolution can be improved by

taking more eigenvectors into account but as a drawback this leads to a larger uncertainty in the estimated model parameters. This trade-off between uncertainty and resolution is now an analogy of the resolution analysis for linear systems as developed by Backus and Gilbert (1968).

Similar to the approach followed by Douma et al. (1996) we project the successful models on the set of truncated eigenvectors :

$$m_{il} = \bar{m}_i + \sum_{n=1}^{Q_i} \alpha_{nl} v_{in} \tag{5.14}$$

The scatter in this "filtered ensemble" will be the maximum allowed variance M_i.

5.6 Inversion : Love waves

In this section we discuss in detail the application of the Monte Carlo inversion and the resolution analysis of the Love wave dataset recorded in station KEV. First we illustrate the resolution of the inversion by a comparison of models that fit only the fundamental mode data with models that fit both fundamental and higher mode data. The model is parameterized by 12 layers which are given in Table 5.3. The search boundaries for the velocity model are ±8% around the starting model. We have evaluated 300.000 Monte Carlo models. We found 160 models that successfully fit both the fundamental mode data and the higher mode data by passing the misfit criterion given by equation 5.7. These successful models are shown by the gray lines in Figure 5.3b. We have also selected 160 models that only fit the fundamental mode data without constraints on the higher mode data, see

Index Layer	**Isotropy** depth (km)	**Anisotropy** depth (km)
1	0 - 50	0 - 100
2	50 - 100	100 - 220
3	100 - 150	220 - 400
4	150 - 220	400 - 670
5	220 - 300	670 - 2071
6	300 - 400	
7	400 - 520	
8	520 - 670	
9	670 - 821	
10	821 - 971	
11	971 - 1371	
12	1371 - 2071	

Table 5.3: Depth parameterization for inversion

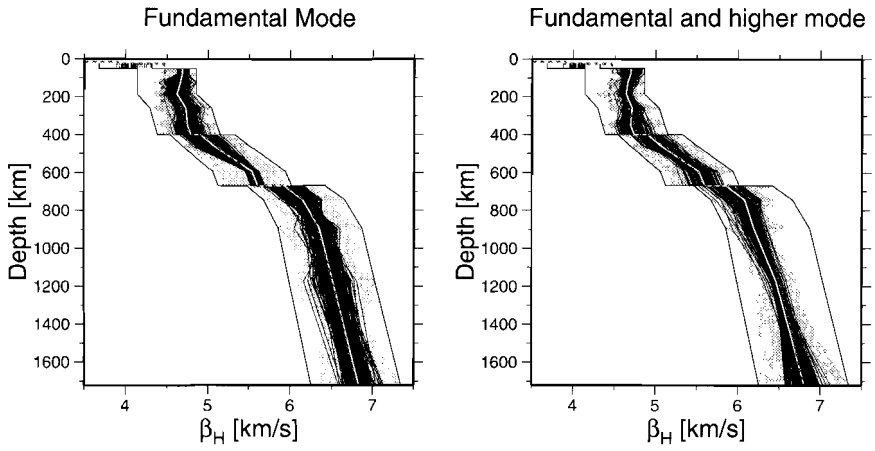

Figure 5.3: (a) β_H velocity model obtained by the Monte Carlo inversion of fundamental mode Love wave data. The gray lines are 160 successful models. Black lines are the filtered models with parameter uncertainty $M_i = 2\%$. The white line is the average model. The dark dashed line is the PREM model. (b) β_H velocity model obtained by inversion of fundamental and higher mode Love wave data.

Figure 5.3a. In this case the misfit is computed by summation of the fundamental mode windows only.

Two different observations indicate that the ensembles are not purely random models but that they contain information about the model parameters. First, in the lithosphere the scatter in the unfiltered ensembles does not reach the lower search boundary. This implies that the data can not be fitted with low velocities in the lithosphere. In the mantle below the lithosphere however many successful models reach the $\pm 8\%$ search bounds. Second, the models in both ensembles are oscillatory which can be seen from their raggedness. The parameters of an oscillatory model are anti-correlated for neighboring layers which is a result of the over-parameterized model space. The fundamental mode ensemble is oscilatory down to 670 km depth. Below 670 km the model parameters are not correlated, i.e. the models are not oscilatory. This indicates that the fundamental mode ensemble has little information about the lower mantle. The higher mode ensemble in this depth range is still oscillatory (compare the raggedness of gray models in the lower mantle in Figures 5.3a-b).

For both ensembles we have computed the average model (indicated by the white line in Figure 5.3) and the filtered ensemble for a parameter uncertainty $M_i = 2\%$. The filtered ensembles look very similar to each other but have a very different depth resolution. The lithosphere has a significant higher β_H velocity in comparison to the PREM model (4.7 km/s versus 4.5 km/s). Below 220 km depth β_H is very similar to PREM, except for the higher mode ensemble which shows 1.5% lower β_H between 670 km and 1100 km depth.

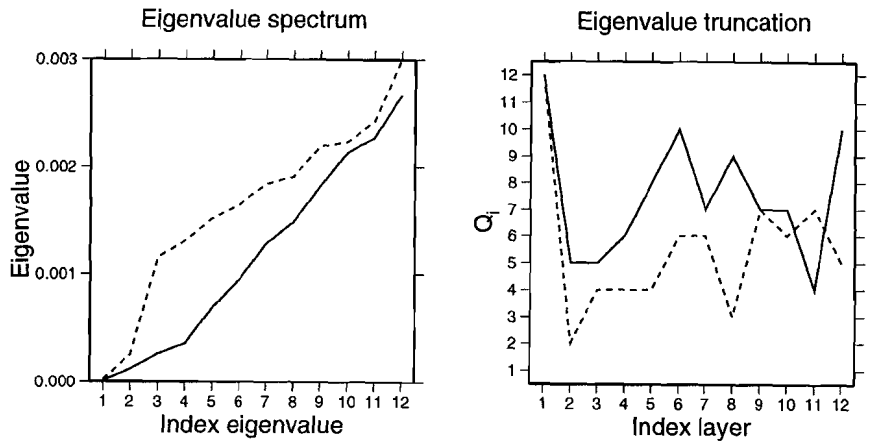

Figure 5.4: (a) Eigenvalue spectrum for fundamental mode inversion (dashed line) and higher mode inversion (solid line). (b) Eigenvalue truncation of each layer for parameter uncertainty $M_i = 2\%$. Line styles as in (a).

The eigenvalue spectrum for both ensembles are shown in Figure 5.4a. The fundamental mode ensemble has a clear jump between the second and third eigenvalue. According to the truncation criterion of Douma et al. (1996) the robust elements of the model space would be described by only two eigenvectors. The eigenvalue spectrum of the higher mode ensemble is much more smooth and a small jump can be found between eigenvalue 4 and 5. This means that the higher mode ensemble is better constrained as it has more small eigenvalues.

The corresponding eigenvectors are show in Figure 5.5. The best determined eigenvector (V_1) of both ensembles are almost identical and is only sensitive to the crust. The second eigenvector (V_2) for both ensembles are also similar to each other. The other eigenvectors are different to each other due to the influence of the higher mode data, although some eigenvectors are surprisingly similar (e.g. V_7, V_8).

In Figure 5.4b the eigenvalue truncation Q_i of each layer for parameter uncertainty $M_i = 2\%$ is shown. The shallowest layer is perfectly resolved in both inversions as Q_i is equal to the maximum number of eigenvectors. In the other layers the maximum allowed error is reached using between 2 and 10 eigenvectors. In the higher mode ensemble Q_i is larger than for the fundamental mode ensemble which indicates a better constrained solution.

The resolution kernels computed for a parameter uncertainty of $M_i = 2\%$ are shown in Figure 5.6. When the model is described by a continious function the resolution kernel for a perfectly resolved parameter is a deltafunction. In this paper a discrete parameterization is used in terms of a finite set of layers. A layer is perfectly resolved when the resolution is only non-zero within that layer, this is decribed by the dotted lines in Figure 5.6.

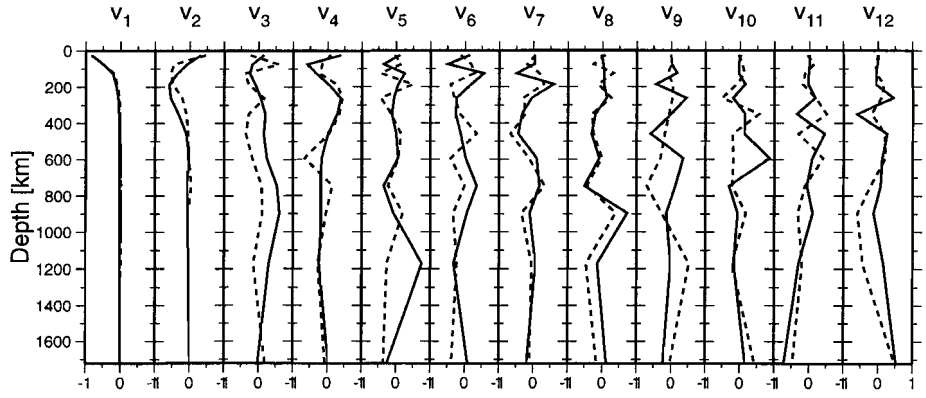

Figure 5.5: Eigenvectors sorted with increasing eigenvalue used for the resolution analysis for Figure 5.3. Dashed line are the eigenvalues found for fundamental mode data alone. Solid line are obtained when both fundamental and higher mode data is used.

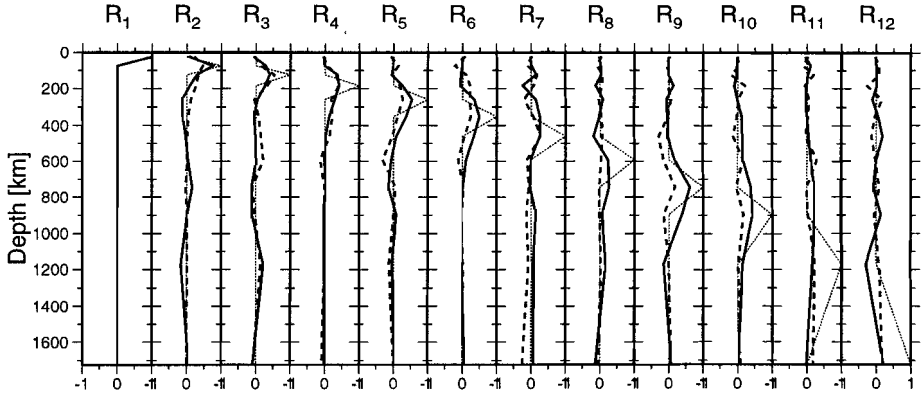

Figure 5.6: Resolution analysis for Figure 5.3. Dashed line are the resolution kernels found for fundamental mode data alone. Solid line are obtained when both fundamental and higher mode data is used. The dotted line is the ideal resolution kernel.

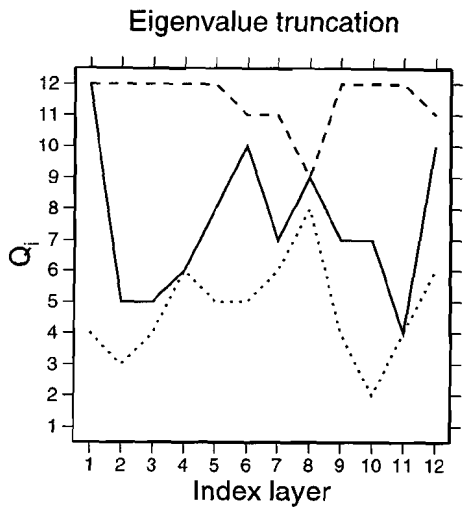

Figure 5.7: Eigenvalue truncation for higher mode inversion for parameter uncertainty $M_i = 1\%$ (dotted line), $M_i = 2\%$ (solid line) and $M_i = 4\%$ (dashed line).

The best resolution is achieved when all eigenvectors are used to construct the resolution kernel, see Douma, Lomax and Snieder (1996). This is observed in the shallowest layer of both ensembles. In the deeper layers the resolution is not so perfect. In the lithosphere the resolution for both ensembles is very similar and approximately 100 km thick layers can be resolved. In the mantle below the lithosphere the resolution the ensembles different. The fundamental mode ensemble has a poor resolution between 200 km and 400 km depth and at larger depths the resolution kernel is zero which means that the model is not resolved at these depths. The higher mode ensemble resolves a layer of 400 km thickness in the mantle. Below 1000 km depth the higher mode model is not resolved.

The waveform fits for the average models of both ensembles are very good, see Figure 5.2b-c. For the fundamental mode model, the direct S-wave is the only poorly fitted part of the seismograms (see Figure 5.2b near $t = 800s$). This is not surprising as we have not inverted this part of the waveform. The seismograms for the model derived using the higher mode data also fit the direct S-wave well, see Figure 5.2c.

The imposed parameter uncertainty M_i has a large influence on the truncation value Q_i. Figure 5.7 shows the eigenvalue truncation calculated for the parameter uncertainties $M_i = 1\%$, $M_i = 2\%$ and $M_i = 4\%$. The Figure illustrates clearly that for a small parameter uncertainty only the first few eigenvalues are used ($2 < Q_i < 8$). The corresponding resolution kernels are shown in Figure 5.8. The resolution kernels in the lithosphere for $M_i = 1\%$ are not different for $M_i = 2\%$. However below 200 km depth the resolution for $M_i = 1\%$ is poorer as the width of the resolution kernel increase and the peak amplitude decreases. A large imposed

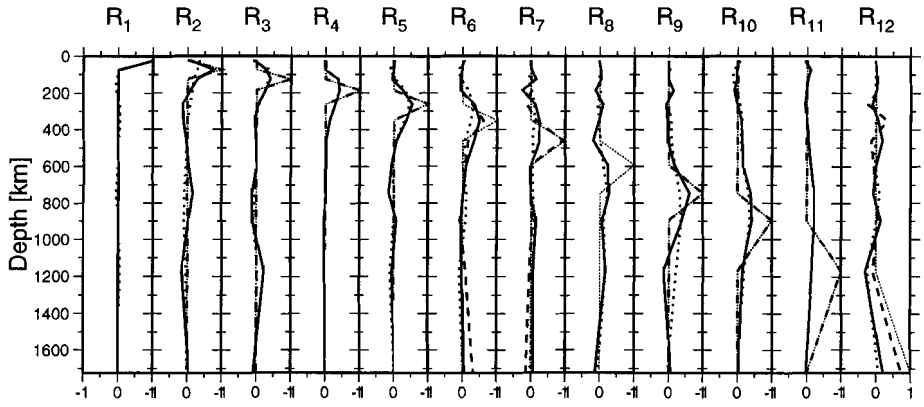

Figure 5.8: Resolution analysis for higher mode inversion for parameter uncertainties $M_i = 1\%$ (dotted line), $M_i = 2\%$ (solid line) and $M_i = 4\%$ (dashed line). The thin dotted line represents the ideal resolution kernel.

larger parameter uncertainty ($M_i = 4\%$) results in perfect resolution in most layers as the maximum number (12) of eigenvalues is used for the construction of the resolution kernels. Further on we will use $M_i = 2\%$ by which we still have some resolution the lower mantle resolution without losing to much uncertainty.

We now ask the question if the simultaneous inversion of more events improves the resolution. We have therefore selected for each event an ensemble of 160 successful models and applied the resolution analysis to the ensembles. The average models for the single event inversions are shown in Figure 5.9. Particular around 400 km depth these average models show significantly differences which is likely due to noise in the individual seismograms. The resolution of the single event inversions is worse than the simultaneous inversion, see Figure 5.10. For instance the single event resolution kernels for the fourth and fifth layer, R_4, R_5, shows that the resolution strongly varies between the events. The shallowest event, *kev.*90107.*bht* has the poorest resolution.

A better comparison of the fundamental and the higher mode inversions can be made when we average the five single event average models. This average model is close to the model obtained by the joint higher mode inversion previously described. We have also averaged the resolution kernels for the five single event inversions. The averaged resolution kernels are in the upper mantle similar to the resolution kernel for the joint inversion. However in the lower mantle the joint inversion has a significantly better resolution, see R_9, R_{10} and R_{11}. The reason of the better resolution in the lower mantle is that the successful models of the joint inversion fit all seismograms well. This is not the case in the single event inversions where each ensemble only fits a single seismogram and the higher modes are less well constrained. For this reason Stutzmann and Montagner (1993) developed their higher mode dispersion measurement technique.

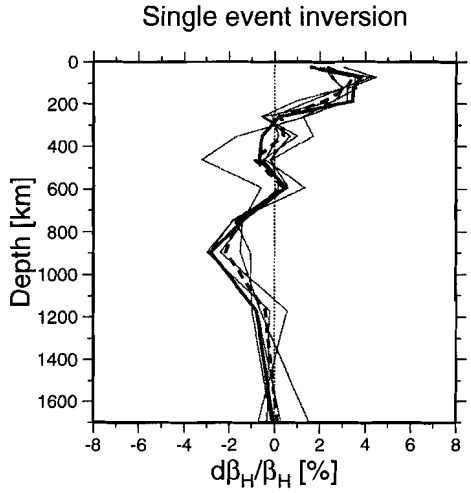

Figure 5.9: Single event inversion for parameter uncertainty $M_i = 2\%$. The thin lines represent the average model obtained by single event inversion. The thick dashed line is the average of all single event models. The solid line represents the average model obtained by simultaneous inversion of all events.

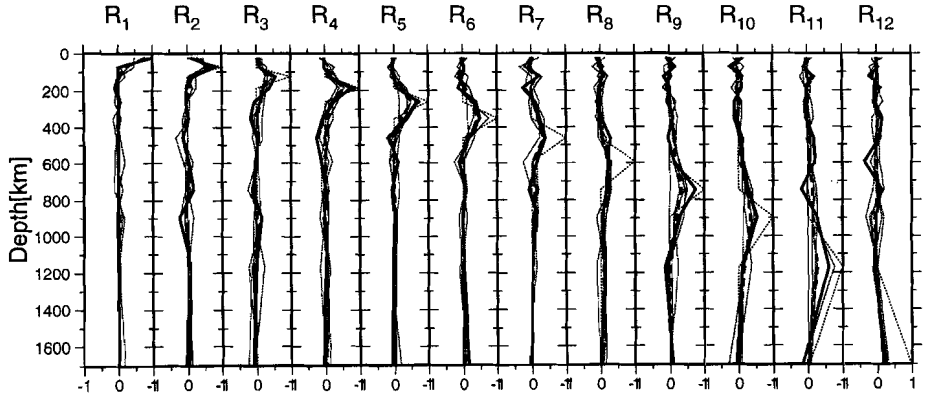

Figure 5.10: Resolution analysis for the the single event inversion. Line styles as in Figure 5.9

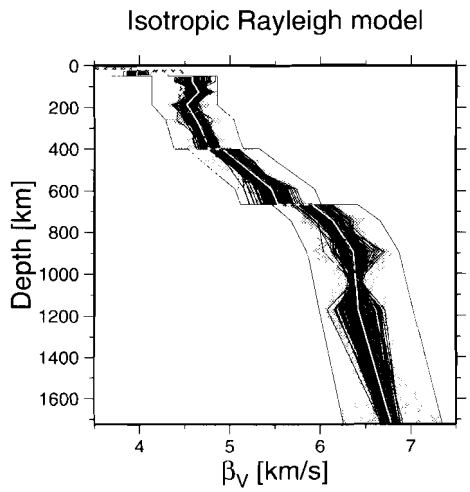

Figure 5.11: β_V velocity model obtained by the isotropic Monte Carlo inversion of Rayleigh data. The gray lines are 151 successful models. The black lines are the filtered models with parameter uncertainty $M_i = 2\%$. The white line is the average model. The dark dashed line is the PREM model.

5.7 Inversion : Rayleigh waves, isotropy

The same analysis is carried out on vertical component Rayleigh waves of the same source-receiver path. In this run the data has been inverted for β_V velocity assuming isotropy. The layer parameterization is identical to the previous analysis of the Love wave. The ensemble of successful models consist of 151 models that passed the misfit criterion. The raw and filtered ensembles for $M_i = 2\%$ and the average model are shown in Figure 5.11. In the lithosphere $\beta_V = 4.6$ km/s which is higher than in the PREM model but still lower than in the previously described β_H model. Below the lithosphere the difference with PREM is less than 1%.

The eigenvalue spectrum has a jump between eigenvalues λ_5 and λ_6 indicating that the first 5 eigenvectors are the best constrained parts of the model, see figure 5.12. The eigenvalue truncation for a parameter uncertainty $M_i = 2\%$ is flat compared to that of the Love waves. The best determined eigenvector V_1 is only sensitive in the upper part of the lithosphere, see Figure 5.13. Eigenvectors V_2 to V_5 have an increasing depth penetration and number of zero crossings. This together with the flat eigenvalue truncation indicates that the Rayleigh wave ensemble is better constrained than the Love wave ensemble. The corresponding resolution kernels show that the model is well resolved down to 1000 km depth, see Figure 5.14. Note that the resolution in the transition zone is significantly better than for the Love waves. This difference in resolution might be caused by an increased noise level on the horizontal components. The waveform fits for the averaged model of this isotropic inversion of the Rayleigh waves are good, see Figure 5.15.

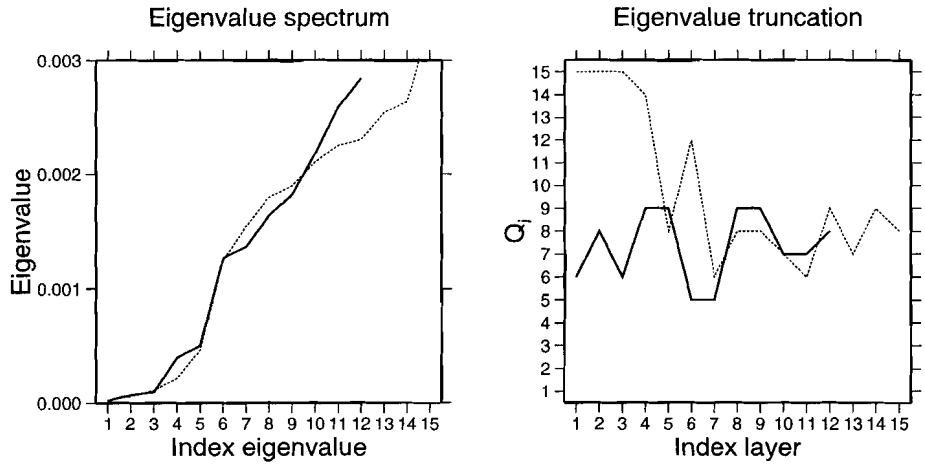

Figure 5.12: (a) Eigenvalue spectrum for inversion of Rayleigh wave. The solid line represents the isotropic inversion. The dashed line the anisotropic inversion. (b) Eigenvalue truncation for the Rayleigh wave inversion.

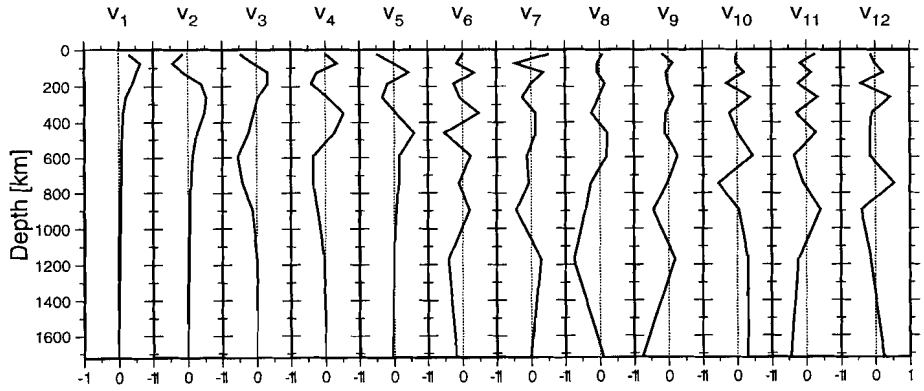

Figure 5.13: Eigenvectors sorted with increasing eigenvalue for the isotropic Rayleigh wave inversion.

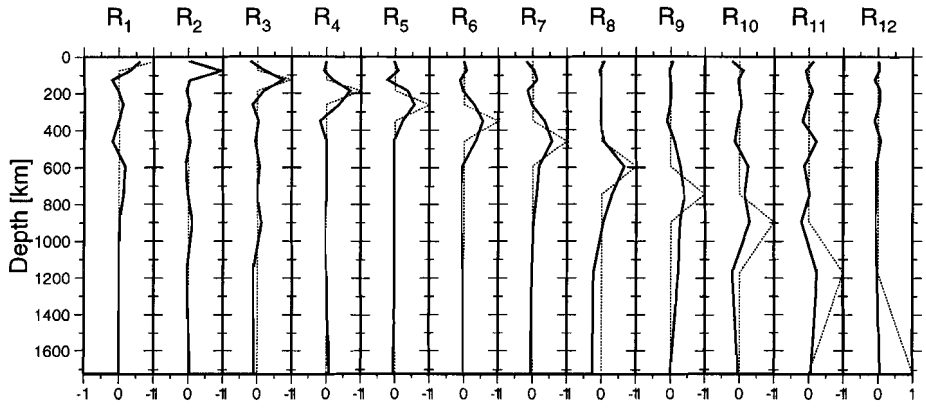

Figure 5.14: Resolution analysis for Figure 5.11. Solid line are resolution kernels for the isotropic Rayleigh wave inversion. Dotted line is the input model.

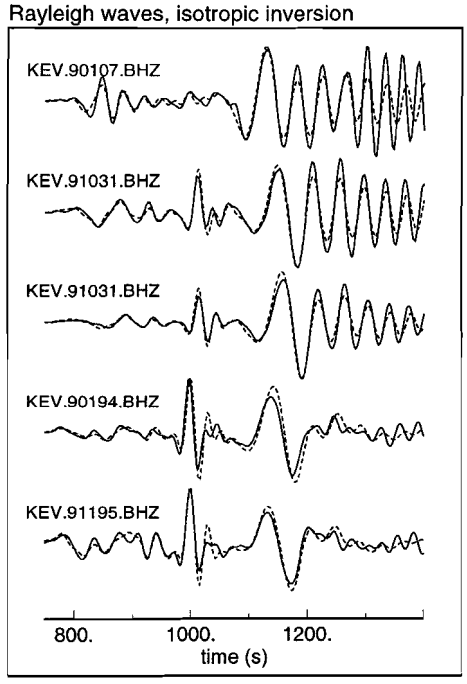

Figure 5.15: Waveform fit for Rayleigh waves for the model obtained by the isotropic inversion. Solid line is the data bandpass filtered between $20 < T < 200s$. Dashed lines are the synthetics for the average model displayed in Figure 5.11.

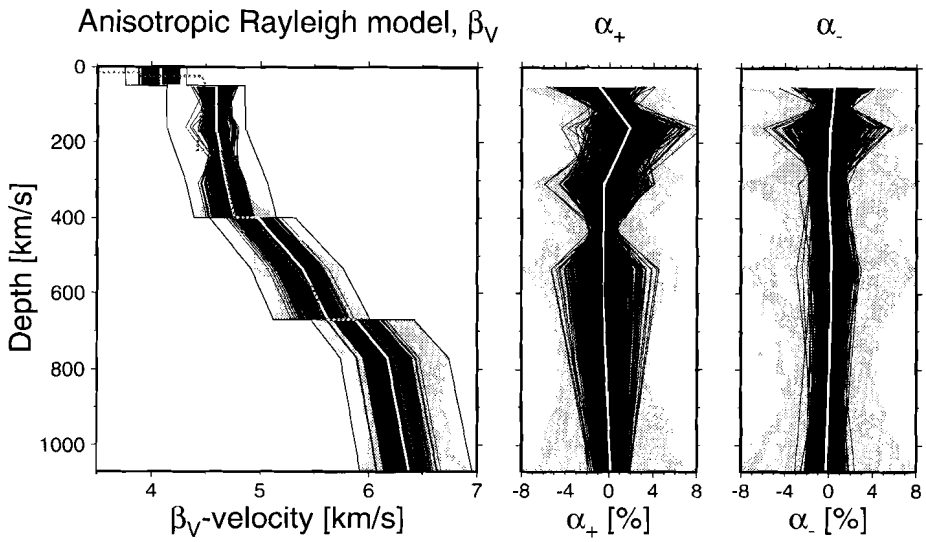

Figure 5.16: Anisotropy model for β_V, α_+ and α_- obtained by the Monte Carlo inversion of Rayleigh data. The gray lines are 322 successful models. The black lines are the filtered models with parameter uncertainty $M_i = 2\%$. The white line is the average model. The dark dashed line is the PREM model.

5.8 Inversion : Rayleigh waves, Anisotropy

We have also inverted the Rayleigh wave data set for anisotropy. As shown in chapter 3, Rayleigh waves in transverse isotropic medium are mainly sensitive to three parameters : the vertical polarized shear velocity β_V, the average of the horizontal and vertical compressional velocity α_+ and the difference in the horizontal and vertical compressional velocity α_-. We initially used the same depth parameterization as in the previous inversion. This resulted in $3 \times 12 = 36$ inversion parameters. In an extensive Monte Carlo search with 1.000.000 tested models we found 130 models that passed the misfit criterion equation 5.7. However the resolution analysis carried out on this ensemble for $M_i = 2\%$ showed that the average model was very poorly resolved. This poor resolution could be due to a insufficient sampling of the model space or to the existence of several clusters of successful models in the ensemble (see Douma et al. 1996). We have therefore reduced the number of parameters dramatically to only five depth layers, thus resulting in totally 15 parameters, see Table 5.3. For this parameterization we obtained 322 successful models after 600.000 tested models.

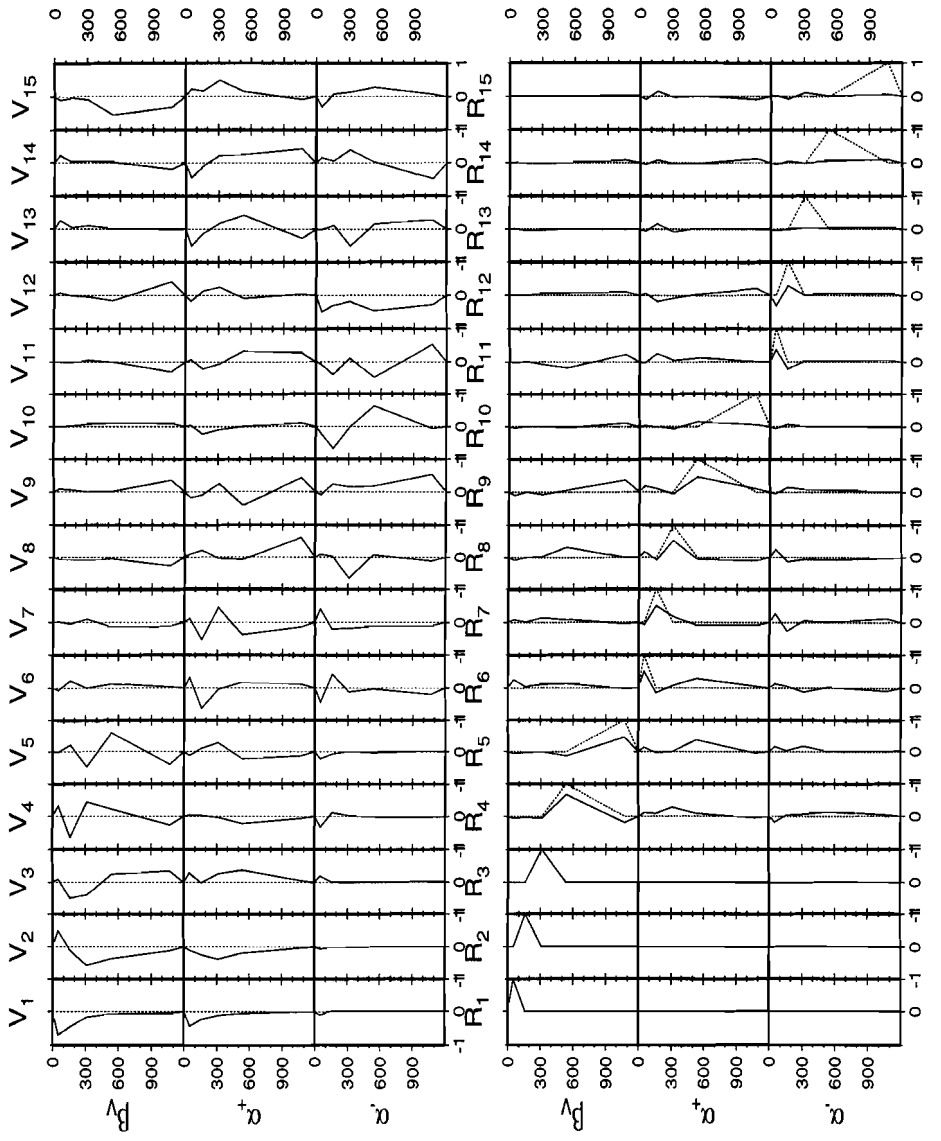

Figure 5.17: (a) Eigenvectors for the anisotropic inversion. (b) Resolution kernels for the anisotropic inversion.

The unfiltered ensemble already shows that β_V is well constrained in the lithosphere due the to thick layer parameterization, see Figure 5.16. The β_V model is not very different from the β_V model obtained in the isotropic inversion indicating little trade-off with the anisotropy parameters α_+ and α_-. The ensembles for α_+ and α_- show much scatter and are on average zero. Only at 150 km depth an anomaly of $\alpha_+ = +2\%$ is observed.

The eigenvalue spectrum for the anisotropic inversion is very similar to that of the isotropic inversion, see Figure 5.12. One may speculate whether this means that the same number of independant parameters can be retrieved in both inversions. The eigenvalue truncation for the first three parameters is maximum which means that these layers are perfectly resolved. The eigenvectors are shown in Figure 5.17a. The best determined eigenvector V_1 is sensitive to the first layer of all three parameters. The other well determined eigenvectors ($V_2 - V_5$) are mainly sensitive to both β_V and α_+. Note that there are few eigenvectors that are sensitive to β_V, α_+ and α_- together. The resolution kernels show that β_V is very well resolved for a parameter uncertainty $M_i = 2\%$, see Figure 5.17b. Also α_+ is well resolved in the upper mantle but α_- is poorly resolved.

It is difficult to say if the observed 2% anomaly in α_+ between 100 km and 220 is required by the data. The resolution kernel for this layer, R_7, shows a good but not perfect resolution for parameter uncertainty $M_i = 2\%$. The data misfits for the isotropic and anisotropic models are very similar.

5.9 Discussion and conclusion

The applied Monte Carlo waveform inversion method in combination with the resolution analysis has proved to be a very powerful method. First of all the average model of the ensemble of successful models gives excellent data fits. The interpretation of Kennett and Nolet's criterion (equation 5.13) for the truncation of the eigenvalue spectrum in terms of parameter uncertainty allows us to estimate the resolution as function of the uncertainty in the model parameters. With the resolution analysis we have shown several aspects for the waveform inversion. First we have shown that higher modes indeed improve the resolution of the inversion. In particular the shear velocity model derived from the Rayleigh wave data set is well resolved down to 1000 km depth. We have also shown that the joint inversion of several events improves the resolution compared to inversion of single events. The resolution analysis for the anisotropic inversion of Rayleigh wave data has showed that it possible to retrieve α_+ from Rayleigh wave data but that α_- is only poorly resolved in the lithosphere. Unfortunately significant variations in these parameters have not been observed in the real data.

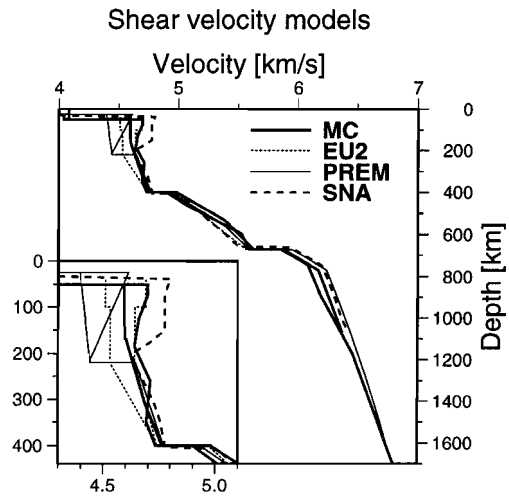

Figure 5.18: Comparison of shear velocity models

The obtained shear velocity models which we will call the MC models are very similar. Only in the lithosphere β_H is 2% larger than β_V. The variations in β_V for the isotropic and anisotropic inversion are very small (less than one percent). Below 220 km both the β_H and the β_V model are similar to each other and to the average earth model PREM, see Figure 5.18. β_H in the lithosphere is almost identical to the EU2 model which has been derived for the same region (Lerner-Lam and Jordan, 1987, Gee and Jordan, 1988). On the other hand, our β_V model is faster than the corresponding EU2 model (Lerner-Lam and Jordan, 1987). The SNA model for the Canadian Shield has high SH-velocity lid in the lithosphere overlying a slower mantle (Grand and Helmberger, 1984). A high velocity lid is not observed under Central Eurasia in both our MC model and the EU2 model.

The observed shear wave anisotropy in the MC model is smaller than in PREM and EU2. We have computed the difference in one way vertical travel time of β_H - β_V. From EU2 we find t=1.6 s, for PREM, t=1.2 s and for MC t=0.5 s. We think that the reason for the small one way vertical travel difference in our model is the crustal correction applied to the synthetic waveforms. After applying the crustal correction we observed that the difference between Love and Rayleigh waves velocities had become smaller. This effect of reduced transverse isotropy when an improved crustal model is used has been described by Levshin and Ratnikova (1984). With better crustal models and modeling techniques the observed difference in β_H and β_V may become even smaller. In the anisotropic inversion a 2% anomaly in α_+ at a depth between 100 and 220 km has been observed. This parameter, which is the difference between the horizontal and vertical compressional velocities, is reasonably well resolved but the observed value is probably not significantly different from zero.

Chapter 6

Deep structure of the East Pacific Rise determined by adaptive Monte Carlo waveform inversion

6.1 Abstract

Central American events recorded by the seismic station RPN on Easter Island provide a unique data set of pure path data sampling the East Pacific Rise. We study the upper mantle shear velocity structure of the East Pacific Rise by the inversion of fundamental and higher modes Rayleigh waves up to the direct S wave extracted five high quality seismograms. The waveform inversion is based on Bayesian inference theory. Initial attempts to invert the data using gradient methods were without success as the inversion got stuck in local minima arising from the fact that we fitting more than one seismogram simultaneously. We therefore changed to a more global method, an adaptive Monte Carlo method based on the VEGAS algorithm. With this algorithm we have carried out a Bayesian inversion and obtained the marginal probability density function for each parameter. Synthetics tests of the algorithm show that it has a good performance also when correlations between parameters are present. We apply the VEGAS algorithm to the Bayesian inversion of waveform data. The presented model for the East Pacific Rise shows that in the upper 200 km under this fast spreading ridge the shear velocity is -5% lower than in the average earth model PREM. Below 200 km deep the velocities differ less than 2% from PREM and the marginal probability density functions show that this difference is not significant. The two-dimensional marginal probability density functions show that when the model space is parameterized by more than five layers strong trade-off's between the parameters exist.

6.2 Introduction

Mid-Ocean Ridges are a surface expression of mantle convection. A basic, still unresolved question involving Mid-Ocean Ridges is the depth origin of the hot up-welling material. The answer to this question has direct implications for dynamical models of the spreading of the oceanic lithosphere.

The structure and dynamics of the ridges have been studied by various geophysical methods (e.g. Phipps Morgan 1991; Forsyth 1992). Seismic studies have revealed at shallow depths under fast spreading ridges a shallow narrow magma lens (e.g. Detrick et al. 1993). The uppermost mantle under such a ridge is anisotropic which is in agreement with the expected mantle flow in the region (Blackman et al. 1993).

Information about the deeper structure of the ridges comes from surface wave data and is rather conflicting. Using very long period Rayleigh waves Wielandt and Knopoff (1982) found evidence for velocity anomalies down to 450 km depth under the East Pacific Rise with respect to the 1066B model. On the other hand, the regionalized surface wave study by Nishimura and Forsyth (1988) showed that young oceanic lithosphere surrounding the ridge axis in the Pacific has only significantly lower velocities down to a depth of 100 km. On a global scale, again using fundamental mode dispersion data alone, Zhang and Tanimoto (1992) concluded that the depth extend of the mid-ocean ridges is limited to 100 km favoring the passive up-welling of mantle material. However Su et al. (1993) concluded by the analysis of S-SS travel time residuals that the ridges are continues features that extend to 300 km and possible 600 km depth. We think these conflicting results are caused by the poor depth resolution of both the long period fundamental mode and the S-SS travel-time residuals which are integrals over the depth velocity. The depth resolution of the seismic models can be improved when higher modes are added to the dataset (e.g. Nolet 1977; Cara, Nercessian and Nolet, 1980)

In this paper we determine the seismic structure of the East Pacific Rise using high-quality waveform data. Data is used from five central American events recorded by the IRIS station RPN located on Easter Island, see figure 6.1. The source-receiver paths sample almost entirely oceanic lithosphere of age younger than 10 Ma and all paths cross the ridge axis. From the selected seismograms we use the fundamental and higher mode Rayleigh waves including the S and SS phases in the period range $20s < T < 200s$. Although the initial dataset had large variations in the waveform data, after testing all events on the reliability of frequency components due to the source uncertainties (see Muyzert and Snieder 1996) and checking on a good signal to noise ratio, a remarkable clean dataset has been obtained.

We invert the waveform data directly for shear velocity. Bayesian inference theory is used to estimated the uncertainties in the model parameters. The Bayesian approach requires knowledge of the uncertainties in the data. Determination of the uncertainty of waveform data is not trivial. In controlled source experiments waveforms from different shots can be stacked and the variance in each sample can

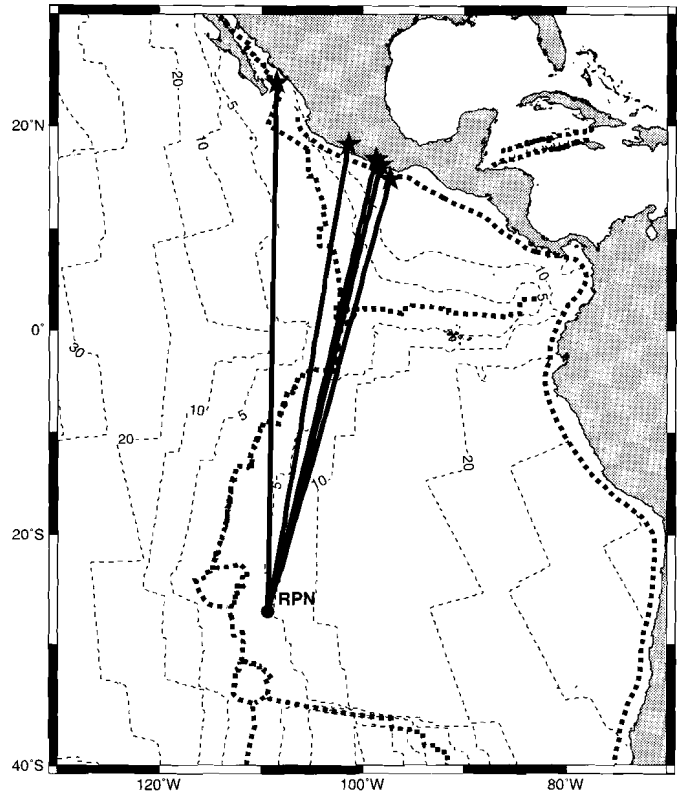

Figure 6.1: Geographic and tectonic settings of the Eastern Pacific. The source-receiver paths for the events (indicated by stars) and the seismic station RPN (circle) used in this study are drawn in thick dark lines. The plate boundaries are indicated by thick dashed lines, the East Pacific Rise is the main North-South line near $110°W$. Thin dashed lines are contour lines of the lithospheric age after Mueller et al. (1997)

be determined (see Sen and Stoffa, 1996ab). For earthquake data this is not possible as the events have different source mechanisms. Because we compare observed data with synthetic data the uncertainty is also influenced by the theory used for the computation of synthetic data and the uncertainty in the source mechanism. As these uncertainties are very difficult to quantify we estimate the uncertainty of the waveform data from the difference between observed and synthetic waveforms in an initial run under the assumption that the data errors follows a Gaussian distribution. Using Bayesian theory we compute the one-dimensional marginal probability density functions for each model parameter. In addition, correlations between the parameters are inspected using the two-dimensional marginal pdf's. The two-dimensional marginal pdf's describe the probability of combinations of two model parameters and are a generalization of the covariance matrix.

For the inversion of waveform data we have experimented with both local and global methods. Linearized waveform inversions have been performed with long period surface wave and body wave data (e.g. Woodhouse and Dziewonski, 1984, Tanimoto, 1991). In these studies no special weighting on the data is applied which results in a dominance of the large amplitude fundamental mode with respect to the smaller amplitude higher modes and body waves. When shorter period waveform data is used the inverse problem becomes less linear and localized gradient methods can be applied (see Nolet, van Trier en Huijsman, 1986). In this approach fundamental and body wave phases as S and SS waveform are separated from the seismogram and are inverted using different amplitude weights for path averaged velocity structure. Initially we followed Nolet's approach and attempted to invert waveform data for path averaged velocity structure. However the inversion of waveform data from more than one events turned out to be rather difficult. Although the seismograms sampled the same region, due to the different sources the waveforms are significantly different which gives non-linearities in the inversion. In addition, noise in the data and uncertainties in the source parameters complicated the misfit function.

These problems can be overcome when a global inversion method is used. Seismic refraction data has been successfully inverted using Monte Carlo sampling (e.g. Cary and Chapman 1989; Sen and Stoffa, 1996ab). To increase the effiency of the search, Sen and Stoffa (1996ab) also used iterative adaptive Monte Carlo methods. Adaptive Monte Carlo methods first sample the model space uniformly, whereas in later iterations most samples are taken from the regions of the model space where the best models are located. In this paper we will use such a Monte Carlo method which allows us to find the global minimum and correctly handles the non-linearity of the surface waveform inversion. We use the adaptive Monte Carlo search algorithm VEGAS described by Lepage (1978). This algorithm allows us to sample the model-space close to the marginal probability density function (pdf) of each model parameter which makes the algorithm rather efficient for this type of problems.

6.3 Bayesian inversion

One of the objectives of this paper is to treat the uncertainties in the data and model parameters properly through the inversion. This can be done with Bayes's rule (Bayes, 1763). Bayes's rule describes the state of information of the model parameters $\mathbf{m}$ given the data $\mathbf{d}$ as the conditional probability $\Phi(\mathbf{m} \mid \mathbf{d})$.

$$\Phi(\mathbf{m} \mid \mathbf{d}) = \frac{\rho(\mathbf{d} \mid \mathbf{m})\rho(\mathbf{m})}{\rho(\mathbf{d})} \tag{6.1}$$

In equation 6.1, $\rho(\mathbf{d})$ describes the probability of the data, $\rho(\mathbf{m})$ is the prior knowledge of the probability of the model parameter and $\rho(\mathbf{d} \mid \mathbf{m})$ the conditional probability of the data for a given model. The model $\mathbf{m}$ is represented by a vector

with length M and the data $\mathbf{d}$ by a vector with length D.

$$\mathbf{m} = [m_1, m_2, \cdots m_M]^T$$
$$\mathbf{d} = [d_1, d_2 \cdots d_D]^T$$

For inverse problems, Bayes's rule is written as

$$\Phi(\mathbf{m} \mid \mathbf{d}) = c \cdot l(\mathbf{d}, \mathbf{m}) \cdot \rho(\mathbf{m}) \tag{6.2}$$

(see Tarantola 1987; Duijndam 1988; Cary and Chapman 1988). In equation 6.2 the constant c represents the probability density function (pdf) of the data $1/\rho(\mathbf{d})$ which can be treated as a constant during the inversion since it is independent of the model parameters. The likelihood function $l(\mathbf{d}, \mathbf{m})$ measures the difference between the data and the synthetic data obtained by the forward modeling operator $g(\mathbf{m})$. The prior pdf $\rho(\mathbf{m})$ describes the knowledge of the model space before inversion.

When Gaussian statistics are used an analytical expression for Φ can be derived. For a Gaussian distribution of the data the likelihood function is given by

$$\begin{gathered} l(\mathbf{d}, \mathbf{m}) = (2\pi)^{-M/2} \mid \mathbf{C}_d \mid^{-1/2} \exp[-\tfrac{1}{2}\mathbf{e}_d^T \mathbf{C}_d^{-1} \mathbf{e}_d] \\ \mathbf{e}_d = \mathbf{d} - \mathbf{g}(\mathbf{m}) \end{gathered} \tag{6.3}$$

with $\mathbf{C}_d$ the covariance matrix of the data. $\mathbf{e}_d$ is the difference of the measured and synthetic data. Gaussian prior information about the model parameters is given by

$$\begin{gathered} \rho(\mathbf{m}) = (2\pi)^{-M/2} \mid \mathbf{C}_m \mid^{-1/2} \exp[-\tfrac{1}{2}\mathbf{e}_m^T \mathbf{C}_m^{-1} \mathbf{e}_m] \\ \mathbf{e}_m = \mathbf{m} - \mathbf{m_p}(\mathbf{m}) \end{gathered} \tag{6.4}$$

with $\mathbf{C}_m$ the prior covariance matrix for the data and $\mathbf{m_p}$ the prior expectation value for the model parameters.

When the prior information is combined with the likelihood function the following solution of the inverse problem Φ :

$$\Phi(\mathbf{m} \mid \mathbf{d}) = \frac{c}{(2\pi)^M \sqrt{\mid \mathbf{C}_d \mid\mid \mathbf{C}_m \mid}} \exp \frac{1}{2}[-\mathbf{e}_d \mathbf{C}_d^{-1} \mathbf{e}_d - e_m \mathbf{C}_m^{-1} \mathbf{e}_m] \tag{6.5}$$

For a non-Gaussian distribution of the data and prior information non-Gaussian expressions should be used (e.g. Tarantola, 1987; Duijndam, 1987). The inverse problem is non-linear when $\mathbf{e}_d$ depends non-linearly on the model parameters. Another type of non-linearity is introduced in the inversion when the prior knowledge of the model space is asymmetric or has more peaks. The inverse method we described in this paper should in principle be capable to treat both kinds of non-linearity.

The exact solution of $\Phi(\mathbf{m} \mid \mathbf{d})$ requires a thorough evaluation of the whole model space which can be very time-consuming. Another problem is that visual inspection of $\Phi(\mathbf{m} \mid \mathbf{d})$ can be rather complicated due to the high number of

dimensions. For these reasons, several estimates of $\Phi(\mathbf{m} \mid \mathbf{d})$ such as the mean model and the posterior covariance matrix are often used. The mean model is defined by :

$$\langle \mathbf{m} \rangle = \int \mathbf{m}\Phi(\mathbf{m} \mid \mathbf{d}) d\mathbf{m} \tag{6.6}$$

The posterior covariance model matrix is given by :

$$\mathbf{C_m} = \int (\mathbf{m} - \langle \mathbf{m} \rangle)(\mathbf{m} - \langle \mathbf{m} \rangle)^T \Phi(\mathbf{m} \mid \mathbf{d}) d\mathbf{m} \tag{6.7}$$

Both the expectation value and the covariance are useful estimates for single peaked, fairly symmetric functions. More complicated functions require the evaluation of the marginal pdf's. The posterior one-dimensional marginal pdf of each model parameter is defined as :

$$\Phi(m_i \mid \mathbf{d}) = \int \Phi(\mathbf{m} \mid \mathbf{d}) \prod_{m=1, m \neq i}^{M} dm_m \tag{6.8}$$

Correlations between the parameters can be inspected with the two-dimensional marginal pdf which is defined similar to the 1D marginal pdf as :

$$\Phi(m_i, m_j \mid \mathbf{d}) = \int \Phi(\mathbf{m} \mid \mathbf{d}) \prod_{m=1, m \neq i,j}^{M} dm_m \tag{6.9}$$

For the waveform inversion problem we do not know how peaked and symmetric $\Phi(\mathbf{m} \mid \mathbf{d})$ is. We therefore will present the inversion results in the form of 1D and 2D marginal pdf's. By using the marginal pdf's we can determine the uncertainty in the model parameters and investigate possible correlation between parameters and find local minima.

6.4 Numerical integration

Integrals such as those for the posterior pdf (equations 6.8 and 6.9) can be solved by numerical integration methods (for reviews of the various approaches see Sen and Stoffa, 1996ab). The main difference between these methods is the way the model space is sampled. The most fully and computational most intense methods are the grid search and the Monte Carlo search which sample the entire model space with a uniform sample density. Specially for higher dimensions these methods are very inefficient as the whole model space is sampled with the same sample density including those areas that have a small contribution to the integrand. The efficiency of the Monte Carlo method can greatly be improved with importance sampling (see Hammersly and Handscomb, 1964). Importance sampling algorithms gain their efficiency by sampling the integrand according to the contribution of each

region to the integrand. Again more efficient but also less accurate are Maximum A Posteriori (MAP) estimates. These methods use global search methods as Genetic Algorithm and Simulated Annealing which rapidly converge. MAP estimates have the disadvantage that parts of the model space that contribute little to the integrand are underestimated and are therefore only useful for smooth localized pdf's (see Sen and Stoffa 1996ab).

For many inverse problems the shape of the marginal pdf's is unknown which makes the use of MAP estimates a bit dangerous. Importance sampling methods provide a better compromise between efficiency and accuracy than the MAP estimates. In this paper we will use the VEGAS importance sampling algorithm (see Lepage 1978). The main reason for this choice is that from this algorithm the marginal pdf's can be determined in a very natural way. The VEGAS algorithm uses all model evaluations for its iterative process unlike other methods such as the Metropolis random walk (see Mosegaard and Tarantola, 1995)

6.4.1 VEGAS importance sampling

In this section we will review the VEGAS algorithm following Lepage (1978) and Press et al. (1992). We want to solve multidimensional integrals such as equations 6.6 to 6.9. The integral of a function of the model $\mathbf{m}$ over a volume Ω is given by

$$I = \int_{\Omega} f(\mathbf{m}) d\mathbf{m} \tag{6.10}$$

An importance sampling algorithm samples such an integral with a non-uniform multi-dimensional sample distribution $P(\mathbf{m})$. The integrand I over the volume Ω can be estimated by sum over all N function values corrected for the sample density $P(\mathbf{m})$.

$$I \approx \frac{1}{N} \sum_{n=1}^{N} \frac{f(\mathbf{m})}{P(\mathbf{m})} \tag{6.11}$$

The standard deviation σ of integrand can be estimated by

$$\sigma = \sqrt{\frac{S^2 - I^2}{N-1}} \tag{6.12}$$

with

$$S^2 = \frac{1}{N} \sum_{n} \frac{f^2(\mathbf{m})}{P^2(\mathbf{m})} \tag{6.13}$$

The number of samples can greatly be reduced with a proper choice of the sample distribution. The VEGAS algorithm implicitly assumes that the sample distribution is separable for all parameters

$$P(\mathbf{m}) = p_1(m_1)p_2(m_2)\cdots p_M(m_M) \tag{6.14}$$

where $p_m(m_m)$ is the one-dimensional, non-uniform sample distribution for the m^{th} model parameter. Further on we will denote $p_m(m_m)$ by p_m. The optimum sample distribution for the estimation of the integrand is obtained by minimizing the standard deviation given by equation 6.12. The optimum separable sampling distribution is given by

$$p_1 = \bar{f}(m_1) \Big/ \int_{m_1} \bar{f}(m_1)\, dm_1 \tag{6.15}$$

with

$$\bar{f}(m_1) = \left[\int_{m_2} \int_{m_3} \cdots \int_{m_M} \frac{f^2(\mathbf{m})}{p_2 p_3 \cdots p_M} dm_2 dm_3 \cdots dm_M \right]^{\frac{1}{2}} \tag{6.16}$$

and corresponding expressions for p_2, $p_3 \cdots p_M$, see Lepage (1978); Press et al. (1992).

The VEGAS algorithm is an iterative algorithm. In the first iteration of VEGAS the function $f(\mathbf{m})$ is sampled using a uniform sample distribution. In later iterations the sample distribution is adapted using equation 6.15 to approximate the optimum sample distribution more closely. For each iteration, VEGAS computes the integrand I_k and its standard deviation σ_k using equations 6.11 and 6.12. After K iterations the VEGAS algorithm returns a mean weighted integral estimate and the standard deviation over all the iterations that improve the convergence rate even further. The mean weighted integral estimate is given by :

$$I_K = \sum_{k=1}^{K} \frac{I_k}{\sigma_k^2} \Big/ \sum_{k=1}^{K} \frac{1}{\sigma_k^2} \tag{6.17}$$

and the estimated variance of the integral

$$\sigma_K^2 = \left(\sum_{k=1}^{K} \frac{1}{\sigma_k^2} \right)^{-\frac{1}{2}} \tag{6.18}$$

Also returned is the quantity

$$\frac{\chi^2}{K} = \frac{1}{K-1} \sum_{k=1}^{K} \frac{(I_k - I_K)^2}{\sigma_k^2} \tag{6.19}$$

If χ^2/K is significantly larger than 1 the estimation of the integrand is suspect.

6.4.2 Inversion using VEGAS

Suppose that the posteriori probability density function Φ, which is the general solution of the inverse problem, is separable for each model parameter. Φ is then equal to the product of the marginal probability density functions :

$$\Phi(\mathbf{m} \mid d) = \Phi_1(m_1 \mid d)\Phi_2(m_2 \mid d) \cdots \Phi_M(m_M \mid d) \tag{6.20}$$

The VEGAS algorithm determines the optimum separable sample distribution P which has the same shape as Φ. In that case the sample distribution along each axis becomes equal to the marginal probability density function for that axis

$$p_i = \Phi_i(m_i) \tag{6.21}$$

There are two reasons why equation 6.21 can not be used for real applications. First, the number of iterations of VEGAS is always limited. This results in only an approximated optimum separable sample distribution and equation 6.21 would give us only approximated marginal pdf's. Secondly, we have assumed that Φ is separable. This is surely not always the case for geophysical inverse problems. An example of a non-separable function is a function with trade-off's or correlations between the parameters e.g.

$$f(\mathbf{m}) = \exp -[{m_1}^2 - 2m_1 m_2 + {m_2}^2] \tag{6.22}$$

This type of trade-off does occur in inversions when the model space is over-parameterized. Over-parameterization leads to large uncertainties in the estimated model parameters and trade-off's between the model parameters. These effects can be suppressed by introducing smoothness constraints on the model parameters. Smoothness contraints can be included in the VEGAS algorithm by introducing prior information given by equation 6.4 where the off-diagonal terms of $\mathbf{C_m}$ determine the smoothness of the model. In the next section we show that the VEGAS algorithm can also be applied to such non-separable functions with trade-off's between the parameters.

We present the solution of the inverse problem as marginal pdf's that are computed using equations 6.8 and 6.9. The results of the last iteration of VEGAS are used as it has a sampling distribution which approximates the marginal pdf. Each parameter axis is divided into H bins with bin-width $\Delta m_{1,h}$. In discrete notation the one-dimensional marginal pdf $\Phi_{1,h} = \Phi_{1,h}\left(m_{1,h} | \mathbf{d}\right)$ at bin h of the first coordinate axis is written as

$$\bar{\Phi}_{1,h} = \sum_{m_1 \in \{m_{1,h} - \Delta m_{1,h}, m_{1,h}\}} \sum_{m_2} \cdots \sum_{m_M} \frac{\Phi\left(\mathbf{m} \mid \mathbf{d}\right)}{p_{1,h} p_{2,h} \cdots p_{M,h}} \tag{6.23}$$

Similar to the uncertainty in the integrand (see equation 6.12) we can estimate the uncertainty in the one-dimensional marginal pdf. Thus the standard deviation of each bin is given by :

$$\sigma_{1,h} = \sqrt{\left[S^2_{1,h} - \bar{\Phi}^2_{1,h}\right] / N_{1,h}} \tag{6.24}$$

$S_{1,h}$ is defined as :

$$S^2_{1,h} = \sum_{m_1 \in \{m_{1,h} - \Delta m_{1,h}, m_{1,h}\}} \sum_{m_2} \cdots \sum_{m_M} \left[\frac{\Phi\left(\mathbf{m} \mid \mathbf{d}\right)}{p_{1,h} p_{2,h} \cdots p_{M,h}}\right]^2 \tag{6.25}$$

with N_h the number of models that falls within the bin. For the two-dimensional marginal pdf a similar expression can be derived.

The convergence and accuracy of the algorithm can be checked in several ways. An indication for poor convergence of the algorithm is found when the estimates of the integrand and sample distributions vary significantly during the iterations. Another indication for poor convergence is when $\chi^2 > K$, see equation 6.19. When the standard deviations in the bin's are large, in particular in the important parts of the integrand, we can decrease the number of bins along each axis in order to increase the accuracy in the bin's. This would only work when the bin size is smaller then the important features of the function. Higher accuracy is also obtained with a larger number of function calls in each iteration and by performing extra iterations.

6.5 Test

We illustrate the behavior of the VEGAS algorithm with a synthetic test. We have defined a likelihood function that could represent the solution of an inverse problem. For this likelihood function we compute 1D and 2D marginal pdf's and compare them with Monte Carlo and analytical results. The likelihood function is defined in five dimensions by :

$$E(\mathbf{m}) = 10000 \exp\left[\sum_{i=1}^{4} -\frac{(m_i + m_{i+1} - 1)^2}{2 \times 0.1^2} - \frac{(m_i - m_{i+1})^2}{2 \times 0.1^2}\right] \tag{6.26}$$

This likelihood function is centered at $m_i = 0.5$ and has correlations between neighboring parameters. It is defined on the interval $0 \leq m_i \leq 1$. In figures 6.2 and 6.3 we show the exact 1D and 2D marginal pdf's for this likelihood function. For this likelihood function good 1D marginal pdf's have been obtained by the VEGAS algorithm in 3 iterations of 6.200 function evaluations, see figure 6.2. The 1D marginal pdf's have been calculated for 30 bins along each axis and a three-point smoothing filter has been applied. The estimated error in the 1D marginal pdf computed using equation 6.24 is small which indicates that the 1D marginal pdf is accurate, see figure 6.2. To obtain a similar accuracy with the pure Monte Carlo method, 300.000 functions evaluations where needed, see figure 6.2. The VEGAS algorithm estimates of the uncertainty are more uniformly distributed than the Monte Carlo estimates.

The 2D marginal pdf's for this test are shown in figure 6.3. Note that the contours are plotted on a log10 scale. Both the VEGAS and the Monte Carlo run find the peak at the right location and the correlation in the proper direction. Figure 6.3 also shows that VEGAS underestimates the low amplitude regions of the 2D marginal pdf's. This is due to the fact that VEGAS focuses on the high amplitude regions and thus only poorly samples the low amplitude regions. This test shows that the VEGAS algorithm is capable of imaging likelihood functions with correlations between the parameters.

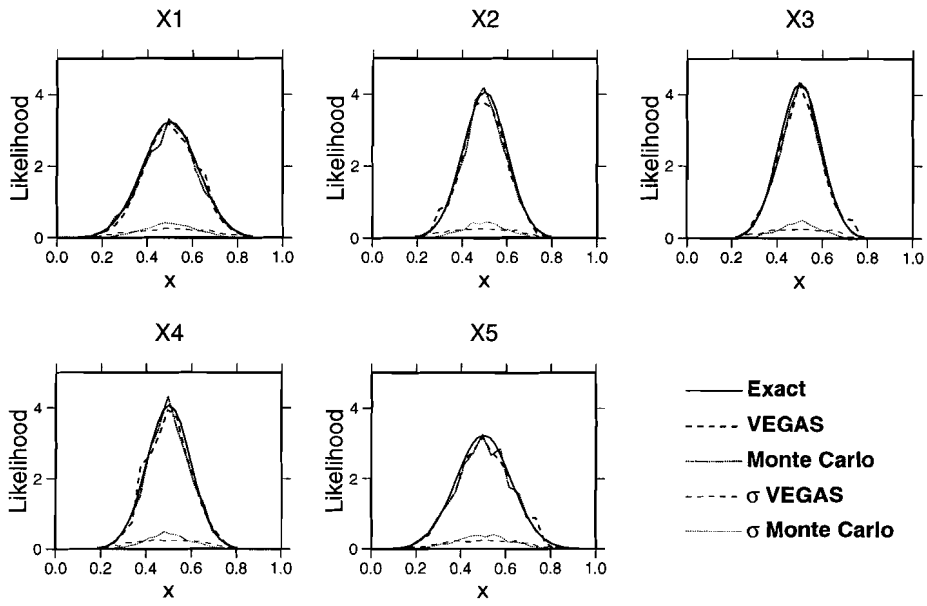

Figure 6.2: One-dimensional marginal probability density functions for the test function defined by equation 6.26. The thick solid represents the exact solution, the thick dashed line the solution estimated using VEGAS, the thick dotted line the Monte Carlo estimate. The thin dashed and dotted lines are the estimated standard deviations of the VEGAS and Monte Carlo solution.

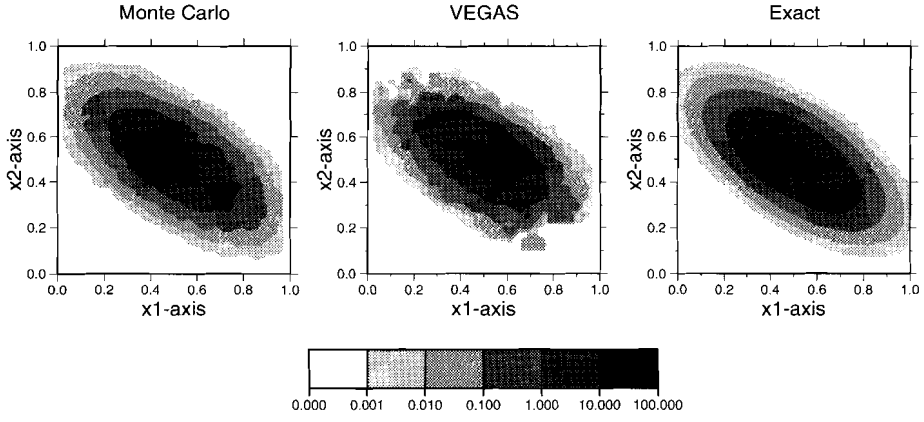

Figure 6.3: Two-dimensional marginal probability density functions for the first and second parameter of the test function. Left figure is the Monte Carlo estimate, the middle figure the VEGAS estimate and the right figure is the exact solution. Note that the contour scale is logarithmic.

6.6 Inversion of waveform data

In this section we discuss the application of the VEGAS algorithm to the inversion of waveform data. We use seismograms from events with magnitude $M_w \geq 5.5$ recorded at epicenteral distances $\Delta \leq 60°$. The seismograms are filtered both in the time and frequency domain in order to isolate the different waves, similar to the partitioned waveform inversion method developed by Nolet (1990). The part of the seismogram from the direct S wave up to the short period fundamental mode in the frequency range 20 – 200 s is used. This part of the seismogram is characterized by large amplitude and frequency variations. Four windows that are sensitive to the shear wave velocity structure at different depths are defined, see table 6.1. The window containing the short period fundamental modes samples the lithosphere down to a depth of 200 km. the long period fundamental mode samples the average velocity of the entire upper mantle. The higher mode window around the SS phase samples roughly the same region as the long period fundamental mode but with a different depth sensitivity. The last window that contains the S phase samples the transition zone and parts of the lower mantle. By simultaneous inversion of the four windows a high resolution with depth can be obtained as both fundamental and higher modes are used.

The excitation of the surface wave modes is dependent on the source mechanism and source depth. We therefore invert all the seismograms simultaneously. This improves the resolution as the higher mode data is better constrained, see chapter 5. Another reason for the joint inversion is that we can estimate the uncertainty in the waveform data as we have more than one measurement along the same source-receiver path. If the events would have the same source mechanism the seismograms could be stacked and the likelihood function could be determined. This approach is followed by Sen and Stoffa (1996ab) who applied source deconvolution on the seismic data and assumed a Gaussian distribution of the data. Stacking of earthquake data is not possible as we deal with different source mechanism.

After the seismograms are filtered, the energy in the remaining data-windows is normalized in order to remove amplitude uncertainties :

$$\tilde{D}(t) = \frac{D(t)}{\sqrt{\int_{t=T_1}^{t=T_2} D^2(t)dt}} \tag{6.27}$$

Such normalization is necessary as the different events have different source strength

Data type	Period (s)	V_g (km/s)	σ^2
Short Period Fundamental mode	30 - 100	3.3 - 4.2	0.01
Long Period Fundamental mode	100 - 200	3.1 - 5.0	0.04
Higher modes and SS-phase	20 - 70	4.2 - 4.8	0.25
Higher modes and S-phase	20 - 70	4.9 - 6.4	0.25

Table 6.1: Definition of data windows

and because the amplitude of the waveform is very sensitive to attenuation and three dimensional propagation effects (focusing). We measure the difference between the data $\tilde{D}(t)$ and the synthetic seismogram $\tilde{S}(t, \mathbf{m})$ by the L^2 norm. This data misfit function is defined as :

$$\xi^2 = \int_{t=T_1}^{T_2} \left[\tilde{D}(t) - \tilde{S}(t, \mathbf{m})\right]^2 dt \tag{6.28}$$

We define the likelihood function for the waveform inversion similar to Cary and Chapman (1988) by :

$$l(\mathbf{d}, \mathbf{m}) = \exp\left[-\sum_{i=1}^{I}\sum_{d=1}^{D_i} \frac{\xi_{i,d}(\mathbf{m})^2 - \xi_{i,0}^2}{2\sigma_i^2}\right] \tag{6.29}$$

In equation 6.29 we sum over all events I and all data windows D_i. This likelihood function is different from the Gaussian distribution given by equation 6.5 as we subtract a constant $\xi_{i,0}$ from the misfit. Due to the presences of noise in the waveforms the difference between the real and the synthetic data, ξ is for realistic models never zero. Thus the maximum likelihood point of the Gaussian function would never be obtained. The distribution of the likelihood function for all models would follow an exponential decay which makes the estimated marginal pdf's very rough. Therefore it is necessary to subtract the misfit of the best model $\xi_{i,0}$ from the ξ. Now the best models are located in the flat part of the Gaussian function within a standard deviation of the mean. We determine $\xi_{i,0}$ from the data by taking it as the misfit of the best model found in the inversion. This model is of course only known after the inversion. We therefore determine in each iteration the best fitting model and update our estimate of ξ_0. This procedure is neccesary for practical reasons but is not purely Baysian as the a-priori information ξ_0 is determined from the data, see Scales and Snieder (1997). By the subtraction of ξ_0 we up-weight the good models with respect to the poor models. The subtraction of ξ_0 results in a likelihood which is centered around the minimum misfit model.

In the likelihood function we have assumed that the data is independent and thus that covariance matrix $\mathbf{C}_d$ has only diagonal terms which are the variances σ. The variance is determined for each window separately as these windows sample different parts of the earth and have different frequencies and amplitudes. We compute the variance by a summation over all misfits of the same data type.

$$\sigma_i^2 = \frac{1}{D_i - 1}\sum_{d=1}^{D_i} \xi_d^2(\mathbf{m}) \tag{6.30}$$

Like with ξ_0 we have experimented with an iterative approach where the variance is updated after each iteration. This approach lead however to unrealistic small variances that caused convergence problems of the VEGAS algorithm. We therefore have chosen to determine the variance in an initial run and to fixed during the inversion.

6.7 East Pacific Rise

We have collected vertical component broadband seismograms recorded at the IRIS station RPN ($27.13°S$, $109.33°W$) from Central American events. The source-receiver paths of such events sample primarily very young oceanic lithosphere and cross the East Pacific Rise (EPR), see Figure 6.1. The epicentral distance of these events is approximately 45°. We have selected events with a magnitude $M_w \geq 5.5$ in years 1990 - 1994. These events have been checked for the reliability of the frequency components of the expected waveforms with respect to uncertainties in the source parameters, see Muyzert and Snieder (1996). In this procedure synthetic seismograms, computed for perturbed source mechanisms, are compared with each other and only those frequency components that show little variation with the source parameters are used. In this procedure approximately 50% of the data has been rejected as it turned out that many sources had fault plane dipping 45° for which the initial phase is very sensitive. The remaining events have been visually inspected for a good signal to noise ratio in the period range $20 < T < 200$ s. In total we have used 5 high quality seismograms, see table 6.2. The great circle paths of the 5 events used in this study go for more than 50% through very young oceanic lithosphere with an age less than 5 MY and all cross the EPR (see figure 6.1).

The starting model for the inversion is the PREM model (Dziewonski and Anderson, 1981) with a modified crust. The crustal structure of the starting model is taken from the CRUST5.1 model (see Mooney et al. 1996). For each $5° \times 5°$ cell of this model along the source receiver path we have computed the local phase velocity and corrected the phase velocity of the starting model. The model is parameterized by a number of layers with increasing thickness with depth, see table 6.3. A crustal layer is not included as tests showed that the short period fundamental mode ($T < 30s$) was very incoherent.

For the following two runs we have used the variances listed table 6.1. These have been determined in an initial run were the data was checked on internal consistency using a conjugated gradient scheme similar to Nolet (1990). During the VEGAS inversions we have found smaller values for the variances but we do not want to underestimate the variance as many wave propagation effect have been neglected (e.g. off-plane propagation, mode coupling, uncertainty in crustal structure and attenuation).

Year, month, day	longitude ($°W$)	latitude ($°N$)	depth (km)	Magnitude
1991.04.01 (091)	98.23	16.23	22	5.8
1991.06.22 (173)	108.49	24.41	10	6.1
1993.10.24 (297)	98.73	16.78	32	6.6
1994.07.04 (185)	97.32	14.94	33	6.4
1994.12.10 (344)	101.35	18.24	67	6.4

Table 6.2: Events used in this study

Layer number	depth (km)	
	RUN1	RUN2
1	0 - 100	0 - 60
2	100 - 200	60 - 140
3	200 - 400	140 - 220
4	400 - 670	220 - 400
5	670 - 1471	400 - 670
6	-	670 - 971
7	-	971 - 1471

Table 6.3: Depth parameterization

6.7.1 RUN1, 5 layers

In this first run we have inverted the waveform data set for 5 thick layers, see table 6.3. Each parameter is allowed to vary $\pm 12\%$ around the starting model which is PREM. The algorithm has performed 4 iterations each with 33614 model evaluations. Figure 6.4a shows the best 50 models with the highest likelyhood found during the inversion. These models are located in a cluster indicating that the true model is located in a well defined region. The 1D marginal pdf's for the model parameters we have computed for this run are shown in figure 6.5. They all have a well defined peak and have small uncertainties, indicating a stable solution. The maximum likelihood model has in the first and second layer -5% lower shear velocities than PREM. Below 200 km depth the maximum likelihood model deviates less than 2% from the PREM model. In fact, only the first and second parameter deviate more than a standard deviation from the PREM model. For the 2D marginal probability density functions we show the 68%, 95.4% and 99.73% confidence limits in figure 6.6. All parameters show correlations with neighboring parameters. From the 68% confidence limits drawn in figure 6.6 we estimate the average uncertainty in the maximum likelihood model as 3%. In the deeper layers the resolution decreases slihtly.

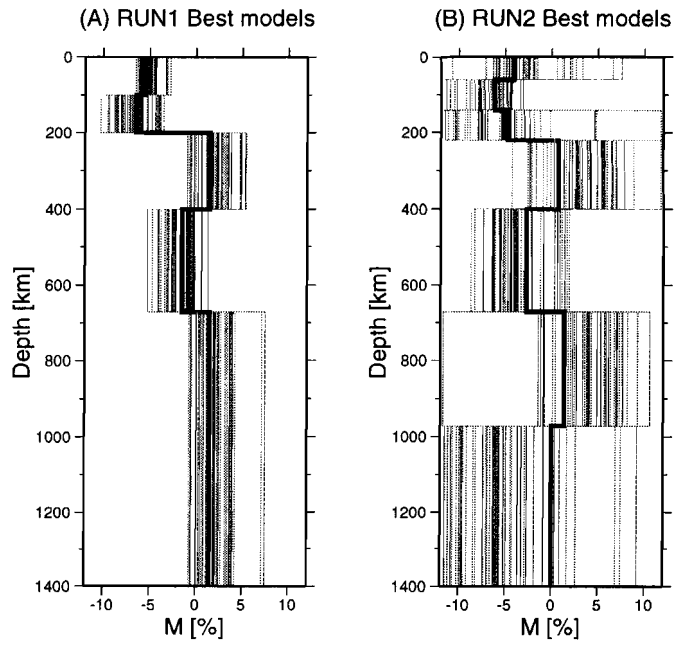

Figure 6.4: (a) Best 50 models with highest likelyhood found in RUN1. The thick solid line represents the maximum likelihood model. (b) Best 50 models found in RUN2.

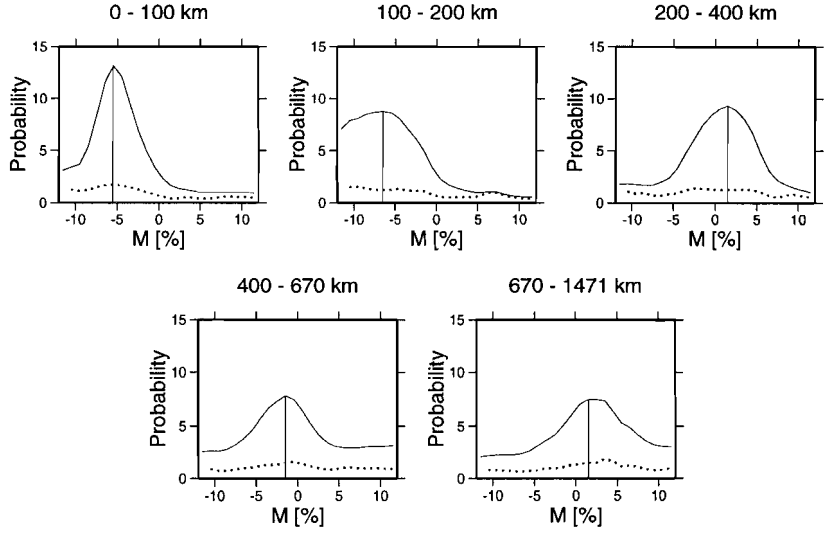

Figure 6.5: One-dimensional marginal probability density functions obtained in RUN1. The dotted line represents the uncertainty in the one-dimensional pdf. The maximum likelihood model is indicated by a vertical bar.

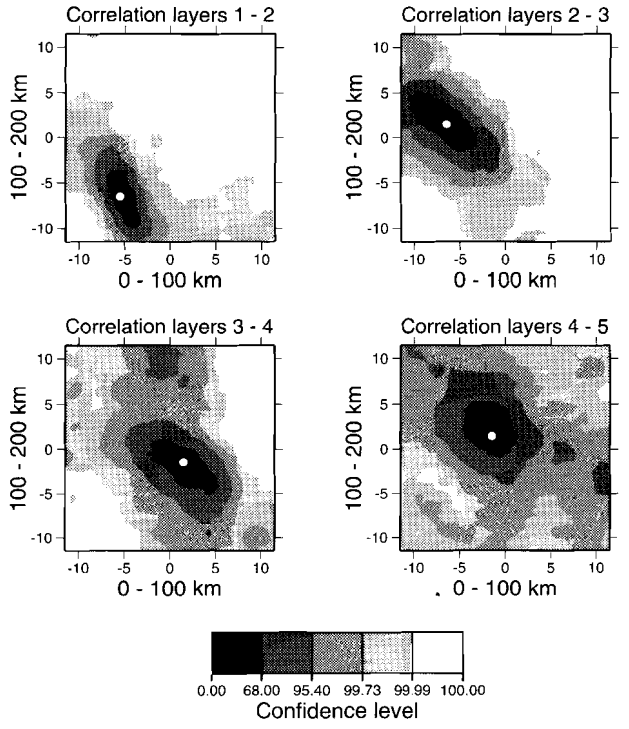

Figure 6.6: Confidence limits for the two-dimensional marginal probability density functions for RUN2. The white circle represents the maximum likelihood model.

6.7.2 RUN2, 7 layers

In the second run we decrease the layer thickness and increase the number of parameters to 7 in order to obtain more resolution in the upper mantle, see table 6.3. In this run the P-velocity is varied with value of $\partial lnV_p/\partial lnV_s = 0.5$. For RUN2 VEGAS performed 4 iteration with each 65536 model evaluations. The best models found during the inversion are presented in figure 6.4b. The best models show poorer clustering than the best models found in RUN1 due to a less constrained inverse problem caused by over-parameterization. The decrease of the layer thickness leads to more trade-off's between the parameters and to more oscillatory models. For the same reason the one and two-dimensional marginal pdf's are also less smooth than in the previous run, see figure 6.7 and 6.8. However, the maximum likelihood solution does not differ much from that obtained in RUN1. In the upper 220 km we have approximately 5% lower shear velocities. Below this depth we find the velocity model oscillating around zero with uncertainties of about 2%.

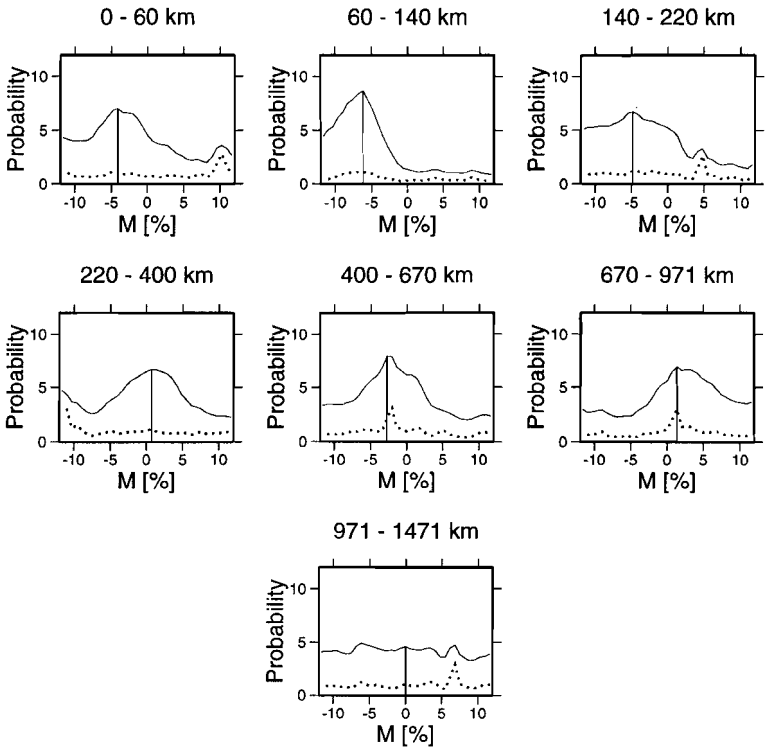

Figure 6.7: One-dimensional marginal probability density functions obtained in RUN2. The maximum likelihood model is indicated by a vertical bar.

In figure 6.9a we show the data together with synthetic seismograms computed for the starting model, the PREM model. In these seismograms the S wave arrives at around $t = 1000$ s, the SS wave around $t = 1200$ s and the fundamental mode between $t = 1300$ s and $t = 1600$ s. The fundamental modes in the synthetic seismograms are much too fast and also the S and SS phases arive to early. The synthetic seismograms computed for the maximum likelihood model for RUN2 shows a very good fit with the data, see figure 6.9b. Only for event rpn.93135.bhz the S and SS wave do not fit data well. This is likely caused by noise as the other events show a much better fit.

6.8 Discussion

We have successfully applied an adaptive Monte Carlo algorithm to the Bayesian inversion of waveform data. There are however some drawback's. Although the synthetic test has shown that the algorithm can be efficient for a likelihood func-

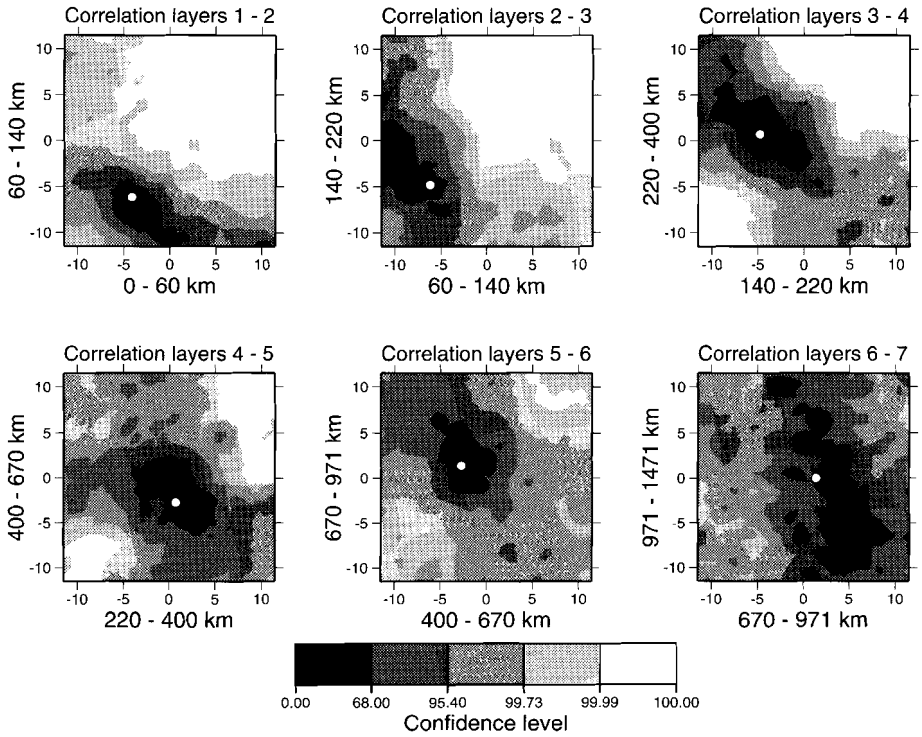

Figure 6.8: Confidence limits for the two-dimensional marginal probability density functions for RUN2. The white circle represents the maximum likelihood model.

tion with correlations between the parameters, the algorithm was less efficient for the waveform inversion problem. This is partly due to over parameterization of the inverse problem which causes trade-off's between the parameters. This could partly be solved by introducing non-uniform prior information $\rho(\mathbf{m})$ in equation 6.2. This is not a very efficient solution as in the first iteration the model space is still uniformly sampled. More efficiency can be obtained when the model space is searched along the axis of the correlations between the parameters, i.e. the covariance matrix $\mathbf{C}_m$ in an approach followed by De Ruyter and Curtis (1996). An other approach would be to carry out a pure Monte Carlo search and a resolution analysis of the set of succesful models (see chapter 5; Douma, Lomax and Snieder, 1996).

Our observations of the shear velocity under the ridge differs from Zhang and Tanimoto (1992) who find only down to 100km depth anomalies of -5% with respect to the same reference model PREM. Down to 300 km depth they observed a weak low velocity zone which may be correlated with slow up-welling of mantle material. Our models indicate a deeper and more pronounced low velocity zone

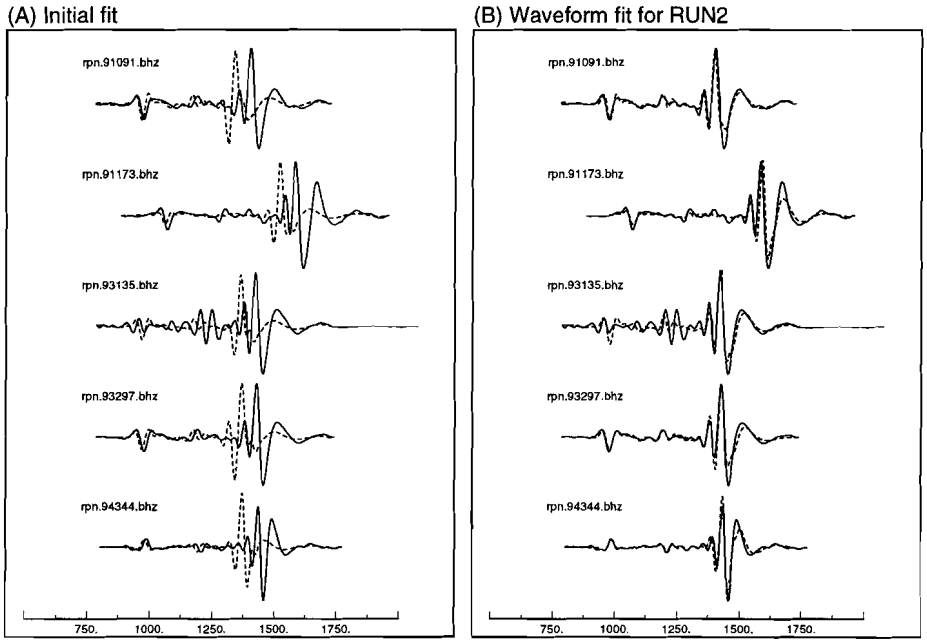

Figure 6.9: (a) Seismograms used in this study, the data is drawn in the solid lines, the synthetic seismograms computed for the starting model, PREM, are drawn in the dashed lines. (b) Waveform fit for the maximum likelihood model of RUN2.

than found by Zhang and Tanimoto (1992). In an other study, Su et al. (1992) showed that the model of Zhang and Tanimoto underestimates the observed SS-S travel-time residuals under the ridges by a factor of 3. They favor a model in which the low velocity anomaly under the ridges extends at least down to 300 km depth and possibly 600 km. They need a 350 km thick layer with -5% velocity anomaly to explain the observed SS-S data. Our dataset consists of Rayleigh waves including the S and SS phases. The final fits of the waveform data are very good and do not require such a large anomaly over 350 km depth as Su et al. (1992). We think that the differences between our models and those of Zhang and Tanimoto (1992) and Su et al. (1992) are caused by a combination of poorer data coverage and regularization parameters in the inversion.

In conclusion, our models show that a low velocity zone associated with the East Pacific rise extends down to a depth of 180 ± 40 km. The low velocity anomaly is -5%. Below this depth models differ only slightly from the average earth model PREM, in particular when marginal pdf's are taken into account. These models favor passive upwelling under the ridges.

References

Aki, K. and P. G. Richards, 1980. *Quantitative seismology : Theory and Methods*, W. H. Freeman, San Francisco.

Anderson, D. L., 1961. Elastic wave propagation in Layered Anisotropy Media, *J. of Geophys. Res.*, 66, 2953-2963.

Babuska, V. and M. Cara, 1991. *Seismic anisotropy in the Earth*, Kluwer Academic Publishers.

Backus, G. and F. Gilbert, 1968. The resolving power of gross earth data, *Geophys. J. R.A.S.*, 16, 169-205.

Bayes, T., 1763. Essay towards solving a problem in the doctrine of chances, republished in *Biometrika*, 1958, 45, 293-315.

Blackman, D.K., Orcutt, J.A., Forsyth, D.W. and J-M. Kendall, 1993. Seismic anisotropy in the mantle beneath an oceanic sreading centre, *Nature*, 366, 675-677.

Cara, M., Nercessian, A. and G. Nolet, 1980. New inferences from higher mode data in western Europe and northern Eurasia, *Geoph. J. R.A.S.*, 61 459-478.

Cara, M., Leveque, J.J. and V. Maupin, 1984. Density-versus-depth models from multimode surface waves, *Geophys. Res. Lett.*, 11, 633-636.

Cara, M. and J.J. Leveque, 1987. Oriented olivine crystals in the upper mantle : a test from the inversion of multimode surface-wave data, *Phys. Earth Planet. Inter.*, 47, 246-525.

Cara, M. and J.J. Leveque, 1988. Anisotropy of the asthenosphere : the higher mode data of the pacific revisited, *Geophys. Res. Lett.*, 15, 205-208.

Cary, P.W. and C.H. Chapman, 1988. Automatic 1-D waveform inversion of marine seismic refrection data, *Geoph. J. R.A.S*, 93, 527-546.

Cloetingh, S., Nolet, G., and R. Wortel, 1980. Crustal structure of the Eastern Mediterranean inferred from Rayleigh wave dispersion, *Earth and Planet. Science Lett.*, 51, 336-342.

Crampin, S., 1984. An introduction to wave propagation in anisotropic media, *Geoph. J. R.A.S.*, 76, 17-28.

De Jonge, M. R.,1995. *Geodynamic evolution and mantle structure*, Ph.D. thesis Utrecht University, Geologica Ultraiectina, 127.

Dercourt, J., Zonenshain, L.P., Ricou, L.-E., Kazimin, V.G., Le Pichon, X., Knipper, A.L., Grandjacquet, C., Sbortshikov, M., Geyssant, J., Lepvrier, C., Perchersky, D.H., Boulin, J., Sibuet, J.-C., Savostin, L.A., Westphal, M., Bazhenov, L., Lauer, J.P. and B. Bij-Duval, 1986. Geological evolution of the Tethys from the Atlantic to the Pamirs since the Lias, *Tectonophysics*, 123, 241-315.

De Ruyter, M. and A. Curtis, 1996. *An adative Monte Carlo algorithm for numerical integration applied to surface wave inversion*, afstudeerscriptie, Dept. Theor. Geophysics, Utrecht University.

De Voogd, B., Truffert, C., Chamot-Rooke, N., Huchon, P., Lallemant, S., and X. le Pichon, 1992. Two-ship deep seismic soundings in the basins of the Eastern Mediterranean Sea (Pasiphae cruise), *Geophys. J. Int.*, 109, 536-552.

Detrick, R.S., Harding, A.J., Kent, G.M., Orcutt, J.A. Mutter, J.C. and P Buhl, 1993. Seismic structure of the southern East Pacific Rise, *Nature*, 259, 499-503.

Douma, H., Snieder, R. and A. Lomax, 1996. Ensemble inference in terms of emperical orthogonal function, *Geoph. J. Int.* 127 363-378.

Duijndam, A. J. W., 1987. *Detailed Bayesian inversion of seismic data.* Ph.D. thesis, Delft University of Technology, The Netherlands.

Durrheim, R. J., and W. D. Mooney, 1994. Evolution of Precambrian lithosphere : seismological and geochemical constrains, *J. Geoph. Res.*, 99, 15359-15374.

Dziewonksi, A. M. and D. L. Anderson, 1981. Preliminary reference Earth Model, *Phys. Earth Plan. Int.*, 25, 297-356.

Dziewonski, A. M. and Woodhouse, J. H., 1983. An experiment in systematic study of global seismicity : centroid-moment tensor solutions for 201 earthquakes of 1981, J Geoph. Res. 88 3347-3271.

Ekstrom, G. A., 1987. *A broad Band Method of Earthquake Analysis*, Ph.D.Thesis, Harvard University, Cambridge, Massachusetts.

Forsyth. D.W., 1992. Geophysical contraints on mantle flow and melt generation beneath mid-ocean ridges, in *Geophysical Monograph*, 71, AGU.

Friederich, W. and Z.-X. Huang, 1996. Evidence for upper mantle anisotropy beneath southern Germany from Love and Rayleigh wave dispersion, *Geophys. Res. Lett.*, 23, 1135-1138.

Gaherty, J. B. and T. H. Jordan, 1995. Lehmann discontinuity as the base of an anisotropic mechanical boundary layer beneath continents, *Science*, 268, 1468-1471.

Gee, L.S. and T.H. Jordan, 1988. Polarization anisotropy and fine-scale structure of the Eurasian upper mantle, *Geoph. Res. Lett.* 15, 824-837.

Grad, M., Kryzanowska, M. and S.E. Pirhonen, 1995. Inhomogeneities of the Eurasian mantle structure from the traveltimes of the nuclear explosions

recorded by the Finnish seismic network during 1961-1985, *Geophys. J. Int.*, 121, 863-872.

Grand, S. and D. Helmberger, 1984. Upper mantle shear structure of North America, *Geophys.J. R.A.S* 76, 399-438.

Hammersley, J. M. and D. C. Handscomb, 1964. *Monte Carlo Methods*, Chapman and Hall, London.

Helffrich, G. R., Stein, S. and B. Wood, 1989. Subduction zone thermal structure and mineralogy and their relation to seismic wave reflections and conversions at the slab/mantle interface, *J. Geoph. Res.*, 94, 753-763.

Hess, H., 1964. Seismic anisotropy of the uppermost mantle under the oceans, *Nature*, 203, 629-631.

Husebye, E.S., and J. Hovland, 1982. On upper mantle seismic heterogeneities beneath fennoscandia, *Tectonophyscis*, 90, 1-17.

Jordan, T.H. 1981. Continents as a chemical boundary layer, *Phil. Trans. R. Soc. London*, A 301, 359-373.

Karato, S., 1992. On the Lehmann discontinuity, *Geoph. Res. Lett.*, 19, 2255-2258.

Kennett, B. and G. Nolet, 1978. Resolution analysis for discrete systems, *Geophys. J. Int.* 53, 413-425.

Knopoff, L., 1972. Observation and inversion of surface wave dispersion, *Tectonofysics*, 13, 497-519.

Lepage, G.P., 1978. A new algorithm for adaptive Multidimensional Integration, *J. Comp. Phys.*, 27, 192-203.

Lerner-Lam, A.L. and T.H. Jordan, 1987. How thick are the continents ?, *J. Geoph. Res.* 92, 14007-14026

Levshin, A. and L. Ratnikova, 1984. Apparent anisotropy in inhomogeneous media, *Geophys. J. R.A.S.* 76, 65-69.

Love, A. E. H., 1927. *A treatise on the mathematical theory of elasticity*, Dover publ. New York, 1944.

Marquering, H. and R. Snieder, 1996. Shear wave velocity structure beneath Europe, Eastern atlantic and western Asia from waveform inversions including mode coupling, *Geophys. J. int.*, 127, 283-304.

Maupin, V., 1985. Partial derivatives of surface wave phase velocities for flat anisotropic models, *Geophys. J. R.A.S.*, 83, 379-398.

McLaughin, K., L., Barker, T. G., Day, S. M., Shkoller, B. and J. L. Stevens, 1992. Effects of subduction zone structure on explosion-generated Rayleigh waves: 3-D numerical simulations, *Geophys.J.Int.*, 111, 291-308.

Meissner, R., 1986. *The continental crust : A geophysical approach*, Academic, San Diego Calif.

Montagner, J. P. and D. L. Anderson, 1989. Petrological constraints on seismic anisotropy, *Phys. Earth Planet. Int.*, 54, 82-105.

Montagner, J. P. and H. C. Nataf, 1986. A simple method for inverting the azimuthal anisotropy of surface waves, *J. Geoph. Res.*, 91, 511-520.

Montagner, J. P. and T. Tanimoto, 1991. Global upper mantle tomography of seismic velocities and anisotropies, *J. Geoph. Res.*, 96, 20337-20351.

Mooney, W.D., Laske, G. and G. Masters, 1996. Crust5.1 : A global crustal model at 5 × 5 degrees, submitted to *J. Geoph. Int.*

Mosegaard, K. and A. Tarantola, 1995. Monte Carlo sampling of solutions to inverse problems, *J. Geoph. Res.*, 100, 12431-12448.

Mueller, R. D., Roest, W. R., Royer, J. Y., Gahagam, L. M. and J. G. Sclater 1997. Digital Isochrons of the world's ocean floor, *J. Geophys. Res.*, 102, 3211-3214.

Muyzert, E.J. and R.K. Snieder, 1996. The influence of errors in the source parameters on phase velocity measurements of surface waves, *Bull. Seis. Soc. Am.*, 86, 1863-1872.

Nakanishi, I. and D. L. Anderson, 1984. Measurements of mantle wave velocities and inversion for lateral heterogeneity and anisotropy - II. Analysis by the single-station method, *Geophys.J. R.A.S* 78, 573-617.

Nishimura, C. L., and D. W. Forsyth, 1989. The anisotropic structure of the upper mantle in the Pacific, *Geophys. J. Int.*, 96, 203-229.

Nolet, G. 1977. The upper mantle under western Europe inferred from the dispersion of Rayleigh modes, *J. Geophys.*, 43, 265-286.

Nolet, G., 1990. Partitioned waveform inversion and the two-dimensional structure under the network of autonomously recording seismographs, *J. Geoph. Res.*, 95, 8499-8512.

Nolet, G., van Trier, J., Huisman, R., 1986. A formalism for nonlinear inversion of seismic surface waves, *Geophys. Res. Lett.*, 13, 26-29.

Nolet, G and A. Zielhuis, 1994. Low S velocities under the Tornquist-Teisseyre zone: Evidence for water injection into the transition zone by subduction, *J. Geophys. Res.*, 99, 15813-15820.

Paige, C.C. and M.A. Saunders, 1984. LSQR : an algorithm for sparse linair equations and sparse least squares, *ACM Trans. Math. Soft.*, 8, 195-209.

Pavlenkova, N. I, 1996. Crust and upper mantle structure in northern eurasia from seismic data, *Advances in geophysics*,37, 1-121.

Phipps Morgan, J., 1991. Mid-Ocean Ridge dynamics : Observations and theory, *Rev. Geophys. sup.* 807-822.

Press, W.H., Teukolsky, S.A., Vettering, W.T. and B.P. Flannery, 1992. *Numerical Recipes: the art of Scientific Programming, 2nd edition*, Cambridge University Press.

Scales, J. A. and R. K. Snieder, 1997. To Bayes or not to Bayes, *Geophysics*, 62, 1045-1046.

Sclater, J.G., Jaupert, C. and D. Galson, 1980. The heat flow through oceanic and continental crust and the heat loss of the earth, *Rev. Geophys. and Space phys*, 18, 269-311.

Sen, M.K. and P.L. Stoffa, 1996a. Bayesian inference, Gibbs'sampler and uncertainty estimation in geophysical inversion, *Geophys. Prop.*, 44,313-350.

Sen, M.K. and P.L. Stoffa, 1996b. Global optimization methods in geophysical inversion, *Advances in exploration geophysics*, 4, Elsevier Science B.V. Amsterdam.

Silver, P. G., 1996. Seismic anisotropy beneath the continents : Probing the depths of geology, *Annu. Rev. Earth Planet. Sci.*, 24, 385-432.

Sipkin, S.A., 1986. Interpretation of non-double couple earthquake source mechanisms derived from moment tensor inversion, *J. Geophys. Res.*, 91, 531-547.

Smith, M. L. and F. A. Dahlen, 1973. The azimuthal dependence of Love and Rayleigh wave propagation in a slightly anisotropic medium, *J. Geophys. Res.*, 78, 3321-3333.

Snieder, R. and H. Paulssen, 1993. Future deployment of the NARS array, *Proceedings of the Europrobe Symposium Jablonna 1991*, 129-132.

Stutzmann, E., and J.P. Montagner, 1993. An inverse technique for retrieving higher mode phase velocity and mantle structure. *Geophys. J. Int.*, 113, 669-683.

Su, W., Woodward, R.L. and Dziewonski, A.M., 1992. Deep origin of mid-ocean-ridge seismic velocity anomalies, *Nature*, 360, 149-152.

Takeuchi, H. and M. Saito, 1972. Seismic surface waves, *Methods in computational Physics*, 11, 217-295.

Tanimoto, T., 1991. Waveform inversion for three-dimensional density and S wave structure, *J. Geophys. Res.*, 96, 8167-8189.

Tanimoto, T. and D. L. Anderson, 1985. Lateral heterogeneity and azimuthal anisotropy of the upper mantle : Love and Rayleigh waves 100-250 s, *J. Geophys. Res.*, 90, 1842-1858 .

Tarantola, A., 1987. Inverse Problem Theory, Elsevier, New York.

Tarantola, A. and B. Valette, 1982. Generalized Nonlinear Inverse Problems solved using the Least Squares criterion, *Rev. Geophys. and Space Physics*, 20, 219-232.

Trampert, J. and J.H. Woodhouse, 1995. Global phase velocity maps of Love and Rayleigh waves between 40 and 150 seconds, *Geophys. J. Int.*, 122, 675-690.

Van Heijst, H. J., Snieder, R. and R. Nowack, 1994. Resolving a low-velocity layer with surface wave data, *Geophys. J. Int.*, 118, 333-343.

Vlaar, N. J., 1968. Ray theory for an anisotropic inhomogeneous elastic medium, *Bull. Seis. Soc. Am.*, 58, 2053-2072.

Vlaar, N.J., Van Keken, P. E. and A. P. van den Berg, 1994. Cooling of the Earth in the Archean : consequences of the pressure-release melting in a hotter mantle, *Earth and Planet. Sci. Lett.*, 121, 1-18.

Wielandt, E. and Knopoff, L., 1982. Dispersion of very long-period Rayleigh waves along the East Pacific Rise : evidence for S wave velocities anomalies to 450 km depth. *J. Geophys. Res.*, 87, 8631-8641.

Woodhouse, J.H. and Dziewonski, A.M., 1984. Mapping the upper mantle : Three-dimensional modeling of Earth structure by inversion of seismic waveforms, *J. Geophys. Res.*, 89, 5953-5986.

Yanovskaya, T. B., R. Maaz, P. G. Ditmar and H. Neunhofer, 1988. A method for joint interpretation of thephase and group velocities to estimate lateral variations in the Earth's structure, *Phys. Earth Planet. Int.* 51, 59-67.

Yanovskaya, T. B., Panza, G. F., Ditmar, P. D., Suhadolc, P. and Mueller, S., 1990. Structural heterogeneity and anisotropy based on 2-D phase velocity patterns of Rayleigh waves in Western Europe, *Atti dell Acca. Naz. dei Lincei Rendiconti*, 9, 127-135.

Zhang, Y. and T. Tanimoto, 1992. Ridges, hotspots and their interaction as observed in seismic velocity maps, *Nature*, 355, 45-49.

Zhang, Y.,and T. Tanimoto, 1993. High resolution Global Upper Mantle Structure and Plate Tectonics, *J. Geophys. Res.*, 98, 9793-9823.

Zielhuis, A. and G. Nolet, 1994a. The deep seismic expression of an ancient plate boundary in Europe, *Science*, 265, 79-81.

Zielhuis, A., and G. Nolet, 1994b. Shear-wave velocity variations in the upper mantle beneath central Europe, *Geophys. J. Int.*, 117, 695-715.

Zonenshain, L. P., Kuzmin, M. I. and L. M. Natapov, 1990. Geology of the USSR: A plate tectonic synthesis, *Geodynam. Series*, 21, Am. Geophys. Un.

Samenvatting (summary in Dutch)

Het NARS-DEEP project (Network of Autonomously Recording Seismographs Deployed on the East European Platform) omvat de installatie van een aantal seismograven in de landen van de voormalige Sovjet-Unie. Het doel van het project is het verkrijgen van seismische data die Oost-Europa bemonsteerd en door de interpretatie van deze gegevens een beter inzicht te verkrijgen in de geodynamische geschiedenis van de regio. Dit project is mogelijk geworden door de afloop van de koude oorlog en de daarop volgende verandering. Als gevolg van de Oost-West tegenstelling is gegevens uitwisseling erg beperkt geweest, wat duidelijk blijkt uit een kaart met distributie van de digitale seismografen in Europa, zie figuur 1.1. Duidelijk is te zien dat in een aantal West-Europese landen (zoals Duitsland en Engeland) het aantal seismografen zeer groot is met een onderlinge afstand van ongeveer 100 km. Tot enige jaren geleden waren er vrijwel geen moderne seismografen in Oost Europa en bedroegen de onderlinge afstanden tussen de seismografen meer dan 1000 km. Met het NARS-DEEP project, het Duitse GEOFON project en het Amerikaanse IRIS project is in Oost-Europa het aantal stations tot een zeer bruikbaar niveau gekomen met onderlinge afstanden van 250 km. In dit proefschrift wordt de mantel structuur onder Oost-Europa bestudeerd door de analyse van seismogrammen van de nieuw beschikbaar gekomen data. Voor de analyse zijn enkele nieuwe technieken ontwikkeld die een betere interpretatie van de seismogrammen mogelijk maken.

De structuur van de aarde wordt bestudeerd met behulp van oppervlakte golven. Er zijn twee belangrijke soorten oppervlakte golven : de horizontaal gepolariseerde transversale Love golven en de vertical gepolariseerde Rayleigh golven. De snelheidsstructuur van de aarde kan worden bepaald uit de dispersieve eigenschappen van de oppervlakte golven. In dit proefschrift gebeurd dit door golfvorm inversie. De golfvorm inversie is een procedure waarbij het geobserveerde seismogram wordt vergeleken met synthetische seismogrammen totdat het verschil minimaal is. Hiervoor worden de lagen van het aardmodel steeds aangepast. In figuur 5.2 zijn de resultaten van een dergelijke procedure te zien. Figuur 5.2a laat de fit (overeenkomst) van het geobserveerde seismogram zien met een synthetisch seismogram, berekend voor het start aardmodel van de inversie. Vooral de fundamentele Love golven (aankomst vanaf $t = 950$ s) laten een slechte fit zien. De hogere mode Love golven die aankomen tussen $t = 750 - 950$ s laten een beter

maar niet perfecte fit zien. In figuur 5.2b is een tussenresultaat van de golfvorm inversie te zien. Hier is alleen de fundamentele mode gefit vanaf $t = 950s$. Dit stuk van de seismogrammen laat dan ook een zeer goede fit zien ten op zichte van het start model. In de laatste figuur 5.2c laten we het resultaat zien als ook de hogere modes worden gebruikt. Kleine doch belangrijke verschillen zijn te zien voor de bevingen *kev*.91031.*bht* en *kev*.91195.*bht*.

Voor het berekenen van de synthetische seismogrammen is het van belang dat accurate bronparameters (sterkte, brondiepte, breukvlak orientatie) worden gebruikt. Deze bronparameters worden routinematig bepaald door diverse internationale organisaties. Echter zoals elke waarneming hebben ook de bronparameters hun onnauwkeurigheden. In hoofdstuk 2 wordt de invloed van onnauwkeurigheden in de bronparameters op dispersie metingen en golfvorm inversies onderzocht. Er is daarvoor een data set geanalyseerd van een cluster van aardbevingen in Afganstan en de Hindu Kush. Deze bevingen vonden dicht bij elkaar plaats en zijn op grote afstand waargenomen door het station KEV in Finland. Figuur 2.1a-b laat de golfvormen zien voor 10 Rayleigh golf seismogrammen in twee frequentie banden. Zes bevingen komen zeer goed overeen met de synthetische seismogrammen, voor vier bevingen is deze fit echter aanzienlijk minder (*kev*.93334.*bhz*, *kev*.93261.*bhz*, *kev*.92141.*bhz*, *kev*.90135.*bhz*). Omdat deze seismogrammen allen hetzelfde bron ontvanger pad hebben kunnen variaties in aardstructuur niet de reden zijn van deze matige fits. De oorzaak hiervan moet gezocht worden in onzekerheden in de bronparameters. In dit hoofdstuk wordt een methode gepresenteerd waarbij dit soort onzekerheden voorspeld kunnen worden uit de bronparameters zonder de seismogrammen te bekijken. De resultaten hiervan zijn samengevat in de laatste kolom van figuur 2.1. Als in dit figuur een van de lijntjes hoger is dan 1 betekent dit dat bij die frequentie het synthetische seismogram erg gevoelig is voor fouten in de bronparameters. Dit blijkt het geval te zijn voor de vier slecht gemodelleerde bevingen. Deze methode is met succes ook op de andere data-sets toegepast die gebruikt zijn in dit proefschrift.

Voor een correcte berekening van synthetische seismogrammen moet rekening gehouden worden met eventuele anisotropische eigenschappen van de aarde. Anisotropie houdt in dat de snelheid van de seismische golven richtingsafhanklijk is. Als gevolg hiervan kunnen Love golven en Rayleigh golven met verschillende snelheden reizen. Voor inversies betekend anisotropie dat er meer parameters bepaald moeten worden, op elke plaats een isotroop deel dat richtings onafhanklijk is alsmede een aantal parameters die de richtsafhanklijkheid van de anisotropie bepalen. In het meest algemene geval wordt dit beschreven door een elasticiteits tensor met 21 te bepalen parameters. Voor oppervlakte golven wordt vaak een simpel model van anisoptropy met een symmetrie as aangenomen dat slechts 5 parameters heeft namelijk transversale isotropie. In hoofdstuk 3 wordt aangetoond dat met enkele benaderingen het aantal parameters dat uit oppervlakte golven bepaald kan worden nog kleiner is. Dit kan omdat een aantal parameters afhankelijk van elkaar zijn en daardoor niet uniek op te lossen zijn. In deze nieuwe parameterisatie kunnen uit Rayleigh golven langs een vast pad slechts drie pa-

rameters bepaald worden. Love golven zijn slechts gevoelig voor 1 parameter. In dit hoofdstuk wordt ook de invloed van de dichtheid besproken en aannemelijk gemaakt dat het moeilijk is om informatie over de dichtheids structuur van de aarde te bepalen.

In hoofdstuk 4 wordt een model voor de aardstructuur onder Oost Europa gepresenteerd. Deze studie is mogelijk geworden door de beschikbaarheid van NARS-DEEP data en enkele toevallige aardbevingen. Het model is een twee dimensionaal profiel van de mantel langs de $30°E$ meridiaan van Egypte tot Spitsbergen, zie figuur 4.1. Uit de Love en Rayleigh data is een isotroop S-snelheid model bepaald dat het gemiddelde beschrijft (middelste figuur 4.1). Uit het verschil van beide golftypen is het anisotroop SA-snelheidsmodel bepaald (onderste figuur 4.1). Dit is een interressant profiel omdat het een aantal zeer verschillende geologische gebeiden doorsnijdt. In de Oostelijke middellandse zee laat het model tot een diepte van 150 km een lage S-snelheid ten opzichte van het startmodel zien. Ook zien we in deze regio een sterke anisotropie (onderste figuur). Deze anisotropie kan verklaard uit de in dit gebied aanwezige resten van de bodem van de oude Tethis oceaan. De Tethis ocean is verdwenen door de botsing van Afrika met Eurasia. Dat oceaan bodem veel sterker anisotroop dan continenten is kan ook gezien worden in het model. Onder Oost Europa is namelijk veel minder anisotropie waar te nemen. Het S-snelheids model geeft daarintegen een zeer duidelijk beeld te zien van het continent (middelste figuur). Een hoge snelheidslaag die geassocieerd is met het continent is duidelijk te volgen tot 200 km diepte. De diepte van deze hoge snelheidslaag varieert met de ouderdom van het continent. De NARS-DEEP stations NE51-NE56 staan op het oudste deel dat ongeveer 2 miljard jaar oud is. De flanken zijn "slechts" honderden miljoenen jaren oud en laten een dunner continent zien (100 km). De gemiddelde snelheden in het continent nemen duidelijk toe met de geologische ouderdom maar de preciese relatie is nog niet duidelijk, zie figuur 4.7. De geobserveerde dikte en snelheids variaties in het continent kunnen verklaard worden door thermische afkoeling en variaties in chemie van het continent.

In hoofdstuk 5 wordt een tweede studie naar de snelheidsstructuur in Oost Europa gepresenteerd. Hiervoor wordt de data-set die gebruikt is in hoofdstuk 2 geinverteerd. De seismogrammen worden gezamelijk geinverteerd wat leidt tot een betere oplossing in vergelijking tot de inversie van elk seismogram afzonderlijk. Voor de inversie wordt een Monte Carlo algoritme gebruikt waarbij vele honderdduizende modellen getest worden tegen de data. Uit de beste modellen wordt vervolgens een gemiddeld model bepaald en de resolutie bepaald. In de resolutie analyse, die gebaseerd is op een nieuwe interpretatie van een bestaand criterium (formule 5.13), worden de robuste delen van een set van succesvolle modellen bepaald. De resultaten voor de anisotrope inversie van de Rayleigh golven zijn te zien in figuur 5.16. Hierbij is de in hoofdstuk 3 afgeleide anisotropie parameter set gebruikt. De beste Monte Carlo modellen zijn getekend met grijze lijnen. Aan het feit dat deze modellen bijna overal de maximale grenzen van het Monte Carlo algorithme bereiken is te zien dat er teveel lagen in het model zijn. Met behulp van de

resultaten van de resolutie analyse is de set van modellen gefilteerd om zodoende de meest robuste delen van de oplossing te verkrijgen, dit zijn de zwarte lijnen in figuur 5.16. Hieruit wordt het gemiddelde model bepaald dat alleen afwijkt in de bovenste 200 km van de aarde met meer dan 1% af van het gemiddeld aardmodel PREM (linker figuur). De anisotropie parameters zijn veel slechter opgelost wat te zien is aan de zeer grote spreiding van de modellen. Alleen rond de 150 km diepte observeren we enige anisotropie in de gemiddelde longitunale snelheid α_+. Het kan echter niet hard gemaakt worden dat deze anisotropie ook daadwerkelijk vereist is door de data (middelste figuur). Een vergelijking van dit MC model met een drietal bestaande modellen laat zien dat het MC model redelijk overeenkomt met andere continentale modellen, zie figuur 5.18. De grootste variaties bevinden zich in de bovenste 200 km van de aarde. In vergelijking met de andere modellen bevat het MC model minder anisotropie wat waarschijnlijk het gevolg is van het nauwkeurig meenemen van de variaties in de aardkorst in de berekening van de synthetische seismogrammen. Verbeteringen in de modellering van de korst structuren zullen waarschijnlijk leiden tot nog continentale snelheids modellen met nog minder anisotropie.

In het laatste hoofdstuk wordt een andere regio onderzocht, de zeer snel spreidende oceaan rug in de oostelijke Pacific, zie figuur 6.1. Een belangrijke vraag hier is van welke diepte het vulkanisch materiaal komt. Hiervoor wordt een snelheidsmodel afgeleid met behulp van Rayleigh golven van aardbevingen uit Centraal Amerika die geregisteerd zijn door het station RPN op Paaseiland. In dit hoofdstuk wordt het golfvorm inversie probleem Bayesiaans geformuleerd. Vervolgens worden de golfvormen geinverteerd met behulp van een adaptief Monte Carlo algoritm : VEGAS. Dit iteratief algorithme past de zoekregio's aan aan de plaatsen waar succevolle modellen zijn gevonden en is efficienter dan het algoritme dat in het vorige hoofdstuk is gebruikt. Met behulp van de Baysiaanse formulering en het VEGAS algoritme worden de kansverdelingsfuncties voor de modelparameters bepaald. Deze zijn te zien onder meer te zien in figuur 6.7 waar de verticale lijn het meest waarschijnlijke model weergeeft. Het meest waarschijnlijke model is tot 220 km diepte ongeveer 5% langzamer dan het gemiddelde aardmodel PREM. Onder de 220 km is geen verschil met het PREM model aan te tonen. Dit wijst erop dat de bron van het vulkanisme bij de rug niet diep in de mantle is maar in de bovenste 200 km.

Dankwoord (Acknowledgements)

Bij het schrijven van dit proefschrift heb ik hulp en steun gehad van een aantal mensen die ik hiervoor wil bedanken.

Allereerst gaat mijn dank uit naar mijn promotor, Roel Snieder voor het mogelijk maken van dit proefschrift. Zijn stimulerend vermogen, openheid en vertrouwen heb ik zeer gewaarderd. De samenwerking met Hanneke Paulssen binnen het NARS-DEEP project was altijd aangenaam. Ik wil bedanken voor haar frisse en kritische blik op de seismologie. Jeannot Trampert wil ik bedanken voor het waarnemen van de honneurs tijdens de afwezigheid van Roel en zijn vaak duidelijke stellingname.

Dolors Alsina, Harm Dorren, Henk Marquering, Filip Neele, Axel Rohm, Martin Schimmel bedank ik voor de discussies, hulp en collegialiteit. Ook Huub Douma en Paul Meijer leverden waardevolle bijdragen in discussies. Het laatste hoofdstuk van dit proefschrift is voortgekomen uit het afstudeeronderzoek dat Mirko van der Baan heeft verricht waarvoor dank. Aan dit hoofdstuk heeft ook Harm van Avendonk bijgedragen. Enig inzicht in de werking van de seismograaf is mij bijgebracht door Arie van Wettum. Dit proefschrift steunt op het werk dat Guust Nolet in zijn Utrechtse tijd heeft verricht.

Een aantal mensen heeft belangrijke ondersteuning verricht. Bernadine Vet was altijd behulpzaam bij de adminstratieve rompslomp. Joop Hoofd en Theo van Zessen boden altijd hulp bij allerhande computer problemen. Bernard Dost van het Orfeus Data Centrum heeft zijn seismogrammen bijgedragen. De financiele steun van GOA/NWO werdt elke maand zeer gewaardeerd.

Former Utrechters Eleonore Stutzman, Anthony Lomax, Andrew Curtis and Laura Jones are thanked for valuable discussions in different stages of this thesis. I would like to thank Jean-Paul Montagner for a discussion about anisotropy. Gaby Laske send me the crustal model. The members of the dissertation committee provided valuable comments on this manuscript. I also would to thank the partners in de NARS-DEEP project for their cooperation. The data mangement centers from IRIS and GEOFON provided additional data for which they are acknowledged.

Mijn moeder wil ik bedanken voor mijn opvoeding en in het bijzonder voor het tijdig ingrijpen in mijn taalverwervingsproces wat een ramp heeft doen voorkomen. Zonder dat was dit proefschrift er waarschijnlijk nooit gekomen. Mijn ooms Kees en Reinier Braams hebben duidelijk hun sporen nagelaten in mijn keuze voor de wetenschap. Geofysica is nu eenmaal een kruising tussen zaken als de relatie tussen de doorsnede en omtrek van een boom en stenenzoeken. Ontspanning heb ik vaak gezocht in het bergklimmen. Hoewel dit met het vorderen van de jaren steeds minder vaak voorkwam heeft de herinnering veel goedgemaakt. Tot slot wil ik Liesbeth bedanken voor haar steun en organisatiekunsten de afgelopen jaren en in het bijzonder tijdens de laatste maanden.

Curriculum Vitae

Everhard Muijzert is op 20 augustus 1967 geboren te Leiden. Aan het Herman Jordan Lyceum te Zeist slaagde hij voor de eindexamens HAVO (1985) en VWO (1987). In september 1987 is hij begonnen aan de studie Geofysica aan de Universiteit Utrecht. Hier werden in mei 1989 het Propeadeutisch examen Geofysica en in maart 1993 het Doctoraal examen Geofysica behaald. Tussentijds is de auteur enige maanden werkzaam geweest als geofysicus bij de Rijks Geologische dienst te Haarlem. Van 1 september 1993 tot 1 september 1997 volgde de aanstelling als onderzoeker in opleiding (OIO) bij de vakgroep Geofysica, Universiteit Utrecht, voor het NARS-DEEP project. Vanaf januari 1998 is de auteur werkzaam als researcher bij Schlumberger Cambridge Research.